ELECTROMAGNETICALLY INDUCED TRANSPARENCY IN SEMICONDUCTORS

by

MARK CHRISTOPHER PHILLIPS

A DISSERTATION

Presented to the Department of Physics
and the Graduate School of the University of Oregon
in partial fulfillment of the requirements
for the degree of
Doctor of Philosophy

December 2002

"Electromagnetically Induced Transparency in Semiconductors," a dissertation prepared by Mark Christopher Phillips in partial fulfillment of the requirements for the Doctor of Philosophy degree in the Department of Physics. This dissertation has been approved and accepted by:

Dr. Hailin Wang, Chair of the Examining Committee

Date

Committee in charge:	Dr. Hailin Wang, Chair Dr. Thomas W. Mossberg Dr. Jens Nöckel Dr. Raymond Frey Dr. Andrew Marcus

Accepted by:

Dean of the Graduate School

An Abstract of the Dissertation of

Mark Christopher Phillips for the degree of Doctor of Philosophy

in the Department of Physics to be taken December 2002

Title: ELECTROMAGNETICALLY INDUCED TRANSPARENCY IN SEMICONDUCTORS

Approved: ______________________________
Dr. Hailin Wang

Electromagnetically Induced Transparency (EIT) is a phenomenon in which the presence of a nonradiative coherence leads to destructive quantum interference, causing an otherwise absorbing transition to become transparent. As a spectroscopic tool, EIT can be used to probe for the existence of nonradiative coherences and to study their properties. Furthermore, EIT is of interest because it demonstrates the control of quantum coherence to dramatically change the linear and nonlinear optical properties of the system. Although EIT and related phenomena have been studied extensively in atomic systems, analogous effects have not been previously observed for interband transitions in semiconductors.

This dissertation presents experimental demonstrations of EIT using exciton and biexciton transitions in semiconductor quantum wells. Results are first presented which show that Rabi splitting of exciton and biexciton transitions is possible, though affected by many-body interactions. The ability to induce Rabi splitting is shown to be a prerequisite for establishing EIT in semiconductors. Numerical simulations of the optical Bloch equations indicate that EIT signatures can be observed using transient pump-probe spectroscopic techniques in which the pump is long and the probe is short relative to the dipole decoherence times. Observations of EIT due to three types of nonradiative coherence are presented and discussed: coherence between heavy-hole and light-hole valence bands, exciton spin coherence, and biexcitonic coherence.

In addition to demonstrating EIT in semiconductors, this dissertation discusses how these EIT experiments provide valuable information about the interplay of quantum coherence and many-body correlations in semiconductors. Studying the behaviors of the EIT signatures under various experimental conditions shows how the underlying nonradiative coherences are affected by exciton-exciton interactions. More importantly, the EIT experiments presented here indicate new types of quantum coherences induced by the many-body interactions themselves, a process without analog in noninteracting atomic-like systems. Specifically, this dissertation shows that in addition to bound biexciton states, even unbound two-exciton states can lead to quantum coherence through many-body correlations.

CURRICULUM VITA

NAME OF AUTHOR: Mark Christopher Phillips

GRADUATE AND UNDERGRADUATE SCHOOLS ATTENDED:

University of Oregon, Eugene, Oregon
University of Washington, Seattle, Washington
Pacific University, Forest Grove, Oregon

DEGREES AWARDED:

Doctor of Philosophy in Physics, 2002, University of Oregon
Bachelor of Science in Physics, 1995, Pacific University

AREAS OF SPECIAL INTEREST:

Ultrafast Nonlinear Spectroscopy of Semiconductors
Correlation Effects in Semiconductors

PROFESSIONAL EXPERIENCE:

Research Assistant, Hailin Wang Lab, Department of Physics, University of Oregon, 1998-2002

Teaching Assistant, Department of Physics, University of Oregon, 1997-1998

Teaching Assistant, Department of Physics, University of Washington, 1995-1997

Teaching Assistant, Pacific University, 1991-1995

Software and Hardware Tester, Oxford Molecular/CAChe Scientific, Beaverton, Oregon, 1993-1995

Lab Assistant, Pacific Environmental Laboratory, Beaverton, Oregon, 1992-1993

AWARDS AND HONORS:

Valedictorian (4.00 GPA), Pacific University (1995)

Outstanding Senior in the Natural Sciences, Pacific University (1995)

Ph.D. prize for highest score on Ph.D. Qualifier exam, University of Oregon (1997)

PUBLICATIONS:

Mark Phillips and Hailin Wang, “Electromagnetically Induced Transparency due to Intervalence Band Coherence in a GaAs Quantum Well,” submitted to Optics Letters.

Mark Phillips, Hailin Wang, I. Rumyantsev, N. H. Kwong, R. Takayama, and R. Binder, “Electromagnetically Induced Transparency in Semiconductors,” *to be submitted.*

Mark Phillips and Hailin Wang, “Spin coherence and electromagnetically induced transparency via exciton correlations,” Phys. Rev. Lett. **89**, 186401 (2002).

T. Meier, S. W. Koch, M. Phillips, and H. Wang, “Strong coupling of heavy- and light-hole excitons induced by many-body correlations,” Phys. Rev. B **62**, 12605 (2000).

Mark Phillips and Hailin Wang, “Coherent oscillation in four-wave mixing of interacting excitons,” Solid State Communications **111**, 317 (1999).

ACKNOWLEDGEMENTS

I would like to thank Professor Hailin Wang for his guidance and support over the course of this research. He has taught me not only about semiconductor optics, but also about how to be a good researcher, experimentalist, and scientist.

I would like to acknowledge Professor Michael Raymer for useful discussions and also for financial support of part of this research. I am grateful for the theoretical expertise of Dr. Rolf Binder, Dr. Torsten Meier, and Dr. Stephan Koch, all of who aided in increasing my understanding of semiconductor physics. Professor Thomas Mossberg has helped me to understand my research, especially from the perspective of atomic physics research. I also thank Dr. David Alavi for providing help on the setup of the lasers and pulse shapers used in the experiments, and J. E. Cunningham and Duncan Steel for providing the quantum well samples.

During my stay at the University of Oregon, I have had many useful discussions with my fellow students. I thank Dr. Xudong Fan for his help and guidance especially during my initial period of starting research in the Wang lab. I am very grateful to Dr. Ethan Blansett for many insightful discussions about semiconductors, optics, and TEX. My research was made much easier and more enjoyable due to extensive help, friendship, and shared lab space from Scott Lacey and Phedon Palinginis. I would also like to thank Sasha Tavenner Kruger, Susanta Sarkar, Yumin Shen, Bert Schumann, and the other members of the Wang lab for their suggestions and help with my research.

This research could not have been performed without the help from the extremely skilled office staff of the physics department. I would especially like to

thank Colleen McKillip, Janine O'Guinn, Sandee Thompson, Jani Calivan, Bonnie Grimm, Mary Crafts, and Jennifer Lewis.

Finally, I am extremely grateful for the support and love of my wife Cheryl, who has helped me in countless ways through the long and arduous process of obtaining a Ph.D. I would also like to thank my parents for their unending support over the years.

DEDICATION

For Cheryl

TABLE OF CONTENTS

Chapter Page

APPENDIX

LIST OF FIGURES

CHAPTER I

INTRODUCTION

The study of nonlinear optical processes in semiconductors is driven by two primary goals. The first goal is fueled by the recent rapid growth in the number and type of optical devices based on semiconductors. An understanding of the physics of semiconductors is essential for improving existing devices, and the new phenomena uncovered by research can lead to additional applications. But semiconductors are interesting not only for their technological applications, but also because they provide an environment for the study of physics in a strongly-interacting many-body system. This second goal of studying the effects of many-body interactions on the optical properties of a semiconductor system also hopefully leads to a better understanding of many-body physics in general. These two goals are complementary. The development of semiconductor technology provides the tools and resources without which more basic research would progress slowly, if at all. Likewise, the basic research into many-body interactions leads to a better understanding of semiconductors on which new technological advances can be built.

A particularly interesting nonlinear optical phenomenon which has been explored extensively in atomic systems is that of electromagnetically induced transparency (EIT) [1–4]. EIT is a process in which an otherwise absorbing optical transition is made transparent as a consequence of quantum interference. EIT may be observed in a three-level system, such as the one shown in Fig. 1, with two dipole transitions $|a\rangle \leftrightarrow |e\rangle$ and $|b\rangle \leftrightarrow |e\rangle$ sharing a common state. Because there are two transition pathways to the common state, the transition amplitudes interfere, which can lead to a vanishing net transition amplitude. The graphs shown in Fig. 2 show an example of the dramatic changes which can be induced in the absorption spectrum by EIT. The destructive interference in EIT is the direct consequence of a nonradiative (Raman) coherence being induced in the system. Many quantum interference effects related to EIT and a nonradiative coherence have been explored in atomic systems. One of these effects is slow light, where the group velocity of light pulses can be reduced to speeds on the order of a few meters per second [5–7]. Another effect is that of adiabatic population transfer, where populations can be transferred without loss between states which are not directly dipole coupled [8, 9]. Experiments have also demonstrated that light can effectively be stopped, stored in a nonradiative coherence, and then read out at a later time [10, 11]. There are also schemes for lasing without inversion which are based on the generation of nonradiative coherences [4, 12–14]. As all these phenomena are related, the demonstration of EIT in a system can open the door to this wide array of fascinating effects.

There has been considerable interest in demonstrating EIT and related phenomena in semiconductors. A major reason for this interest lies in the possibility of making practical solid-state devices based on EIT. It had often been questioned whether or not EIT would even be possible in semiconductors, due to the high decoherence rates relative to atomic systems. However, the observation of Rabi oscillations in semiconductors [15] strongly suggested that this decoherence could be overcome. Furthermore, effects of nonradiative coherences have been studied

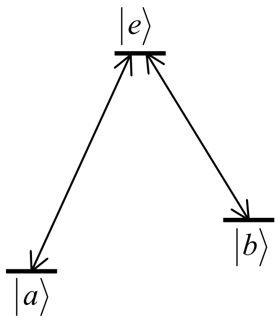

FIGURE 1. Example three-level system in which EIT may be observed. The arrows indicate allowed dipole transitions.

previously in semiconductor systems, although not at field intensities high enough to observe EIT [16–19]. There have been a few theoretical proposals indicating that EIT should be possible in semiconductor systems [20–24]; however, experimental verification has been largely unsuccessful. EIT effects have been demonstrated in semiconductor systems using the far-infrared intraband transitions [22]. However, there have not previously been demonstrations of EIT using the more useful optical frequency interband transitions.

Optical excitations in semiconductors can often be qualitatively understood through analogy with atomic-like systems. The process of exciting an electron to the conduction band from the valence band (leaving behind a hole in the valence band) can be approximated by an electric dipole transition. Furthermore, the lowest-energy optical transitions in direct gap semiconductors such as GaAs are dominated by excitonic effects. An exciton is formed when the Coulomb interaction between a negatively charged electron and positively charged hole leads to a bound state, much like an electron and proton form a hydrogen atom. Therefore, it is

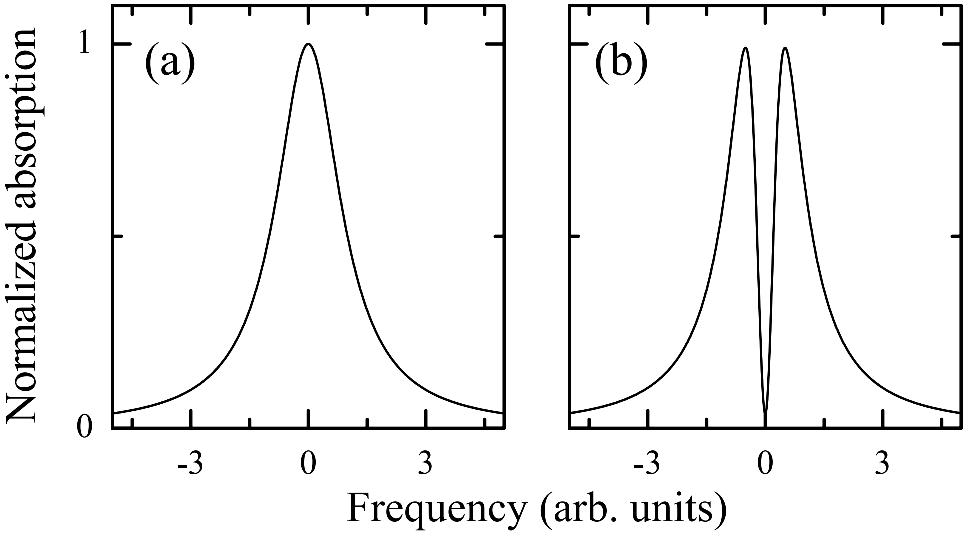

FIGURE 2. Example of EIT. (a) Calculated absorption spectrum for a two-level dipole transition. (b) Calculated absorption spectrum in three-level system showing EIT. The absorption becomes nearly zero at the center of the absorption peak, meaning the transition has become transparent at that frequency. The details of how these spectra are calculated will be discussed in Chapter II.

not surprising that excitonic transitions share many optical properties with atomic transitions.

While a correct theoretical treatment of the semiconductor system requires sophisticated models which include the effects of many-body interactions, in many situations the interaction of excitonic transitions with an optical field can be qualitatively described in terms of the simpler optical Bloch equations (OBE). With the addition of corrections to account for many-body effects, such a model can be used quite effectively to understand the nonlinear optical properties of exciton transitions. For example, these models have been used successfully to describe photon echo, four-wave mixing, and quantum beat experiments in semiconductors [25].

Regardless of the analogies between excitons and atoms, excitons are subject to effects and interactions simply not found in atomic systems. An optical transition in an atom corresponds to moving an electron between states within that atom. In contrast, an optical transition in a semiconductor corresponds to creating an exciton, not making transitions within an existing exciton. In an atomic system, the atomic density can be fixed regardless of any incident fields. However, in a semiconductor, the density of excitons depends strongly on the incident field which excites them. With increasing exciton density comes increased exciton-exciton scattering, leading to effects such as excitation induced dephasing (EID) [26], in which the dephasing rate of dipole transitions depends on the exciton density.

Another consequence of the strong exciton-exciton interaction is the formation of many-exciton states. For example, bound and unbound biexciton states may be formed via the Coulomb interactions between two excitons, much like molecules can be formed from atoms. The existence of biexciton states has been found to have dramatic effects on the optical properties of semiconductors. In addition to biexcitons, states made up of larger numbers of excitons may also be formed; however, so far biexcitons have been found to have the largest effect on the optical properties.

Including these exciton-exciton interactions into rigorous theoretical models of semiconductors is challenging, but significant progress has been made. The semiconductor Bloch equations (SBE) [27] model optical interactions with semiconductors within the Hartree-Fock (HF), or mean-field, limit. HF theories such as this account for the electron-hole Coulomb interaction which leads to excitons, and also correctly describe exchange interactions. Models based on the SBE have been highly effective for understanding a wide variety of semiconductor phenomena. However, HF theories such as the SBE do not account for Coulomb correlations, the interactions beyond the mean-field limit. As effects of Coulomb correlations such as biexcitons have been explored by experiments, more sophisticated theories have been developed. The most successful theory is based on a microscopic model in which the correlations are classified by their order in the external optical field. The Dynamics Controlled Truncation Scheme (DCTS) [28] introduces a way to truncate the infinite series of correlation terms by limiting the field to a certain order. DCTS theories have been used to describe the optical properties of semiconductors, including biexcitonic effects, up to third order in the optical field, and in some cases up to fifth order. However, these perturbation approaches are computationally demanding, which has restricted their use so far to low orders of the optical field.

There exist a wide variety of highly nonlinear optical phenomena which cannot be explained properly using a perturbation expansion in the optical field. One such process is that of Rabi oscillation. It is well known from studies of both spin and atomic systems that when a resonant optical field is applied to a two-level transition, the probabilities of occupation in the states oscillate at a frequency which is proportional to the product of the electric field magnitude and the dipole moment of the transition [29]. While the related optical Stark shift has been studied extensively, Rabi oscillations of excitonic transitions in semiconductors have only recently been observed [15]. The counterpart of Rabi oscillations in the spectral domain, called either optical Stark splitting or Rabi splitting, has also been recently observed [30]. These important experiments show that even highly nonlinear optical phenomena in atomic systems can have analogs in excitonic systems, although it should be noted that the full effects of Coulomb correlations on exciton Rabi oscillations are not completely understood at this time.

These developments also provide motivation and justification for taking other highly nonlinear optical effects which have been observed in atomic systems, and extending their study to semiconductors. It is in this spirit which we attempt to apply the concepts of EIT to a semiconductor system. While analogy with atomic phenomena can help guide the experiments in semiconductors, it is the differences observed in the semiconductor system which will help lead to advances in theoretical understanding of many-body systems.

In this dissertation, we present experimental demonstration that EIT is indeed possible in semiconductors, and show EIT resulting from three distinct nonradiative coherences. The first example uses a nonradiative coherence between valence bands in order to cause EIT, which is based on a previous theoretical proposal. Although the choice of this system for EIT is the most obvious one, and we do successfully demonstrate weak EIT signatures, it turns out to be a poor choice for observing strong EIT effects. The problem with this system is the large decoherence rate for the valence band coherence. The decoherence is made even worse by the effects of EID caused by a large exciton population necessarily excited during the EIT experiment.

The second example of EIT is based on generating a nonradiative coherence between exciton spin states. This exciton spin coherence leads to strong EIT effects, which is interesting in and of itself. However, a more significant consequence of these experiments is that it demonstrates an example of a nonradiative coherence which is only possible due to the presence of many-body biexciton states. We further show that the exciton spin coherence can be induced through unbound biexciton states, in addition to bound states. Instead of being a hindrance in this case, the exciton-exciton interactions allow for EIT to be realized in ways not possible in noninteracting atomic systems.

The third example of EIT again uses biexciton states, but this time to generate directly a biexcitonic coherence between the ground and bound biexciton states. The advantage of this system is that we can avoid the excitation of a large exciton population, which causes additional decoherence and limits the strength of EIT observed in the first two examples. Using this system, we are able to demonstrate a factor of twenty reduction in the absorption of an exciton resonance.

In addition to demonstrating that strong EIT effects are possible using excitonic transitions, we also use the experimental results to explore how correlations affect the quantum coherences in the system. By studying the effects of varying the experimental parameters, we use the EIT experiments as a spectroscopic tool to access the properties of nonradiative coherences. As noted before, one significant result is that nonradiative quantum coherences can be induced via exciton correlations. We also discover an energy shift of the biexcitonic coherence which is a direct consequence of exciton correlations. The properties of these nonradiative coherences are easily discerned from the large changes to the absorption caused by EIT.

Some qualitative aspects of our experiments may be understood through analogies with atomic systems, such as the basic mechanism for EIT arising from a nonradiative coherence. Other aspects, such as the correlation-induced coherences, are unique to a many-body system. In order to fully describe these experimental results, a theory will need to include the effects of Coulomb correlations on the optical nonlinearities. This combination represents a considerable challenge to current theoretical approaches, although progress is being made. The experiments presented here have already led to a collaboration [31] which has advanced the sophistication of theoretical models. It is hoped that these and future experiments will lead to even greater understanding of the physics of many-body systems.

The organization of this dissertation is as follows. Chapter 2 introduces the phenomenon of EIT in an atomic-like three-level system using a theoretical model based on the OBE. We begin by exploring analytical solutions to the OBE for steady-state excitation conditions. We then present numerical simulations of the equations showing that EIT may also be observed using pulsed excitation. Chapter 3 discusses the optical properties of excitons and biexcitons in semiconductors, which will be necessary to understand the experimental results. In Chapter 4, we briefly describe our experimental setup and methods. Chapter 5 presents experimental results showing Rabi splitting of exciton transitions. We use the results for two purposes. First, we show that the observation of Rabi splitting indicates that we can generate pump intensities of the correct magnitude to observe EIT. Second, we investigate how many-body correlations affect Rabi splitting in semiconductors. The next three chapters are devoted to experimental demonstrations of EIT in semiconductors. Chapter 6 discusses EIT based on a valence band coherence. Chapter 7 shows how exciton correlations may be used to generate an exciton spin coherence which leads to EIT. In Chapter 8, we explore strong EIT effects caused by a biexcitonic coherence. Finally, Chapter 9 is a summary of both the experimental results and the understanding of many-body physics we have gained from them.

CHAPTER II

ELECTROMAGNETICALLY INDUCED TRANSPARENCY

As described in the Introduction chapter, Electromagnetically induced transparency (EIT) is a process whereby quantum interference causes an otherwise absorbing optical transition to become transparent. In this chapter, we will discuss the details of how EIT occurs in various atomic-like three-level systems. We will see that EIT depends on the generation of a nonradiative coherence in the system, and that EIT may be used as spectroscopic tool both to probe for the existence of and to determine the properties of such nonradiative coherences.

EIT may occur in any configuration of three-level system; the three types are called Λ, *cascade*, and V systems as shown in Fig. 3. In this chapter, we will focus on the Λ system with states $|a\rangle$, $|b\rangle$, and $|e\rangle$, where the $|a\rangle \leftrightarrow |e\rangle$ and $|b\rangle \leftrightarrow |e\rangle$ are dipole transitions coupled by electric fields $\mathcal{E}_a$ and $\mathcal{E}_b$, respectively, as shown in Fig. 4. The $|a\rangle \leftrightarrow |b\rangle$ transition is not allowed via a dipole transition, but is allowed via a two-photon transition through the excited state.

Optical Bloch Equations for the Λ System

To describe the interaction of the electric fields with the three-level system, we use a model based on solving the optical Bloch equations (OBE). The semiclassical OBE describe the interaction of a quantum system with classical light fields. Solutions to the OBE for a two-level system interacting with a monochromatic light field are well-known and can be found in almost any quantum optics

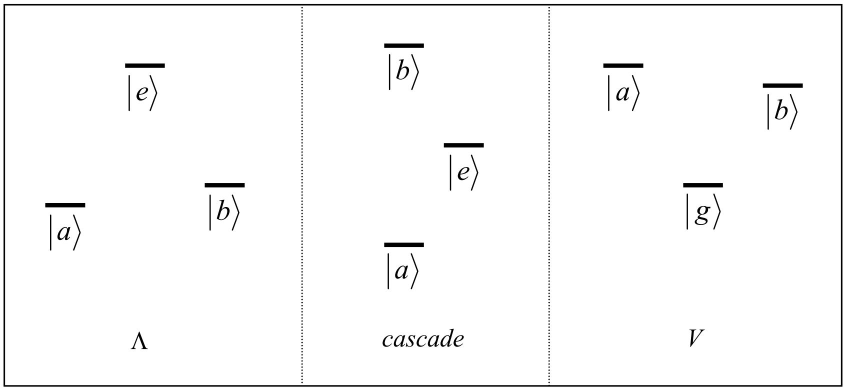

FIGURE 3. Types of three-level systems.

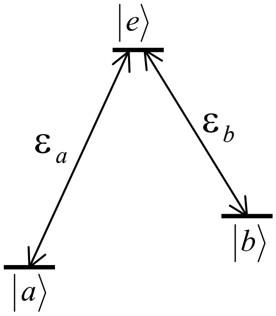

FIGURE 4. Λ system with electric fields applied to dipole transitions.

textbook. Solutions for three-level systems are more difficult to find, but are discussed in a few references [4, 29]. Exact analytical solutions are often possible if the applied fields are assumed monochromatic, and this limit is discussed most commonly in the literature. In some cases, an analytical solution can be obtained by assuming the incident fields have a delta-function temporal shape [25]. As will be discussed later, our experimental realizations of EIT in semiconductors require the use of temporally long pulsed excitation in the range where neither a quasi-CW approximation nor a delta-function pulse shape is valid, so exact solutions of the OBE are generally not possible. Therefore, we must rely on numerical solutions to the OBE, using temporal pulse shapes approximating those used in our experiments.

For the three-level system and the two applied fields, the Hamiltonian consists of two parts, the atomic Hamiltonian $\mathcal{H}_0$, describing the free evolution of the atomic states, given by

$$\mathcal{H}_0 = \hbar \begin{pmatrix} \omega_{ee} & 0 & 0 \\ 0 & \omega_{aa} & 0 \\ 0 & 0 & \omega_{bb} \end{pmatrix} \tag{2.1}$$

and an interaction Hamiltonian V, describing the interaction between the atomic dipole transitions and the electric fields, given by

$$V = - \begin{pmatrix} 0 & \mu_a \mathcal{E}_a & \mu_b \mathcal{E}_b \\ \mu_a \mathcal{E}_a & 0 & 0 \\ \mu_b \mathcal{E}_b & 0 & 0 \end{pmatrix} \tag{2.2}$$

where μ_a and μ_b are the components of the dipole matrix elements $\vec{\mu_a} = \langle a | e\vec{r} | e \rangle$ and $\vec{\mu_b} = \langle b | e\vec{r} | e \rangle$ along the electric fields $\vec{\mathcal{E}_a}$ and $\vec{\mathcal{E}_b}$, respectively. For convenience, μ_a and μ_b are taken to be real.

The applied electric fields are given by

$$\mathcal{E}_a(t) = \frac{1}{2}E_a(t)e^{-i\nu_a t} + c.c. \tag{2.3}$$

$$\mathcal{E}_b(t) = \frac{1}{2}E_b(t)e^{-i\nu_b t} + c.c. \tag{2.4}$$

which are real by construction. The quantities $E_a(t)$ and $E_b(t)$ are the slowly varying (relative to the optical frequencies ν_a and ν_b) amplitudes of the electric fields. For convenience, we will refer to the electric fields in terms of their Rabi frequencies Ω_a and Ω_b,

$$\Omega_a(t) = \frac{\mu_a E_a(t)}{\hbar} \tag{2.5}$$

$$\Omega_b(t) = \frac{\mu_b E_b(t)}{\hbar} \tag{2.6}$$

The state of the three-level system is given by a 3 × 3 density matrix of the form:

$$\rho = \begin{pmatrix} \rho_{ee} & \rho_{ea} & \rho_{eb} \\ \rho_{ae} & \rho_{aa} & \rho_{ab} \\ \rho_{be} & \rho_{ba} & \rho_{bb} \end{pmatrix} \tag{2.7}$$

The diagonal matrix elements ρ_{ee}, ρ_{aa}, and ρ_{bb} give the populations of levels $|e\rangle$, $|a\rangle$, and $|b\rangle$, respectively. The matrix elements $\rho_{ea} = \rho^*_{ae}$ and $\rho_{eb} = \rho^*_{be}$ describe the coherence for the dipole transitions. The matrix element $\rho_{ba} = \rho^*_{ab}$ describes the two-photon nonradiative coherence.

The equations of motion for the density matrix elements are derived using the time-evolution relationship $\dot{\rho} = \frac{i}{\hbar}[\rho, \mathcal{H}]$. We make the substitutions

$$\rho_{ea} = \tilde{p}_a e^{-i\nu_a t} \tag{2.8}$$

$$\rho_{eb} = \tilde{p}_b e^{-i\nu_b t} \tag{2.9}$$

$$\rho_{ba} = \tilde{p}_{ba} e^{i(\nu_b - \nu_a)t} \tag{2.10}$$

to factor out the rapidly varying components of the dipole coherences which oscillate at the optical frequencies. For convenience, we also make the following replacements:

$$\rho_{aa} = n_a \tag{2.11}$$

$$\rho_{bb} = n_b \tag{2.12}$$

$$\rho_{ee} = n_e \tag{2.13}$$

Using the Hamiltonian and the above substitutions for the density matrix elements we may derive the OBE for the Λ system. We drop rapidly varying and nonresonant terms by making the rotating wave approximation (RWA). We also set $n_a + n_b + n_e = 1$ to normalize the total level population to one. Finally, we introduce phenomenologically the decay of the the level populations and dipole coherences described by the density matrix elements. With these assumptions, we arrive at the following equations:

$$\dot{\tilde{p}}_a(t) = (i\delta_a - \gamma_a)\tilde{p}_a(t) - \frac{i\Omega_a(t)}{2}\left[1 - n_b(t) - 2n_a(t)\right] + \frac{i\Omega_b(t)}{2}\tilde{p}_{ba}(t) \tag{2.14}$$

$$\dot{\tilde{p}}_b(t) = (i\delta_b - \gamma_b)\tilde{p}_b(t) - \frac{i\Omega_b(t)}{2}\left[1 - n_a(t) - 2n_b(t)\right] + \frac{i\Omega_a(t)}{2}\tilde{p}_{ba}(t)^* \tag{2.15}$$

$$\dot{\tilde{p}}_{ba}(t) = \left[i(\delta_a - \delta_b) - \gamma_{ab}\right]\tilde{p}_{ba}(t) - \frac{i\Omega_a(t)}{2}\tilde{p}_b(t)^* + \frac{i\Omega_b(t)}{2}\tilde{p}_a(t) \tag{2.16}$$

$$\dot{n}_a(t) = \Gamma_a(1 - n_a(t) - n_b(t)) + \frac{i}{2}(\Omega_a(t)^*\tilde{p}_a(t) - c.c.) \tag{2.17}$$

$$\dot{n}_b(t) = \Gamma_b(1 - n_a(t) - n_b(t)) + \frac{i}{2}(\Omega_b(t)^*\tilde{p}_b(t) - c.c.) \tag{2.18}$$

where $\delta_a = \nu_a - \omega_a$ and $\delta_b = \nu_b - \omega_b$ give the detunings of the applied fields from the dipole transitions with energies $\omega_a = \omega_{ee} - \omega_{aa}$ and $\omega_b = \omega_{ee} - \omega_{bb}$, respectively. The terms γ_a and γ_b describe the dephasing of the dipole coherences, the terms Γ_a and Γ_b describe population relaxation from the state $|e\rangle$ into states $|a\rangle$ and $|b\rangle$, and the term γ_{ab} describes the decay of the nonradiative coherence between states $|a\rangle$ and $|b\rangle$.

We will assume state $|a\rangle$ is the ground state of the system, with no initial occupation of state $|b\rangle$, and will seek to measure EIT in the $|a\rangle \leftrightarrow |e\rangle$ transition. We assume that Ω_a is a weak probe beam, while we place no limitation on the strength of the pump Ω_b. Under these restrictions, we solve the OBE perturbatively up to first order in Ω_a. To zeroth order in Ω_a, $n_a^{(0)} = 1$, and all other terms are zero. Note that this is a direct consequence of states $|b\rangle$ and $|e\rangle$ being unoccupied in the absence of Ω_a, so that Ω_b is pumping on an "empty" transition. This would not be the case for a V system.

To first order in Ω_a, we obtain the following coupled equations:

$$\dot{\tilde{p}}_a^{(1)}(t) = (i\delta_a - \gamma)\,\tilde{p}_a^{(1)}(t) + \frac{i\Omega_a(t)}{2} + \frac{i\Omega_b(t)}{2}\tilde{p}_{ba}^{(1)}(t) \tag{2.19}$$

$$\dot{\tilde{p}}_{ba}^{(1)}(t) = \left[i\left(\delta_a - \delta_b\right) - \gamma_{ab}\right]\tilde{p}_{ba}^{(1)}(t) + \frac{i\Omega_b(t)^*}{2}\tilde{p}_a^{(1)}(t) \tag{2.20}$$

where we have replaced γ_a by γ, since the dipole decoherence rate for the $|b\rangle \leftrightarrow |e\rangle$ transition does not enter the equations. These two equations can be solved to find the response of the system to the pump and probe fields. Even before finding solutions, we can deduce some basic results from the equations. First, if the pump field is absent, we set $\Omega_b = 0$ and find that Eqn. 2.19 reduces to the result for the linear response of a two-level system. Likewise, if we set $p_{ba} = 0$ so that there is no nonradiative coherence, we get the same result. Therefore, any changes in the absorption spectrum can be traced directly back to the presence of the nonradiative coherence. Second, looking at Eqn. 2.20 confirms that the nonradiative coherence requires that both Ω_b *and* Ω_a act on the system (because $\tilde{p}_a^{(1)} \propto \Omega_a$). Though this is not surprising based on the fact that the excitation $|a\rangle \leftrightarrow |b\rangle$ requires a two-photon transition, it is still important to keep in mind when interpreting the solutions to the equations.

Additional details relating to the derivation of the OBE for each configuration of three-level system are given in Appendix B. In the next two sections, we will solve the OBE we have derived for the Λ system first under steady-state conditions, and second under transient conditions more appropriate for our semiconductor experiments.

Steady-State EIT Solutions

Before proceeding to solve these equations numerically, it is useful to review the analytic solutions for steady-state excitation conditions. We are interested primarily in the absorption spectrum $\alpha(\delta_a)$ of the probe field, which is calculated from the relation: $\alpha \propto \mathrm{Im}\left[\frac{\tilde{p}_a^{(1)}}{\Omega_a}\right]$. Solving the above equations 2.19 and 2.20 for $\tilde{p}_a^{(1)}$ in the steady-state limit yields:

$$\tilde{p}_a^{(1)} = \frac{-\frac{i\Omega_a}{2}\left[i\left(\delta_a - \delta_b\right) - \gamma_{ab}\right]}{\left(i\delta_a - \gamma\right)\left[i\left(\delta_a - \delta_b\right) - \gamma_{ab}\right] + \frac{|\Omega_b|^2}{4}} \tag{2.21}$$

from which the absorption spectrum of the probe is readily calculated.

In Fig. 5 we plot as the solid line the probe absorption spectrum for the conditions $\gamma_{ab} = 0.01\gamma$, $\delta_b = 0$, and $\Omega_b = \gamma$. Throughout this dissertation, when plotting theoretical results we will reference all time and frequency parameters to the dipole decoherence rate γ. We also plot as the dotted line the absorption spectrum for the probe in the absence of the pump, i.e. the linear absorption. As can be seen in Fig. 5, the pump field has a dramatic effect on the absorption spectrum, leading to a narrow region of almost complete transparency at $\delta_a = 0$.

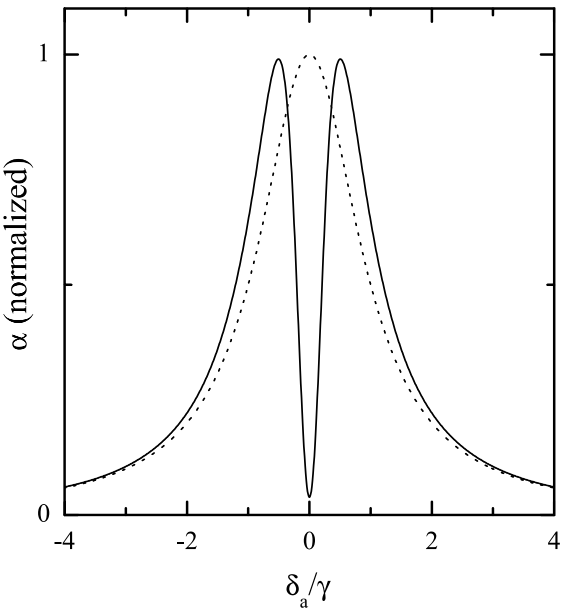

FIGURE 5. EIT in the absorption spectrum of the probe for steady-state excitation. The solid line is the normalized absorption of the probe as a function of the probe detuning δ_a, calculated from Eqn. 2.21 with $\gamma_{ab} = 0.01\gamma$, $\delta_b = 0$, and $\Omega_b = \gamma$. The dashed line is the linear absorption spectrum of the probe.

The change in absorption lineshape has been interpreted in several manners, including explanations drawing on the dark state in the system and explanations based on interference in the absorption to states dressed by the pump field [3]. For the purposes of this dissertation, however, it will be useful to understand the EIT absorption lineshape based on the effects of the nonradiative coherence in the OBE. In Eqn. 2.19, it is the imaginary part of the equation that determines the absorption spectrum of the probe. In the absence of the pump, the term $\frac{i\Omega_a}{2}$ leads to absorption. The term $\frac{i\Omega_b}{2}\tilde{p}_{ba}^{(1)}$ can counteract this absorption if its imaginary part is negative, which occurs for $\mathrm{Re}[\tilde{p}_{ba}^{(1)}] < 0$. The magnitude of the nonradiative coherence comes from Eqn. 2.20, which to a first approximation gives a resonance with width γ_{ab} centered at $\delta_a = \delta_b$. It is this resonance condition for the nonradiative coherence which leads directly to the EIT dip in Fig. 5. Because the driving term in Eqn. 2.20 is nonlinear in Ω_b, higher pump strengths lead to larger regions in the absorption spectrum over which the nonradiative coherence has an effect. In Fig. 6 we show that as the pump field strength Ω_b is increased, the EIT dip gets progressively broader.

The spectra shown in Fig. 6 for higher pump intensities appear to resemble the sum of two Lorentzian peaks centered at $\delta_a = \pm\Omega_b/2$. Indeed, these peaks reflect the strong absorption to the states of the $|b\rangle \leftrightarrow |e\rangle$ transition dressed by the pump field. However, note that the absorption at $\delta_a = 0$ approaches zero, a result which is not consistent with the sum of two positive resonances. The EIT lineshape reflects the destructive interference cause by the nonradiative coherence.

The resonance condition for the nonradiative coherence can be further demonstrated by changing the pump detuning δ_b. As shown in Fig.7(a), the minimum absorption occurs at a spectral position given by $\delta_a = \delta_b$. The EIT dip also begins to look more dispersive in lineshape. For larger values of γ_{ab}, the EIT dip does not occur exactly at $\delta_a = \delta_b$, as shown in Fig.7(b). This same behavior may also occur for smaller values of Ω_b.

The resonance condition for the nonradiative coherence reflects the two-photon nature of the $|a\rangle \leftrightarrow |b\rangle$ transition. As shown by the diagram in Fig. 8(a),

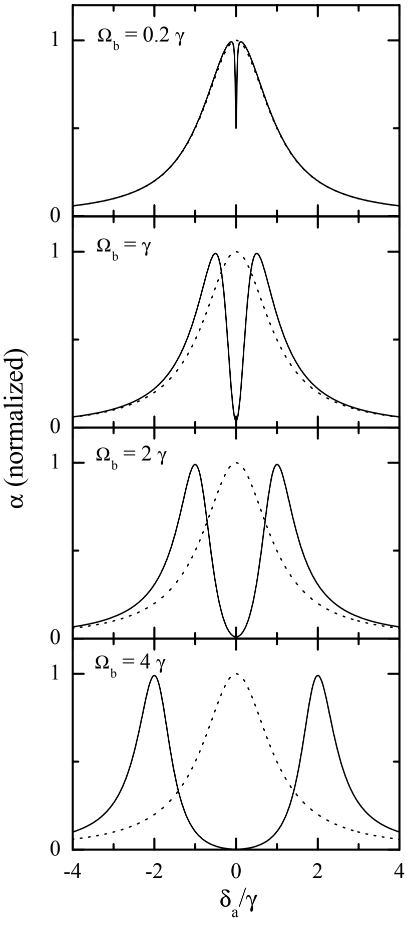

FIGURE 6. Dependence of the EIT spectrum on the pump strength. Absorption spectra are plotted for the values of Ω_b given in the figure, and with $\gamma_{ab} = 0.01\gamma$ and $\delta_b = 0$.

the transition from $|a\rangle \leftrightarrow |b\rangle$ is resonant when the detunings of the pump and probe are equal. Therefore, the largest magnitude of the nonradiative coherence will be generated for the resonance condition $\delta_a = \delta_b$. Although we have limited our discussion to a Λ configuration so far, we should also discuss the two-photon resonance condition for the V and *cascade* systems. As shown in Fig. 8(b), the resonance condition for the V system is the same as for the Λ system; however, as shown in Fig. 8(c), the resonance condition is different for the *cascade* configuration, where it changes to $\delta_a = -\delta_b$.

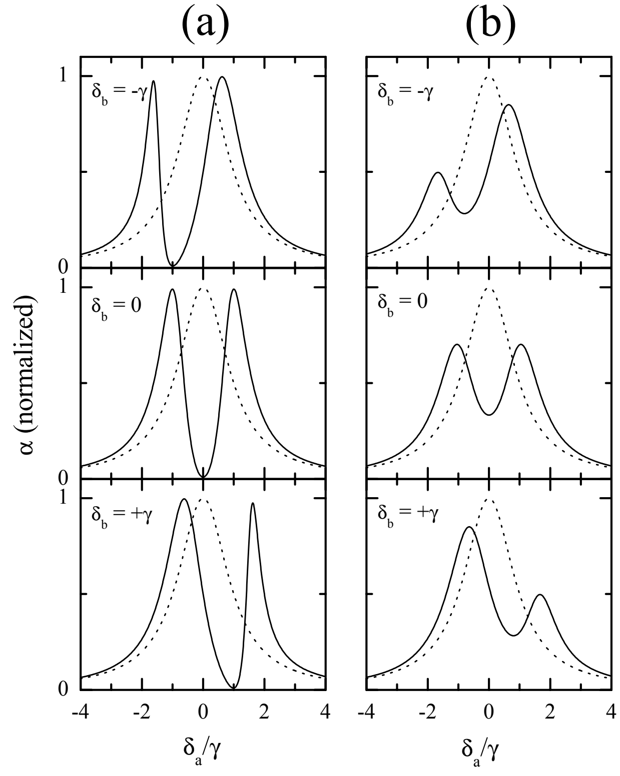

FIGURE 7. EIT spectra for different values of the pump detuning δ_b, and with $\Omega_b = 2\gamma$. For (a), $\gamma_{ab} = 0.01\gamma$ and for (b), $\gamma_{ab} = 0.5\gamma$.

For a given pump field strength Ω_b, the magnitude of the nonradiative coherence that can be generated is determined by the decoherence rate γ_{ab}. Figure 9 shows that this effect of changing γ_{ab} is reflected in the width and depth of the EIT dip in the absorption spectrum. In fact, if γ_{ab} is too large, indicating that no significant nonradiative coherence can be generated, then the EIT dip disappears entirely and the absorption spectrum reverts to that of linear absorption for a

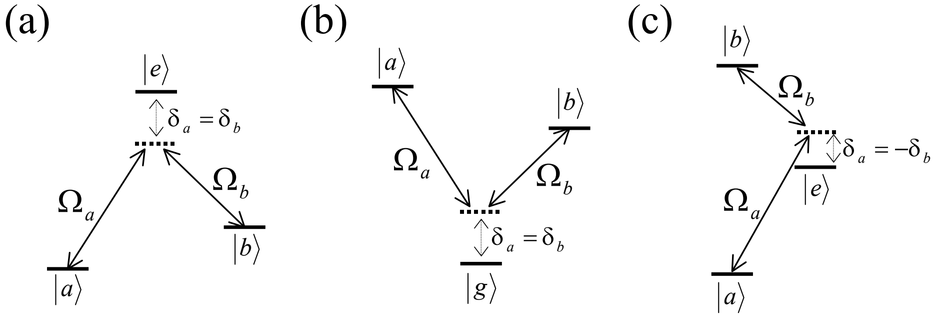

FIGURE 8. Resonance conditions for the two-photon transition between states $|a\rangle$ and $b\rangle$ for (a) Λ-system, (b) V-system, and (C) *cascade*-system.

two-level system.

As the above graphs show, simply applying pump and probe to a three-level system does not guarantee that an EIT signature will be observed in the probe absorption spectrum. We can derive a general condition for the observation of EIT from Eqn. 2.21. Setting $\delta_b = 0$, the absorption reduction for $\delta_a = 0$ is given by the ratio

$$\frac{\alpha\left(\delta_a = 0\right)}{\alpha_0} = \frac{1}{1 + \frac{|\Omega_b|^2}{4\gamma\gamma_{ab}}} \tag{2.22}$$

where α_0 is the absorption at $\delta_a = 0$ for $\Omega_b = 0$. In order to achieve greater than 50 percent reduction in absorption, we therefore must meet the requirement $|\Omega_b|^2 > 4\gamma_a\gamma_{ab}$.

For completeness, we should also point out that the large changes in the absorption spectrum associated with EIT have corresponding effects in the index

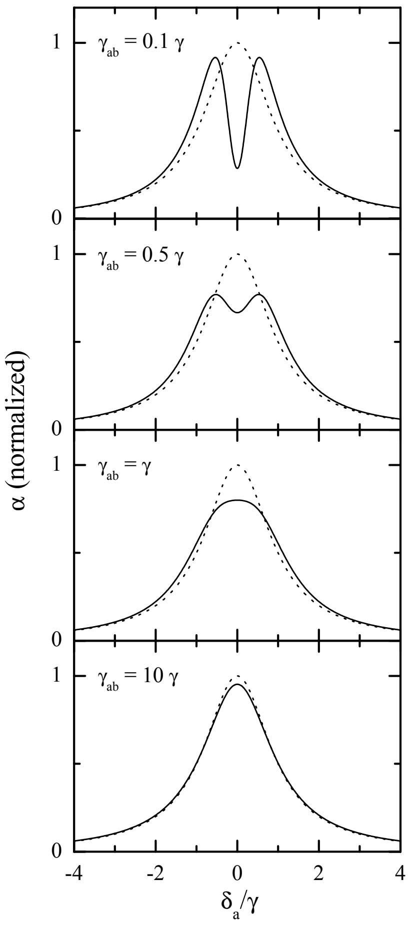

FIGURE 9. EIT spectra for different values of the decoherence rate γ_{ab}. For all curves, $\delta_b = 0$, and $\Omega_b = \gamma$.

of refraction. In Fig. 10 we show the index of refraction as a function of δ_a both for a two-level system, and for the Λ system with the same parameters as for Fig. 5. When EIT is present, the index of refraction changes the sign of its slope and can become very steep. These changes have been used to demonstrate slowing of the group velocity of light pulses [5–7]. Although the results discussed in this dissertation focus on the changes to the absorption spectrum caused by EIT, the corresponding changes to the index of refraction are also necessarily present.

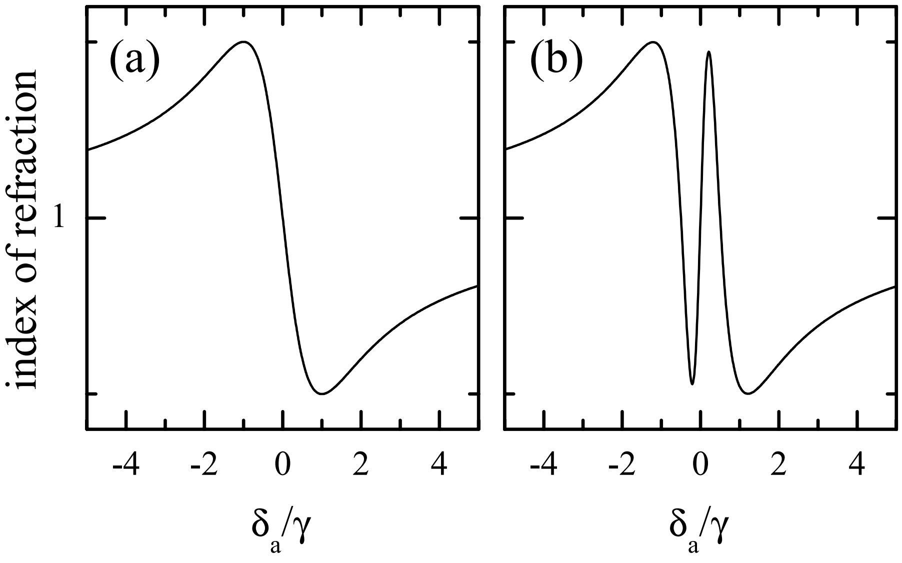

FIGURE 10. Index of refraction as a function of probe detuning for (a) two-level system, and (b) Λ-system when EIT is observed in absorption spectrum. For (b), the parameters are the same as for Fig. 5.

Transient EIT Solutions

In this section, we will look at solutions to the OBE in Eqns. 2.19 and 2.20 when the pump and probe fields are given by pulses. Despite our best efforts, we could not observe EIT in semiconductors under CW excitation conditions, due to a large increase in decoherence rates caused by scattering from a steady-state exciton population. However, we found that EIT signatures could be experimentally observed using pump pulses of a few picoseconds duration and probe pulses of 150 femptoseconds duration. In this section, will show that EIT signatures appear in the solutions to the OBE for these transient excitation conditions used in our experiments.

The numerical modeling was performed using Mathematica. The coupled differential equations given in Eqns. 2.19 and 2.20 were solved numerically using a fourth-order Runge-Kutta routine, with Gaussian temporal pulse shapes for $\Omega_a(t)$ and $\Omega_b(t)$ (the exact pulse shape was found to have no significant effect on the results, as long as it varied smoothly in time). Fourier transforms of the functions $\tilde{p}_a^{(1)}(t)$ and $\Omega_a(t)$ were taken to give $\tilde{p}_a^{(1)}(\delta_a)$ and $\Omega_a(\delta_a)$. The absorption spectrum was then calculated using the relation $\alpha \propto \mathrm{Im}\left[\frac{\tilde{p}_a^{(1)}(\delta_a)}{\Omega_a(\delta_a)}\right]$. The resulting spectrum was normalized so that the peak value of the linear absorption equaled one. The Mathematica script used for the simulations is included in Appendix C.

To confirm that the simulation gives the correct results for the absorption of a two-level system subject excited by a short probe pulse, we plot the numerical solutions for both $\mathrm{Im}[\tilde{p}_a^{(1)}(t)]$ in Fig. 11(a), and the corresponding absorption spectrum in Fig. 11(b), for $\Omega_b = 0$. The polarization $\mathrm{Im}[\tilde{p}_a^{(1)}(t)]$ is initially excited by the short probe pulse and then decays exponentially at the dipole decoherence rate γ. As long as the probe duration is short compared with the dipole dephasing time, the initial spike in $\mathrm{Im}[\tilde{p}_a^{(1)}(t)]$ represents a small fraction of the total signal and the spectrum is determined primarily by the slow decay. This is equivalent to requiring that the spectral bandwidth of the probe pulse be large compared with the absorption linewidth we wish to measure. The numerically calculated absorption spectrum for the short probe pulse shown in Fig. 11(b) matches the analytically calculated Lorentzian absorption resonance obtained for CW excitation plotted in Fig. 11(c). The width of the absorption resonance is determined by the dipole decoherence rate, with the full-width at half-maximum given by 2γ.

The Lorentzian line shape simply reflects the Fourier transform of the exponential decay of $\mathrm{Im}[\tilde{p}_a^{(1)}(t)]$.

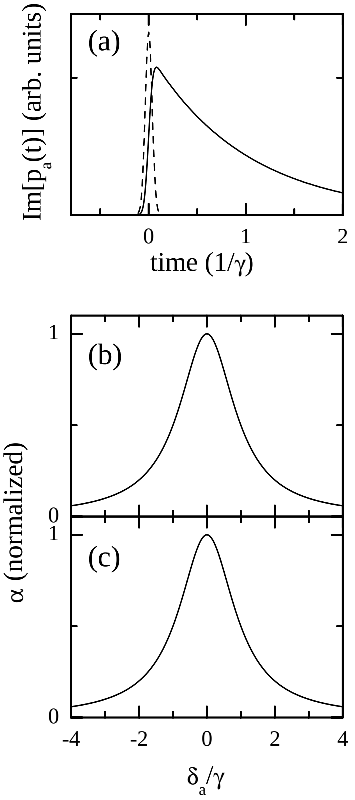

FIGURE 11. Numerical solutions of OBE for a two-level system excited by a short probe pulse of duration $.1\gamma^{-1}$. (a) Time dependence of $\mathrm{Im}[\tilde{p}_a^{(1)}(t)]$ (solid curve). The dashed curve gives the probe amplitude Ω_a(t). (b) Numerically calculated absorption spectrum (c) Theoretical linear absorption spectrum for two-level system measured by CW probe.

Having verified that a short (compared with the dipole decoherence time) probe pulse can be used to obtain the correct absorption spectrum for a two-level system, we turn next to the EIT situation. In the experiments, our first inclination was to use shorter pump pulses in order to make the pump Rabi frequency as high as possible. However, an analysis of the OBE shows that longer pump pulses are actually better. In Eqn. 2.19 determining the time evolution of $\tilde{p}_a^{(1)}(t)$, the term which leads to the EIT dip in the absorption spectrum, $\frac{i\Omega_b(t)}{2}\tilde{p}_{ba}^{(1)}(t)$, contains a factor of $\Omega_b(t)$. Therefore, when $\Omega_b(t) = 0$, there will be no effect at that time on the absorption of the $|a\rangle \leftrightarrow |e\rangle$ transition, regardless of the magnitude of the nonradiative coherence. To maximize the effects of the nonradiative coherence on the $|a\rangle \leftrightarrow |e\rangle$ transition, the pump pulse should be as long as possible. Here, we choose a pump duration of $10\gamma^{-1}$, which is long compared with the dipole decoherence time, but still short enough to be experimentally practical.

In Fig. 12 we present numerical results showing EIT in the probe absorption spectrum for these pulsed excitation conditions, with $\gamma_{ab} = 0.01\gamma$, $\Omega_b = \gamma$ at its peak, and with the probe arriving at the peak of the pump pulse. The absorption spectrum shows a distinct EIT dip which appears similar to that observed for CW pumping conditions. To understand better the origin of the EIT signature for pulsed excitation, it is useful to look directly at the time dependence of the solutions for $\mathrm{Im}[\tilde{p}_a^{(1)}(t)]$ and $\mathrm{Re}[\tilde{p}_{ab}^{(1)}(t)]$, which are plotted in Fig. 13. The decay of $\mathrm{Im}[\tilde{p}_a^{(1)}(t)]$ is modified by the presence of the pump field and the nonradiative coherence, which leads to the alteration of the absorption lineshape. Also note that the nonradiative coherence $\mathrm{Re}[\tilde{p}_{ab}^{(1)}(t)]$ is zero until both the pump and probe have arrived, and is negative for times after that, indicating that it leads to a reduction in absorption.

One parameter in the pulsed case which is not present in the CW case is the delay between the peaks of the pump and probe pulses, which we denote by τ. We define a positive pump-probe delay to mean that the probe arrives after the peak of the pump. Figure 14 shows absorption spectra for various pump-

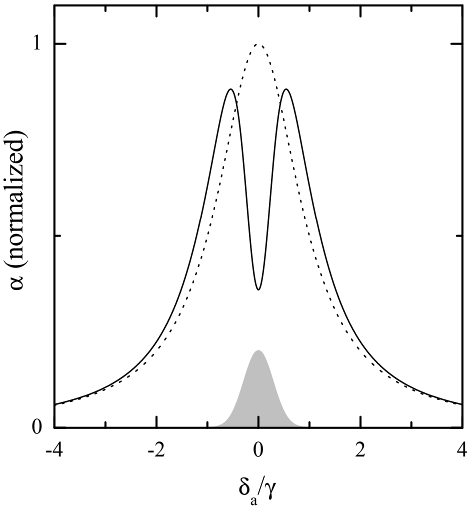

FIGURE 12. Calculated EIT absorption spectrum for pulsed excitation conditions. The probe and pump durations are $.1\gamma^{-1}$ and $10\gamma^{-1}$, respectively, and the probe arrives at the peak of the pump. Other parameters are $\gamma_{ab} = 0.01\gamma$, $\Omega_b(0) = \gamma$, and $\delta_b = 0$. The pump spectrum is plotted as the shaded area.

probe delays. The depth of the EIT dip is strongly dependent on the pump-probe delay, and the results are not symmetric about $\tau = 0$. The EIT dip appears at relatively large negative delays, and is deepest when the probe slightly precedes the pump. The EIT dip disappears rapidly for positive delays. This behavior can be understood by examining the temporal behavior of $\mathrm{Im}[\tilde{p}_a^{(1)}(t)]$, which is shown in Fig. 15 for the same pump-probe delays as in Fig. 14. Also plotted is the temporal behavior of the product $\mathrm{Re}[\tilde{p}_{ab}^{(1)}(t)]\Omega_b(t)$, which gives the strength of the nonradiative coherence term which leads to EIT. For large negative delays, $\mathrm{Im}[\tilde{p}_a^{(1)}(t)]$ has decayed significantly even before the arrival of the pump. Because most of this decay has a simple exponential dependence, and also because the nonradiative coherence term is small, the effects of EIT in the absorption spectrum

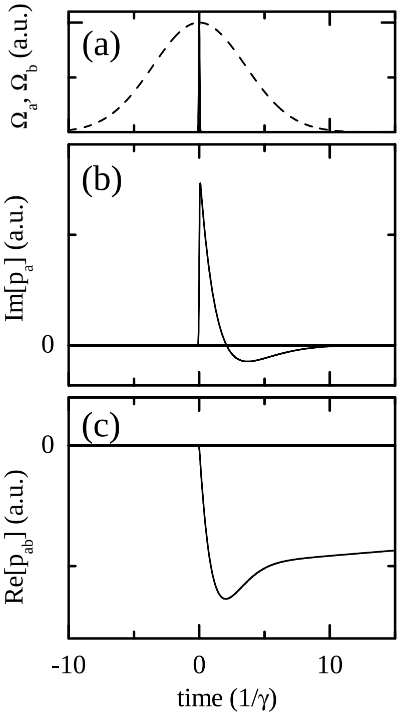

FIGURE 13. Numerical solutions for $\mathrm{Im}[\tilde{p}_a^{(1)}(t)]$ and $\mathrm{Re}[\tilde{p}_{ab}^{(1)}(t)]$ under pulsed excitation conditions of Fig. 12. (a) Timing of pump and probe pulses. The probe $\Omega_a(t)$ is the solid curve and the pump $\Omega_b(t)$ is the dashed curve. (b) Time dependence of $\mathrm{Im}[\tilde{p}_a^{(1)}(t)]$. (c) Time dependence of $\mathrm{Re}[\tilde{p}_{ab}^{(1)}(t)]$.

are small. For slightly negative delays, $\mathrm{Im}[\tilde{p}_a^{(1)}(t)]$ is affected by the nonradiative coherence term over its entire decay, leading to a strong EIT signature in the absorption. If the probe arrives after the peak of the pump, there is not sufficient pump amplitude to generate a large nonradiative coherence term, and again the decay of $\mathrm{Im}[\tilde{p}_a^{(1)}(t)]$ has a primarily exponential dependence.

As it was for the CW excitation conditions, the depth of the EIT dip is strongly dependent of the decoherence rate for the nonradiative coherence. Figure 16 shows absorption spectra for various values of γ_{ab}. At a certain point,

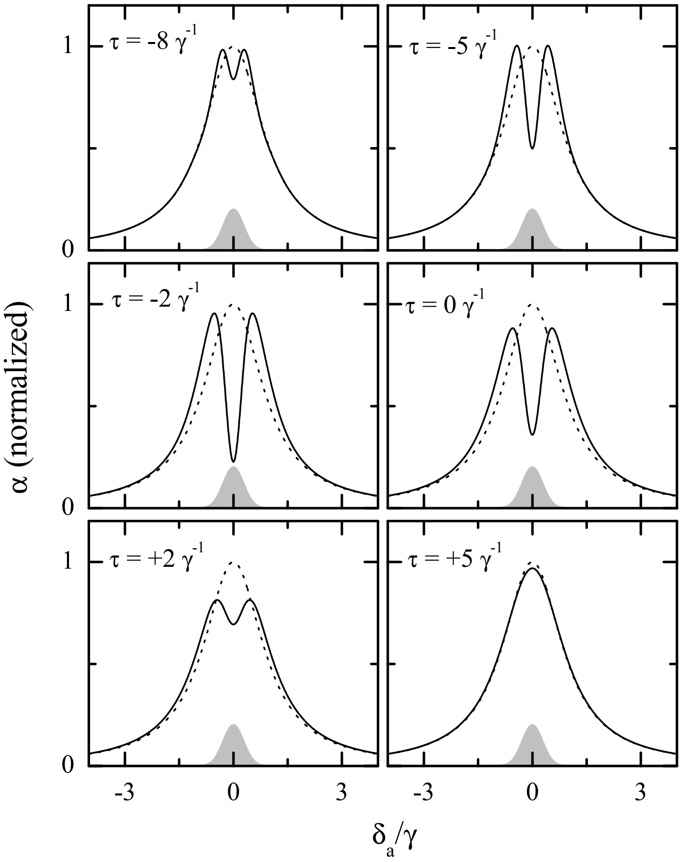

FIGURE 14. EIT absorption spectra for the pump-probe delays τ indicated in the figure. Other parameters are the same as for Fig. 12.

decreasing γ_{ab} has little effect on the width of the EIT dip. For the pulsed excitation case, the pump duration sets a limit on the width of the observed EIT dip, so that decreasing γ_{ab} below the pump spectral bandwidth has no effect on the EIT dip. This result again arises from the fact that the changes to the probe absorption due to EIT are dependent on the product of the nonradiative coherence and the pump field amplitude. If the pump pulse reaches zero amplitude before the nonradiative coherence does, then the pump is the limiting factor.

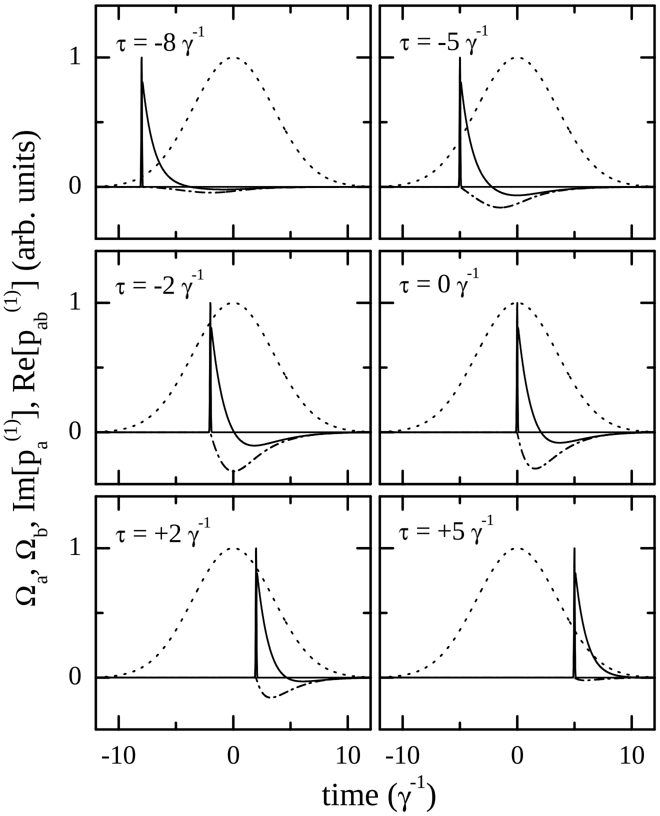

FIGURE 15. Time dependence of $\mathrm{Im}[\tilde{p}_a^{(1)}(t)]$ (solid), $\mathrm{Re}[\tilde{p}_{ab}^{(1)}(t)]\Omega_b(t)$ (dash-dot), and $\Omega_b(t)$ (dashed) for the same pump-probe delays as in Fig. 14. Other parameters are the same as for Fig. 12.

Minimum Requirements to Observe EIT Using Pulsed Excitation

In this section, we summarize the requirements we will need to meet in order to observe EIT in a semiconductor system, under worst-case conditions. The requirement can be broken up into two categories, those dealing with the three-level system under investigation, and those dealing with the applied optical fields. The properties of the semiconductor system we will be investigating will be discussed in the next chapter. For now, we will assume that we can find a suitable analog

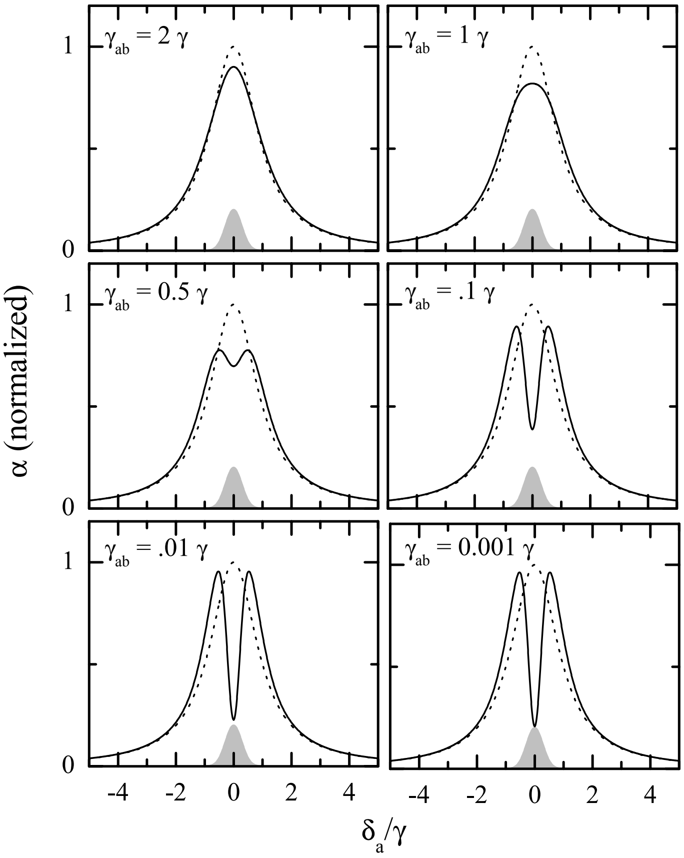

FIGURE 16. Effects of the decoherence rate γ_{ab} on the EIT absorption spectrum. The values of γ_{ab} are indicated in the figure, and other parameters are the same as for Fig. 12, but with $\tau = -2\gamma^{-1}$.

to a three-level system in which a nonradiative coherence can be generated. If we find such a three-level system, it is possible the nonradiative coherence will have a high decoherence rate. At worst, the decoherence will be dominated by scattering-induced dephasing, in which case we would expect $\gamma_{ab} \sim \gamma$.

Even for this non-ideal system, it should still be possible to observe EIT signatures as long as the pump field strength is high enough. As discussed above, for the pulsed experiment the pump duration should be long relative to the dipole decoherence rate. Furthermore, the pump-probe delay should be set to slightly negative values. Using the condition for observation of EIT under CW pump and probe, Eqn. 2.22, with $\gamma_{ab} = \gamma$, indicates that we will need pump fields strong enough that $\Omega_b \sim \gamma$. In Fig. 17 we plot the absorption spectrum for pulsed excitation, with $\gamma_{ab} = \gamma$, and for various values of Ω_b. It can be seen from the figure that the condition for observation of EIT in this non-ideal system under pulsed excitation is the same as for CW excitation: $\Omega_b \sim \gamma$. As this is the same condition for the pump to induce Rabi oscillations in the $|b\rangle \leftrightarrow |e\rangle$ transition, we will discuss in Chapter V our experiments to show that this condition can be reached in a semiconductor system.

This chapter has discussed the basic properties of EIT in a Λ-type three-level system. For both CW and pulsed pump and probe, the appearance of an EIT dip directly indicates the presence of a nonradiative coherence in the system. This nonradiative coherence causes destructive interference in the transition pathways of the system, leading to a region of transparency in the probe absorption spectrum. As a spectroscopic tool, an experiment to measure EIT can also be used to deduce properties of the underlying nonradiative coherence. In particular, the behavior of the EIT dip under varying experimental conditions can give information about the decoherence rate of the nonradiative coherence, which may not be otherwise accessible.

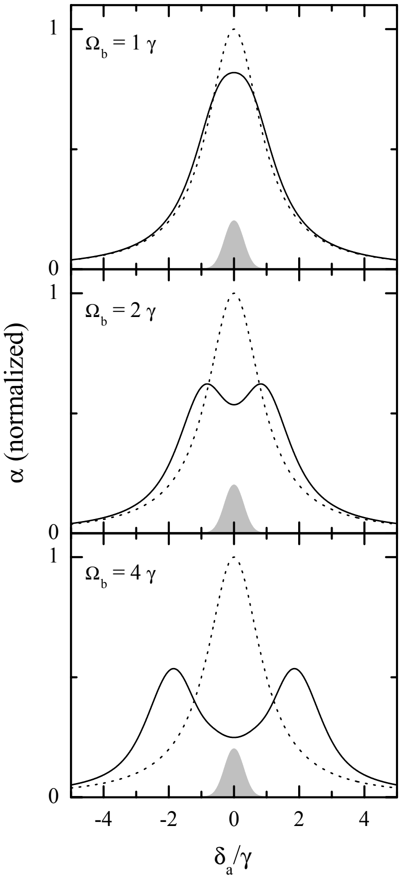

FIGURE 17. Minimum requirements for EIT in non-ideal system with $\gamma_{ab} = \gamma$. The absorption spectrum is plotted for the values of Ω_b indicated in the figure. Other parameters are the same as in Fig. 12, but with $\tau = -2\gamma^{-1}$.

CHAPTER III

EXCITONS AND BIEXCITONS IN SEMICONDUCTOR QUANTUM WELLS

Optical Excitations in Semiconductors

This chapter will introduce the basic concepts necessary to understand our optical studies of excitonic transitions in semiconductors. There are many excellent reference works on linear and nonlinear optical properties of semiconductors [25, 27, 32–34], from which much of the discussion in this chapter draws. We will first discuss the extent to which exciton transitions may be modeled as atomic-like transitions. We will then turn to the effects of exciton correlations, and biexcitons in particular, to demonstrate some of the differences between excitonic and atomic systems. While much of the discussion is general, we will give specific parameters for GaAs when appropriate, as this is the system in which the experiments were performed.

In a semiconductor, optical transitions are made by exciting an electron from the valence band to the conduction band, creating a positively charged hole in the valence band. The energy separation between the top of the valence band and the bottom of the conduction band is given by the band gap E_g, and in direct gap semiconductors such as GaAs, the band extrema occur at the Brillouin zone center $k = 0$ (where k is the crystal momentum). While electrons can be excited for energies above the band gap, we will be concerned here with the lowest energy transitions near the band extrema.

The wavefunctions for electrons in the valence band or conduction band are given by Bloch functions $\psi_c(k,r)$ and $\psi_v(k,r)$, where $\psi_j(k,r) = e^{ik\cdot r}u_j(k,r)$ and $j = c, v$. The periodic functions $u_j(k,r)$ are solutions to the Schrödinger equation:

$$\left[-\frac{\hbar}{2m_0}\nabla^2 + \frac{\hbar}{m_0}k\cdot p + V_0(r)\right]u_j(k,r) = \left[E_j(k) - \frac{\hbar^2k^2}{2m_0}\right]u_j(k,r) \tag{3.1}$$

where m_0 is the electron mass and V_0 is the periodic crystal potential.

Since we are interested in the optical properties of the semiconductor, we consider the matrix elements of the dipole operator $\mu = er$ between a state in the valence band $|v,k\rangle$ and a state in the conduction band $|c,k'\rangle$. It can be shown that:

$$\mu_{cv} = \langle c,k'|\mu|v,k\rangle = \frac{ie}{m_0(E_c(k') - E_v(k))}\delta_{k,k'}p_{cv} \tag{3.2}$$

where p_{cv} is the matrix element of the momentum operator. This result assumes that the photon momentum is small, which is equivalent to requiring the optical field wavelength to be large compared with the lattice spacing (the electric dipole approximation). The delta function in this expression indicates that dipole transitions are allowed between valence band states and conduction band states which have the same k.

The oppositely charged electrons and holes interact with each other via the Coulomb potential, which leads to the formation of excitons. The wavefunction Ψ of an electron-hole pair state can be written as a linear combination of electron and hole Bloch wavefunctions:

$$\Psi = \sum_{k_e, k_h} C(k_e, k_h)\psi_{k_e}(r_e)\psi_{k_h}(r_h) \tag{3.3}$$

When the Coulomb interaction is then introduced into the Hamiltonian, the problem reduces to that of the hydrogen atom, or more correctly the positronium atom. The center of mass motion of the electron and hole obeys the equation for a plane wave and gives energies $E_K = \frac{\hbar K^2}{2M}$, where M is the sum of electron and hole masses: $M = m_e + m_h$. The relative motion of the electron and hole satisfies the Wannier equation:

$$\left[-\frac{\hbar^2}{2\mu}\nabla_r^2 - \frac{e^2}{\epsilon_0 r}\right]\phi(r) = E\phi(r) \tag{3.4}$$

where $\mu = (m_e^{-1} + m_h^{-1})^{-1}$ is the reduced electron-hole mass.

The energies and wavefunctions for the relative e-h motion are therefore given by solutions of the hydrogen atom. The bound exciton energies form a hydrogenic series with the lowest energy state reduced from the band gap energy by the exciton binding energy. The higher energy exciton states merge into a continuum with energies at the band gap and above.

With the e-h Coulomb interaction included, we find that the linear susceptibility is given by

$$\chi(\nu) \propto |\mu_{cv}|^2 \sum_n \frac{|\phi_n(r=0)|^2}{E_n - \hbar\nu - i\gamma} \tag{3.5}$$

where the sum is over all bound and continuum exciton states with energies E_n. The factor $|\phi_n(r = 0)|$ indicates that the oscillator strength for a given exciton transition is proportional to the probability that the electron and hole are created in the same location. It also indicates that only the hydrogenic s states contribute to the absorption, as they are the only states with nonzero probability at $r = 0$. The linear absorption spectrum is therefore given by a series of bound exciton resonances and a continuum absorption beginning at the band gap energy. The strongest absorption is to the 1s exciton state, with a wavefunction and energy given by:

$$\phi_{1s}^{3D} = \frac{1}{\pi^{1/2} a_B^{3/2}} e^{-r/a_B} \tag{3.6}$$

$$E_{1s}^{3D} = E_g - R \tag{3.7}$$

in three-dimensions and

$$\phi_{1s}^{2D} = \left(\frac{2}{\pi}\right)^2 \left(\frac{2}{a_B}\right) e^{-2r/a_B} \tag{3.8}$$

$$E_{1s}^{2D} = E_g - 4R \tag{3.9}$$

in two-dimensions. In GaAs, the exciton Bohr radius a_B is 16 nm, and the exciton Rydberg energy R is 4.2 meV.

If we treat the excitons as independent particles, we may also regard the optical transitions which excite them as atomic-like electric dipole transitions between discrete states. In this case, the two states correspond to the presence and the absence of an exciton. The excitonic transitions are characterized by a transition energy, a dipole matrix element and a decay rate for the optical dipole coherence. An exciton can also emit a photon and return to the ground state, a process contributing to a population relaxation rate. With these identifications, the interactions of the excitonic transition and the electric field can then be modeled using the optical Bloch equations (OBE). These simple models allow for simulations to be performed without being computationally prohibitive. For the experimentalist, these models represent an important tool for gaining understanding into the physical processes.

As noted in the Introduction chapter, there have been numerous theoretical models developed to more accurately describe the optical interactions with excitons and many-body systems. We should certainly not expect our simple OBE models, even with phenomenological many-body corrections, to fully account for the behavior of semiconductor systems. Nevertheless, we can use simple models to gain important physical insights into the optical interactions.

Quantum Wells

Quantum wells are layered semiconductor structures, typically grown by either molecular beam epitaxy or chemical vapor deposition. A single QW is formed when a thin layer of semiconductor material is sandwiched between two other semiconductors that have a higher bandgap. The lower bandgap material is called the well layer, and the higher bandgap materials the barrier layers. If the well layer is thin enough and the bandgap difference between the well and barriers is large enough, the motion of electrons in the quantum well is confined to a quasi-2D plane.

In our experiments, we have used QWs consisting of GaAs well layers and $Al_{0.3}Ga_{0.7}As$ barriers; a schematic diagram of such a QW is shown in Fig. 18(a). Electrons and holes are free to move in the plane of the QW (perpendicular to the growth direction) and their wavefunctions are described by Bloch functions. However, in the z-direction (parallel to the growth direction), the wavefunctions of the electrons and holes are strongly affected by the presence of the barriers. The wavefunctions in the z-direction are those for a particle in a box with finite barriers, and the energy levels split into discrete subbands. Figure 18(b) shows both the potential variation and the first few wavefunctions (assuming infinite barrier potentials) for independent electrons and holes in the z-direction.

In this dissertation, we are not concerned directly with studying the effects of confinement. Instead, we use QWs because of the advantages they provide over other semiconductor systems. By confining the electrons and holes to a quasi-2D layer with a thickness on the order of the exciton Bohr radius, the exciton binding energy is increased. As shown by Eqn. 3.9, the exciton binding energy increases by a factor of 4 for a perfect 2D system. This increased binding energy, typically near 10 meV (depending on the QW width), allows the bound exciton transitions to be studied separately from the unbound continuum transitions. An additional effect of the confinement is that the interactions between excitons are increased so that QWs provide an excellent environment for studying exciton correlation effects.

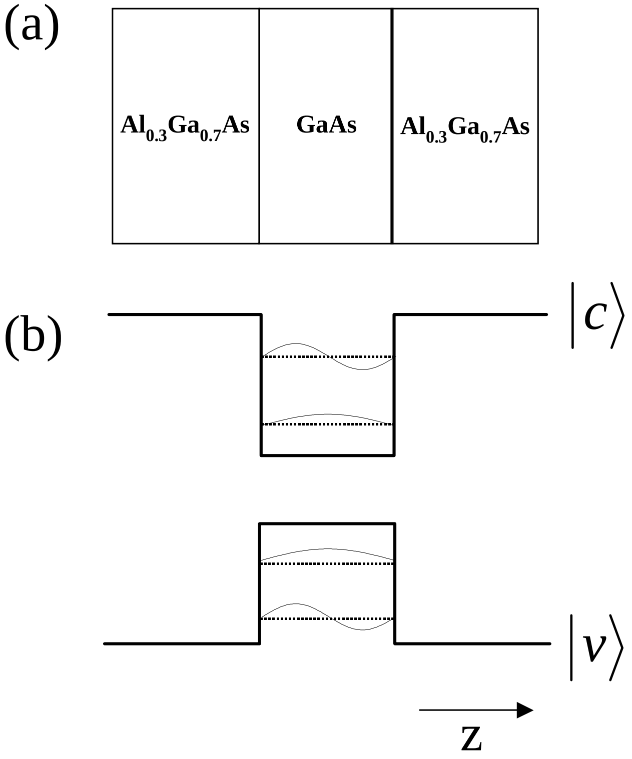

FIGURE 18. GaAs/AlGaAs quantum well. (a) Composition of layers making up the QW. (b) Potential variation in the z-direction (growth direction) and first few energy levels for in the conduction band $|c\rangle$ and valence band $|v\rangle$. The electron and hole wavefunctions shown assume an infinite confinement potential. Typical well widths are on the order of 10 nm.

Other confined structures can be grown and studied, including 0D quantum dots (QD). Even though QDs are the closest semiconductor analog to an atomic system, we have chosen to study QWs. There are a few reasons for this choice. First, current growth techniques for QDs lead to large fluctuations in the dot sizes, which in turn leads to a large inhomogeneous broadening in the the exciton transition energies. To overcome this inhomogeneous broadening, our experiments would have to be performed at the single-dot level, which is technically challenging.

On the other hand, if we can demonstrate that EIT is possible in a QW, then it will almost certainly be possible in a QD system as well. QWs also provide a more appropriate environment for studying the effects of correlations in a many-body system. Whereas correlation effects dominate the nonlinear optical properties in QWs, the confinement effects lead to the dominant nonlinearity in QDs.

In our experiments, we have primarily used three different QW structures. All are multiple QW (MQW) structures, meaning that the wells and barriers are repeated a number of times in the growth of the sample. For sufficiently wide barriers, the individual QWs behave independently, and this was the case for all our samples. All samples were grown by molecular beam epitaxy. The first sample has 17.5 nm wells and 15 nm barriers, with 15 periods, and was grown by J. E. Cunningham. The second sample has 13 nm wells and 15 nm barriers, with 8 periods, and was also grown by J. E. Cunningham. The third sample has 10 nm wells and 10 nm barriers, with 10 periods. This sample was obtained from D. G. Steel.

GaAs Band Structure

GaAs is a direct bandgap semiconductor, with an s-like conduction band and a p-like valence band. Electrons in the conduction band therefore have total angular momentum $J = 1/2$, while electrons in the valence band have $J = 3/2$ or $J = 1/2$. Spin-orbit coupling leads to a large energy splitting of the valence band according to the total angular momentum, but we will not be concerned with the split-off band with $J = 1/2$. Instead, we are interested in the valence band with $J = 3/2$ from which the lowest energy optical transitions occur.

The band structure is determined by the Hamiltonian, which we rewrite as:

$$\left[H_0 + \frac{\hbar}{m_0} k \cdot p\right] u_j(k,r) = \bar{E}_j(k) u_j(k,r) \tag{3.10}$$

where

$$H_0 = -\frac{\hbar}{2m_0}\nabla^2 + V_0(r) \tag{3.11}$$

and

$$\bar{E}_j(k) = E_j(k) - \frac{\hbar^2 k^2}{2m_0} \tag{3.12}$$

The band structure determined from the exact form of V_0 can be very complicated, and typically requires numerical solution. If we restrict our attention to near $k = 0$, however, we can simplify the description by making an effective mass approximation in which each band is assumed parabolic. This is accomplished using $k \cdot p$ theory to perform a perturbative expansion of the Hamiltonian up to second order in k. In this case:

$$E_j(k) = E_j(0) + \frac{\hbar^2 k^2}{2m^*} \tag{3.13}$$

where m^* is the effective mass determined by:

$$\frac{1}{m^*} = \frac{1}{m^0} + \frac{2}{k^2 m_0^2} \sum_{i \neq j} \frac{k \cdot \langle i|p|j \rangle k \cdot \langle j|p|i \rangle}{E_i(0) = E_j(0)} \tag{3.14}$$

For the conduction band in GaAs, the electron effective mass is calculated to be 0.067 m_0 [34]. For the degenerate valence bands with $J = 3/2$, the band structure near $k = 0$ can be approximated using the Luttinger Hamiltonian [27]:

$$H_L = \frac{\hbar}{2m_0} \left[(\gamma_1 + \frac{5}{2}\gamma_2)k^2 - 2\gamma_2 (k \cdot J)^2 \right] \tag{3.15}$$

where the Luttinger parameters γ_1 and γ_2 are constants adjusted to give the best match with experimental data.

The $k \cdot J$ term gives different effective masses for the band with $J_z = \pm 3/2$ and the band with $J_z = \pm 1/2$. For a 3D system with spherical symmetry, the calculation gives a heavy-hole (HH) band with $J_z = \pm 3/2$ and effective mass $m_{HH} = m_0(\gamma_1 - 2\gamma_2)^{-1}$, and a LH band with $J_z = \pm 1/2$ and effective mass $m_{LH} = m_0(\gamma_1 + 2\gamma_2)^{-1}$. In a 2D system, the z component of momentum must be separated from the in-plane momentum. In this case, the in-plane effective masses of the HH and LH are given by $m_{HH} = m_0(\gamma_1 + \gamma_2)^{-1}$ and $m_{LH} = m_0(\gamma_1 - \gamma_2)^{-1}$. The confinement potential also introduces an energy splitting between the HH and LH bands at $k = 0$ due to the different HH and LH effective masses in the z direction. Using the values of $\gamma_1 = 6.85$ and $\gamma_2 = 2.1$ for GaAs [34], the in-plane effective masses are calculated to be $m_{HH} = 0.112 m_0$ and $m_{LH} = 0.211 m_0$. A diagram of the band structure within the effective mass approximation near $k = 0$ is shown in Fig. 19 for both bulk GaAs and a GaAs QW.

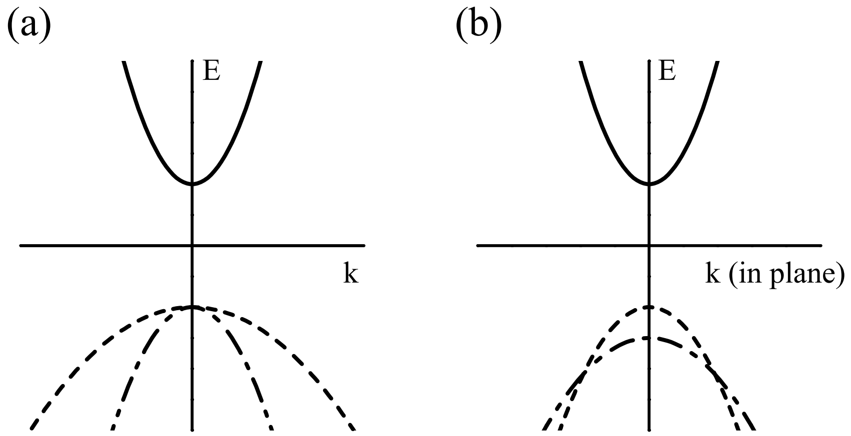

FIGURE 19. Band structure for (a) bulk GaAs and (b) GaAs QW, within the effective mass approximation. The solid line is the conduction band, the dashed line is the HH valence band, and the dot-dashed line is the LH valence band.

Note that in the QW, the HH and LH bands cross for some finite value of k, and our simplified band structure is incorrect. More detailed calculations give strong band mixing effects, where the identity of the bands becomes lost. Near $k = 0$, however, the band mixing is small and the HH and LH bands remain distinct.

In Fig. 20. we show explicitly the band energies for a GaAs QW at $k = 0$, labeled by J_z. In the figure, we also show the allowed optical transitions for either σ^+ or σ^- circularly polarized light, which carries an angular momentum of $J_z = \pm 1$. There are two HH transitions from the valence band states $J_z = \pm 3/2$ and two higher energy LH transitions from the valence band states with $J_z = \pm 1/2$.

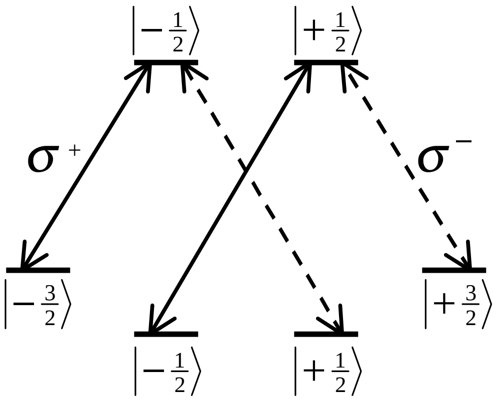

FIGURE 20. Band structure of GaAs QW at $k = 0$. The energy levels are labeled by the z-component of the total angular momentum $|J_z\rangle$. Allowed optical transitions for σ^+ polarized light are shown as solid arrows, while transitions for σ^- polarized light are shown as dashed arrows.

Exciton Absorption in GaAs QWs

Figure 21 shows the linear absorption spectrum at a temperature of 10K for the 17.5 nm MQW, obtained by using a weak probe beam with σ^+ polarization. The lowest energy 1s HH and LH exciton resonances give the strongest absorption, and the weaker 2s HH and LH exciton resonances are also visible. The other exciton bound states merge into the continuum absorption at the band edge. For convenience, we shall refer to the 1s exciton states as the HH and LH excitons, and not consider the 2s and higher states. The linewidth of the HH exciton is 0.3 nm, which is about twice as large as the linewidth in bulk GaAs [26], where the exciton transition is homogeneously broadened. The larger linewidth in the QW is primarily due to inhomogeneous broadening from fluctuations in the interfaces between the wells and barriers, but note that the increased linewidth due to inhomogeneous broadening is nevertheless small relative to the homogeneous linewidth observed for bulk GaAs.

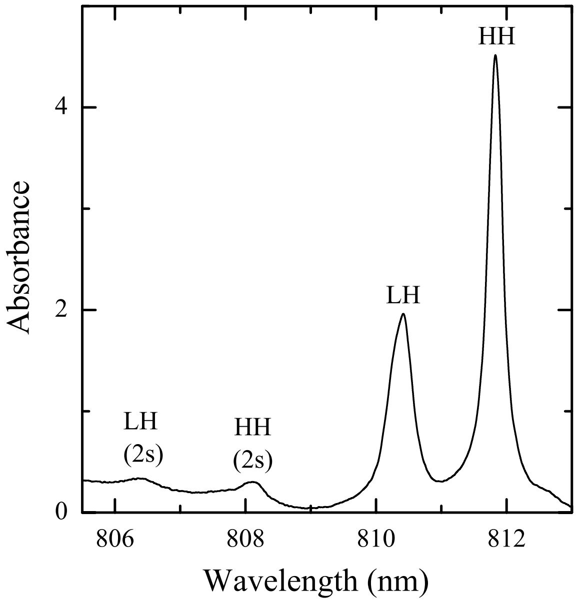

FIGURE 21. Linear absorption spectrum for the 17.5 nm GaAs MQW sample.

The linear absorption spectra for the 13 nm and 10 nm MQWs are shown in Figs. 22 and 23. A few effects of reducing the well width are apparent from comparing the spectra. The absorption resonances shift to shorter wavelengths, due to the change in width of the potential well. From observing the separation of the HH exciton resonance and the onset of continuum absorption, it can be seen that the exciton binding energy increases as the well width is reduced. The exciton linewidths broaden for narrower wells, because the relative effects of interface fluctuations are larger. Finally, the separation between HH and LH excitons increases as the well width decreases, though we should mention that the exact value of the HH-LH splitting is highly dependent on stresses in the sample.

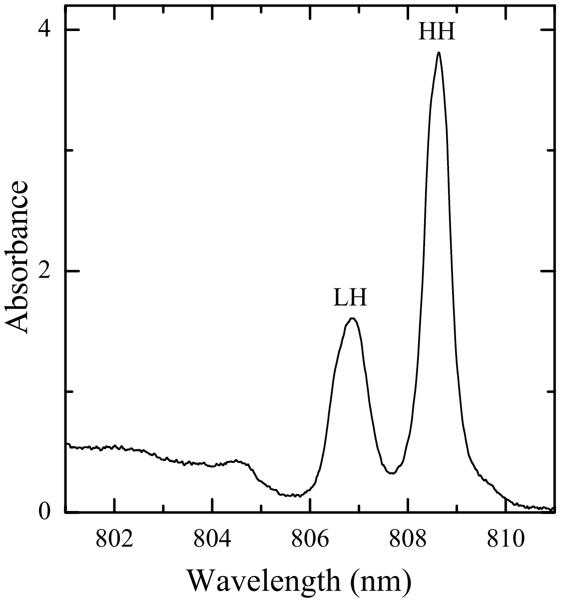

FIGURE 22. Linear absorption spectrum for the 13 nm GaAs MQW sample.

Decoherence times for the excitonic transitions (which determines the homogeneous linewidth) are typically on the order of a few picoseconds [25] at low temperature and low exciton densities. Since the exciton population relaxation times are long, on the order of hundreds of picoseconds [25], the decoherence rate is primarily due to collisional dephasing from phonons and other excitons. Performing experiments at low temperature reduces the effects of phonon scattering. We will discuss the effects of exciton-exciton scattering in the next section.

Exciton-Exciton Interactions

The dominant optical nonlinearity in atomic systems is due to saturation, or state-filling, in the sense that a two-level quantum system cannot be described by a harmonic oscillator model. In a semiconductor, band filling leads to non-

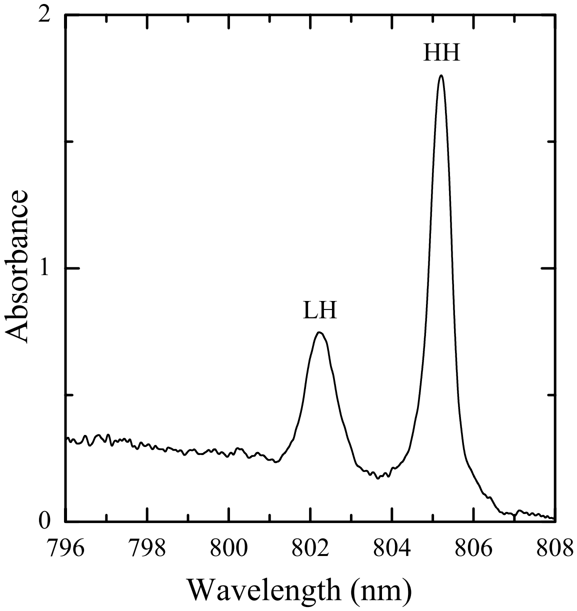

FIGURE 23. Linear absorption spectrum for the 10 nm GaAs MQW sample.

linearities; however, the interactions between excitons can also have significant effects. In particular, the optical properties can change dramatically depending on the density of excitons present. Two effects which we cannot ignore in our experiments are excitation-induced dephasing (EID), and also exchange interactions that lead to energy shifts. EID [26] refers to the increase in the decoherence rate for exciton transitions with increased exciton density. At higher exciton densities, the collisions between excitons are increased, which leads to increased collisional dephasing. In addition to increasing the linewidth of exciton absorption, EID also affects the nonlinear susceptibility [26], because the exciton density depends on the intensity of an incident electric field. EID effects can be added to an OBE model. To accomplish this, the dipole decoherence rate γ is replaced by $\gamma + \sigma n_{ex}$, where σ is a phenomenological factor representing the strength of EID, and n_{ex} is the exciton density.

In addition to the decoherence rate, the exciton transition shifts to higher energy as the exciton density increases, due to exchange interactions [35]. The exchange interactions which lead to this shift are included in the SBE, but they can also be modeled using corrections to the OBE. The interacting exciton system can be considered analogous to a dense dielectric medium in which the Lorentz local field replaces the externally applied field [36]. By replacing the electric field E with $E + LP$, where L is the Lorentz local field factor and P is the polarization induced in the system, the transition energy is shifted. In addition to a static shift, the local field correction leads to to a shift in the transition energy which depends on the exciton density.

The effects of both EID and exchange interactions can be seen in Fig. 24. The solid curve shows the absorption spectrum of a probe pulse in the presence of an exciton population which has been excited by a pump pulse. The probe measures the absorption at a time 10 ps after the pump has excited the system, so all coherent effects due to the pump have decayed. The HH exciton resonance is both broadened and shifted to higher energy relative to the absorption in the absence of the pump. Note that the increased linewidth of the exciton transition is due to *homogeneous* broadening, and indicates that the homogeneous linewidth is now larger than the previous inhomogeneous linewidth. Therefore, for experiments in which exciton densities are relatively high, it is often correct to treat the exciton transition as homogeneously broadened.

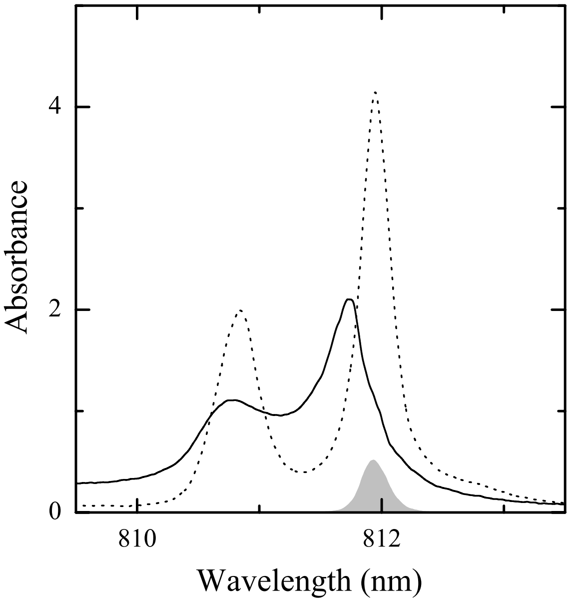

FIGURE 24. Effects of EID and exchange interactions. The curves shows the absorption spectra for a 150 fs probe pulse in the absence (dotted) and presence (solid) of a pump pulse having same circular polarization. The pump spectrum is shown as the shaded area. The pump duration is 6 ps, and the probe is delayed by 10 ps relative to the peak of the pump. The pump energy flux per pulse is 400 nJ/cm^2. The sample is the 17.5 nm MQW at 10 K.

Biexcitons

Another effect of the Coulomb interactions between excitons is the formation of bound or unbound biexcitons. Figure 25 shows the absorption spectrum of a probe pulse under the same conditions as in Fig. 24, except with the pump and probe having opposite circular polarizations. In this experiment, an absorption resonance appears at an energy lower than the exciton peak, which corresponds to a one-exciton to two-exciton transition in which a bound biexciton is formed. The transition energy for this process is smaller than the exciton transition energy by an amount equal to the biexciton binding energy.

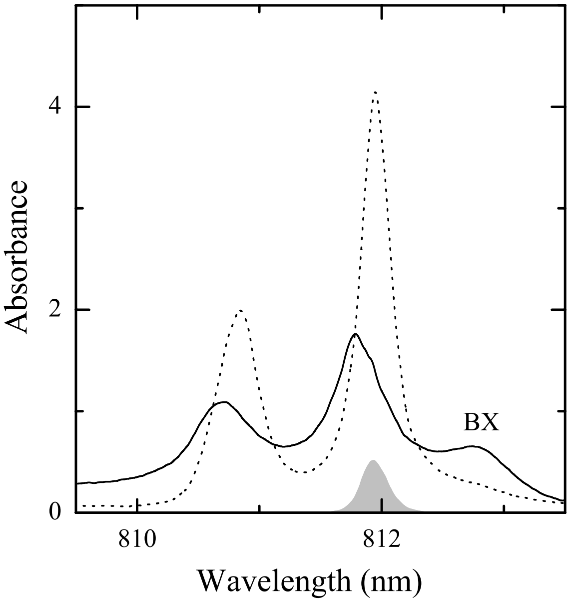

FIGURE 25. Biexciton-induced absorption. The curves shows the absorption spectra for a 150 fs probe pulse in the absence (dotted) and presence (solid) of a pump pulse, which has the opposite circular polarization. All other conditions are the same as for Fig. 24. The bound biexciton resonance is labeled by BX.

To form a bound biexciton, the two electron J_z states must be different from each other and the hole states must also be different from each other. As can be seen from Fig. 26, HH transitions excited by opposite circular polarizations meet this requirement. Therefore, if the pump pulse excites the σ^+ transition, bound biexcitons can only be formed when the probe excites the σ^- transition. In Fig. 24, when the pump and probe both excite the σ^+ transition, bound biexcitons cannot be formed; however, note that the absorption at energies slightly above the HH exciton is increased due to the formation of unbound biexcitons.

The above discussion applies to biexcitons formed by two HH excitons or by

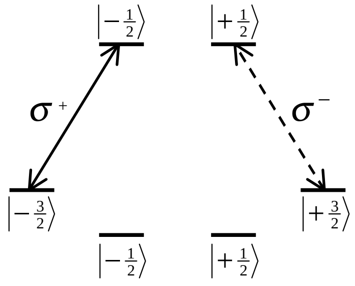

FIGURE 26. Selection rules for bound HH biexciton. If the pump (solid arrow) excites σ^+ HH excitons, a σ^- probe can excite bound biexcitons.

two LH excitons, but it is also possible to form so-called mixed biexcitons from one HH and one LH exciton [37, 38]. In Fig 27(a) we show differential absorption spectra (change in absorption induced by the pump) for the case where a pump is resonant with the HH exciton. Note that differential absorption measurements were necessary to see the small absorption changes for this case, where the experiment was performed with a weak pump pulse to allow for more direct comparison with a semiconductor theoretical calculation [38]. When the pump excites HH excitons, we observe a bound biexciton resonance for the pump and probe having opposite circular polarization, in agreement with our previous observations in Figs. 24 and 25. Figure 27(b) shows results when the pump is resonant with the LH exciton. In this case, a bound biexciton resonance is observed below the HH exciton for pump and probe having the *same* circular polarization. This mixed biexciton is formed when the probe excites a HH exciton into a biexciton state with a LH exciton which has been excited by the pump.

The different polarization selection rules for mixed biexciton formation can

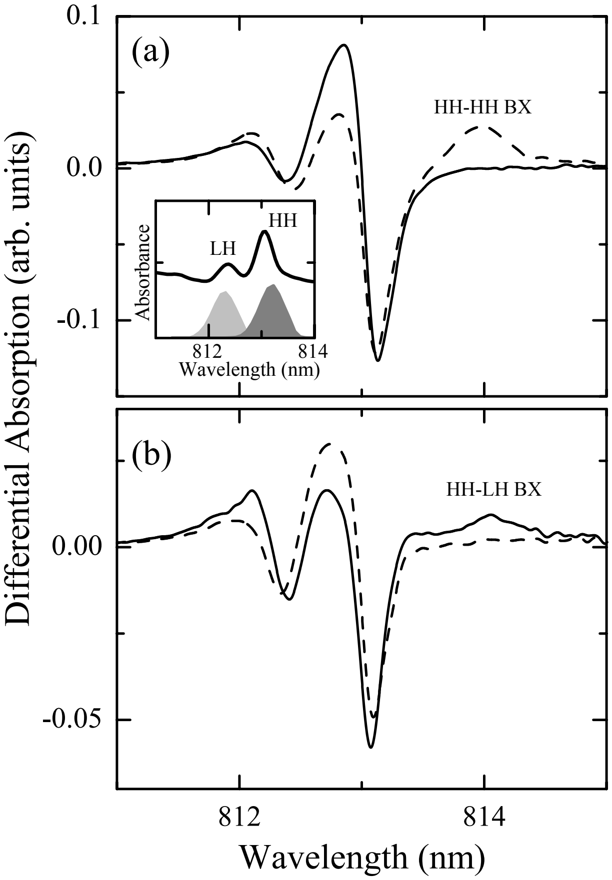

FIGURE 27. Mixed biexcitons. The curves show the differential absorption spectra for a 150 fs probe pulse in the presence of a pump pulse with the same (solid) and the opposite (dashed) circular polarization. The pump duration is 3 ps, and the pump-probe delay is 2 ps. The pump pulse energy flux is 6 nJ/cm^2. The inset shows the absorption spectrum for the sample, a 17.5nm single QW at 10 K, and also the pump spectra. (a) Pump resonant with HH exciton transition. (b) Pump resonant with LH exciton transition.

be understood by considering the electron and hole states, as shown in Fig. 28. If a σ^+ pump excites the LH transition, then it is the σ^+ HH transition which shares no common states. In this case, the mixed biexciton bound state is excited when the probe has the same circular polarization as the pump.

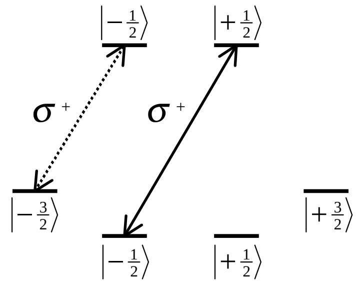

FIGURE 28. Selection rules for mixed HH-LH bound biexcitons. If the pump (solid arrow) excites σ^+ LH excitons, a σ^+ probe can excite mixed biexcitons.

While induced absorption into a bound biexciton state leads to the appearance of a resonance in the spectrum, the unbound biexciton states are also important. Figures 24 and 25 show an increased absorption at energies above the HH exciton, partly due to the energy shift due to exchange interactions, but also with contributions from unbound biexcitonic states. Both effects, however, arise from the exciton being excited into a state which is modified due to interactions with an existing exciton population.

The electron states shown in Fig. 20 are useful for determining the selection rules for biexciton formation, but we will also find it useful in the remaining chapters to describe the system in terms of N-exciton states. Figure 29 shows the states corresponding to zero, one, and two HH excitons. Transitions may be made in which a $|+\rangle$ or $|-\rangle$ exciton is created by a σ^+ or σ^- photon, respectively. We can also indicate exciton to biexciton transitions; for example, a $|+\rangle \rightarrow |+-\rangle_b$ transition with σ^- light corresponds to the formation of a bound biexciton.

To summarize this chapter, it can be beneficial to use the similarities between atomic and excitonic systems in order to understand the optical properties of

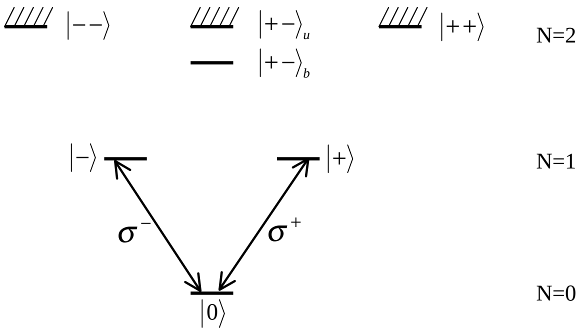

FIGURE 29. N-exciton states for HH excitons. The ground state is labeled by $|0\rangle$. The one exciton (N=1) states are denoted $|+\rangle$ and $|-\rangle$ for excitons excited by σ^+ and σ^- light, respectively. The 2-exciton states are the bound biexciton state $|+-\rangle_b$ and the unbound two-exciton continuum states $|+-\rangle_u$, $|--\rangle$, and $|++\rangle$.

a semiconductor. Even though the semiconductor is a many-body system, the exciton transitions can often be modeled as atomic-like, and the interactions with light described using the OBE with phenomenological corrections due to the many-body interactions. However, the exciton-exciton interactions cannot be completely ignored, and we will show in future chapters how the presence of biexciton states has a significant impact on the observation of EIT in semiconductors.

CHAPTER IV

EXPERIMENTAL SETUP

In this chapter, we will discuss the features of the experimental setup which are common to all the experiments presented in this dissertation.

Laser System

The laser system used for these experiments consisted of a mode-locked Ti:sapphire laser (Spectra-Physics Tsunami) pumped by a 10W argon-ion laser (Spectra Physics BeamLoc). The Ti:sapphire was typically run at a spectral bandwidth of 7-8 nm, and a pulse duration of 150 fs. The pulse repetition rate was 82 MHz. For 9.5 W input pump power, the average output power from the Ti:sapphire was approximately 1.5 W at 800 nm.

Pulse Shaper

To obtain spectrally narrow (and temporally long) pump pulses needed for the experiments, we used an external pulse shaper based on a design by David Alavi [39]. The pulse shaper consisted of a 1200 groove/mm diffraction grating, a 300 mm focusing lens, an adjustable slit, and a mirror, as shown in Fig. 30. The input beam was diffracted from the grating to spatially separate its frequency components. The diffracted beam was focused onto a mirror, with the lens placed one focal length from the grating and one focal length from the mirror, so that each frequency was focused to a point in the image plane (within the resolution limits of the system). A slit was placed between the lens and mirror in order to narrow the spectral bandwidth of the pulses; the slit was adjustable in both position and width. After reflecting off the mirror, the remaining spectral components of the beam returned through the lens to the grating where they were recombined. By introducing a small vertical tilt in the beam, the incident and filtered beam could be separated spatially.

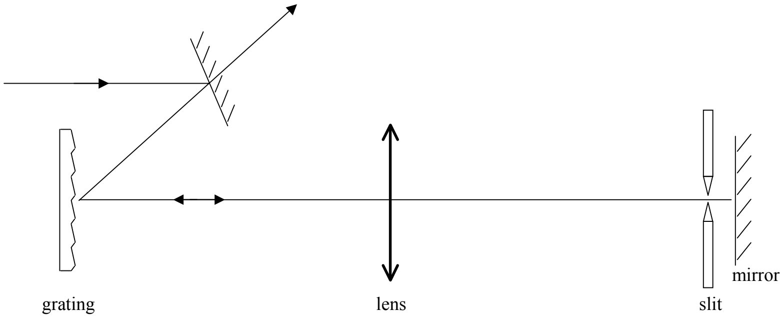

FIGURE 30. Schematic of the pulse shaper apparatus.

Alignment of the pulse shaper was important to avoid pulse broadening due to differing path lengths of the spatially separated spectral components. By adjusting the relative distances between the grating, lens, and mirror, nearly Fourier-transform limited pulses could be obtained. This was verified by measuring the spectral bandwidth using a spectrometer and the temporal width using autocorrelation or cross-correlation techniques. The shape of the filtered spectrum, specifically the steepness of the cutoffs, was adjusted by moving the position of the slit along the beam path. For the slit close to the mirror, a sharp cutoff was obtained. For the slit closer to the lens, a smoother cutoff was obtained, resulting in an approximately Gaussian spectrum and temporal pulse shape. The minimum filtered spectral bandwidth obtained with this setup was approximately 0.2 nm. Attempting to close the slit further resulted in an increase in spectral bandwidth due to spatial diffraction from the slit. For most of the experiments presented in this dissertation, the filtered pump widths were between 0.2 nm and 0.3 nm, with pulse widths of 5-6 ps, as measured by cross-correlation with the probe pulses.

Transient Pump-Probe Spectroscopy

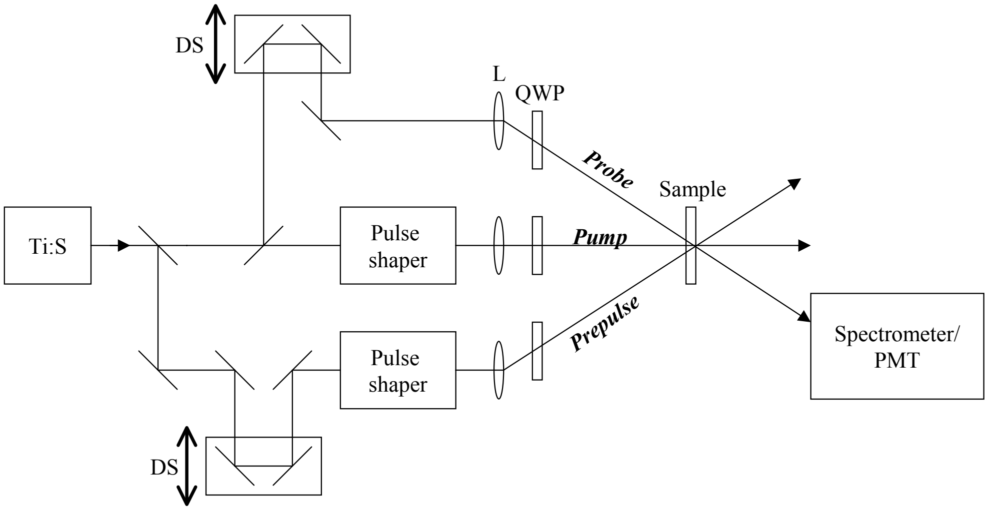

FIGURE 31. Schematic of the experimental setup. DS refers to a delay stage, L is a lens, and QWP is a quarter wave plate.

Figure 31 shows a schematic diagram of the experimental setup. The output from the Ti:sapphire laser was split into pump and probe beams. A third prepulse beam was split from the pump for the experiments in Chapter VII, and will be described further there. The pump pulses were spectrally filtered, as described above. The probe pulses were unfiltered. A scanning linear stage with 1 μm resolution was placed in the probe beam path to control the delay between pump and probe pulses. The zero delay position was set by measuring the cross-correlation of the pump and probe pulses using a LBO crystal to generate a nonlinear sum-frequency signal.

The output from the Ti:sapphire laser was linearly polarized. Circular polarizations of the pump and probe were generated using zeroth-order quartz quarter wave plates (QWP), optimized for use at 830 nm. By adjusting the QWPs, the pump and probe polarizations could be made co-circular ($\sigma^+\sigma^+$) or cross-circular ($\sigma^+\sigma^-$). Variations from circular polarization were less than 5%.

The pump and probe beams were focused onto the sample. Typical focused spot sizes were 3×10^{-5} cm^2 for the pump and 4×10^{-6} cm^2 for the probe, measured by scanning a 3 μm pinhole across the focused spots. It is important for the probe to be focused to a smaller size than the pump so that it samples only the central region of the pump spot, where the excitation level is more uniform. From the pump and probe spot sizes, it is estimated that the pump intensity varies by approximately 20% over the area of the probe spot.

The GaAs quantum well samples were held at a temperature near 10 K in a helium flow cryostat. The samples were etched to remove the thick GaAs substrate layer, and mounted on sapphire discs for transmission measurements. The probe beam transmitted through the sample was collected and sent through a spectrometer with 0.05 nm resolution. The resulting spectrally-resolved signal was detected using a photomultiplier tube. Absorption spectra in the presence or absence of the pump were calculated using the relationship:

$$\alpha(\lambda)L = -\ln\frac{I(\lambda)}{I_0(\lambda)} \tag{4.1}$$

where $\alpha(\lambda)$ is the absorption coefficient as a function of the probe wavelength λ, L is the thickness of the absorbing region of the sample, $I(\lambda)$ is the measured intensity of the probe after passing through the sample, and $I_0(\lambda)$ is the intensity of the probe before passing through the sample, approximated by measuring the probe spectrum when passed through the sapphire disc only. We will refer to the quantity αL as the absorbance when presenting experimental data.

CHAPTER V

RABI SPLITTING OF EXCITON TRANSITIONS

Rabi Oscillations and Splitting in Atomic Systems

The process of Rabi oscillation is discussed in quantum optics textbooks (Refs. [4, 29] for example), and is a direct consequence of the interaction of light with the discrete energy levels predicted by quantum mechanics. In Fig. 32, we consider an electric field $E\cos(\nu t)$ applied to a two-level system with ground state $|g\rangle$ and excited state $|e\rangle$, with transition frequency ω. A solution of this problem gives the well-known Rabi result [40]: the electron probability oscillates between the two states at the generalized Rabi frequency $\mathcal{R} = \sqrt{\delta^2 + \Omega^2}$, where $\delta = \nu - \omega$ is the detuning of the field, and $\Omega = \mu E/\hbar$ is the Rabi frequency. These Rabi oscillations are shown in Fig. 33(a). If we include effects of decoherence, then the Rabi oscillations decay at the dipole decoherence rate γ (for $\gamma >> \Gamma$, which is the situation in a semiconductor), as shown in Fig. 33(b). Therefore, in order to resolve Rabi oscillations, the condition $\mathcal{R} > \gamma$ must be met.

The Rabi oscillations introduce the frequency $\mathcal{R}$ into the dynamics of the system, which has effects in the spectral domain. In a resonance fluorescence measurement, where the fluorescence of the system under the influence of a resonant pump is measured, the original Lorentzian lineshape acquires sidebands at the Rabi frequency [29, 41], and is known as the Mollow triplet. The effects of Rabi oscillation can also be detected in absorption measurements. If the absorption spectrum of a CW probe field is measured in the presence of a CW pump field, the

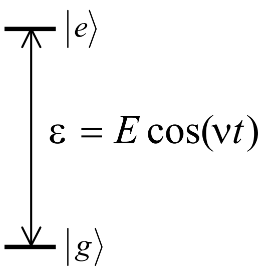

FIGURE 32. Light interacting with two-level system

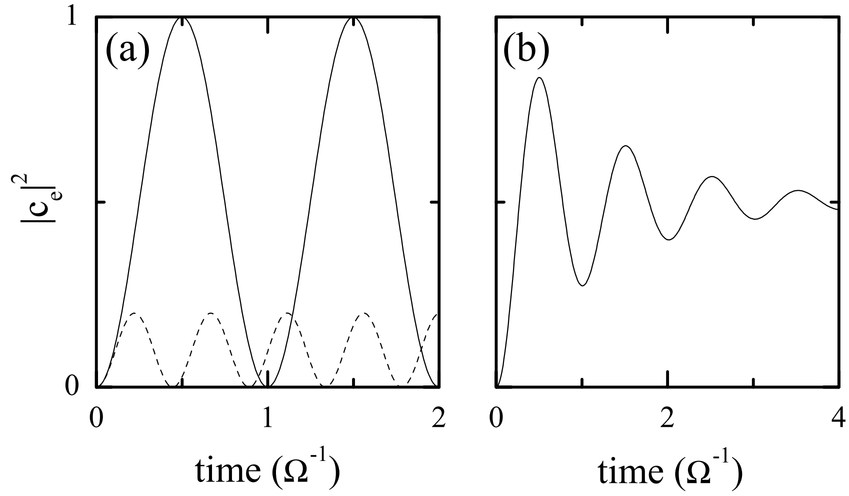

FIGURE 33. Rabi oscillations. The excited state population $|c_e|^2$ is plotted as a function of time. (a) Rabi oscillations with no decoherence. The solid line is for $\delta = 0$ and the dashed line is for $\delta = 2\Omega$. (b) Rabi oscillations with $\Omega = 4\gamma$ and $\gamma >> \Gamma$.

so-called Mollow spectra are obtained [29, 42, 43]. In general, the Mollow spectra represent complicated lineshapes where the response of the system at the Rabi frequency is introduced via wave-mixing of the pump and probe. By the term Rabi splitting, we shall refer to the modification of the absorption spectrum to include components at $\pm\mathcal{R}$. We should note that effects of Rabi splitting may appear in the absorption spectrum even if $\mathcal{R} < \gamma$ [29].

A closely related effect to that of Rabi splitting is that of the optical Stark effect [29, 44]. If the pump field is sufficiently detuned, so that $|\delta| >> \gamma$, then the resonance does not split, but instead shifts in the opposite direction as the pump detuning. For example, if the pump is tuned to a frequency lower than that of the transition, the transition will be shifted to a higher frequency. In addition to the shift in absorption, a gain peak also appears in the spectrum on the opposite side of the pump as the absorption.

The phenomena of Rabi oscillation, Rabi splitting, and the optical Stark effect can also be described using a model in which the quantization of the electric field is considered [45]. In this case, the pump and atom are described by the dressed states of the system. Both states $|g\rangle$ and $|e\rangle$ are mixed with the field states of n-photons to form doublets with energy separation $\mathcal{R}$, as shown in Fig. 34. The dressed states can be written as linear combinations of the uncoupled states $|e, n\rangle$ and $|g, n+1\rangle$:

$$|1, n\rangle = \sin(\theta)|e, n\rangle + \cos(\theta)|g, n+1\rangle \tag{5.1}$$

$$|2, n\rangle = \cos(\theta)|e, n\rangle - \sin(\theta)|g, n+1\rangle \tag{5.2}$$

where

$$\cos(\theta) = \frac{\mathcal{R} - \delta}{\sqrt{(\mathcal{R} - \delta)^2 + \Omega^2}} \tag{5.3}$$

$$\sin(\theta) = \frac{\Omega}{\sqrt{(\mathcal{R} - \delta)^2 + \Omega^2}} \tag{5.4}$$

and we have made the approximation that the number of photons is large (so that the dependence of the Rabi frequency Ω on the photon number can be ignored). The energies of the dressed states are given by:

$$E_{1n} = \hbar(n + \frac{1}{2})\nu + \frac{1}{2}\hbar\mathcal{R} \tag{5.5}$$

$$E_{2n} = \hbar(n + \frac{1}{2})\nu - \frac{1}{2}\hbar\mathcal{R} \tag{5.6}$$

For small detunings, the dressed states contain nearly equal contributions from both atomic states. At zero detuning, there are three transition frequencies between the two doublets, which occur at frequencies ω, and $\omega \pm \Omega$, which is the result observed in the Mollow triplet.

For large detunings, one state in the doublet is more atomic-like, while the other is more field-like. Also, the dressed state energies are not symmetric about the atomic state energies. It is straightforward to calculate that the dressed states are shifted from the original atomic state energy by an amount $\Delta_\pm = \frac{1}{2}(\delta \pm \mathcal{R})$. Figure 35 shows the dressed states for the case where the pump is detuned to lower energy than the transition, with the more atomic-like states shown as darker lines.

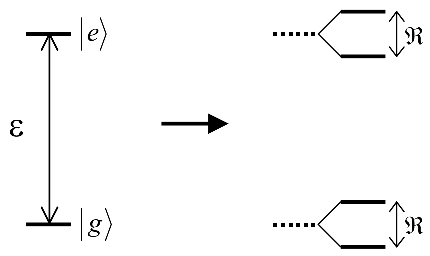

FIGURE 34. Dressed states of atom-field system.

In this case, the strongest absorption occurs at an energy higher than the original transition energy, which indicates the optical Stark shift of the absorption. We shall use this result in Chapter VI to help explain optical Stark shifts in three-level systems.

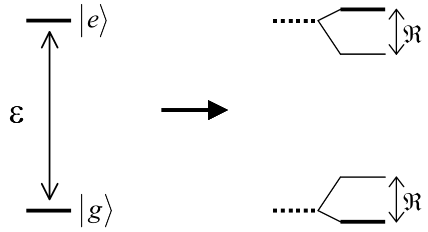

FIGURE 35. Dressed states for $\delta < 0$. The dark lines show the states which have a larger atomic component.

Previous Studies of Rabi Oscillations and Splitting in Semiconductors

The optical Stark effect in semiconductors has received considerable experimental and theoretical treatment in the past [25]. By positioning a 100 fs pump pulse energetically below the exciton transition, high enough electric fields can be generated to shift the exciton peaks to higher energy. Because the pump pulse is far detuned from the absorption, no real excitation is induced in the semiconductor (although virtual excitations are present) and the effect is fully coherent. The lack of a real excitation also makes theoretical modeling considerably easier. Because the Stark shift lasts only as long as the pump pulse, this process can be useful for high speed switching applications.

There have also been theoretical studies which predicted that Rabi oscillations would be possible in semiconductors [46], and a few experiments which indirectly indicated their presence [47, 48]. However, it was only recently that Rabi oscillation of exciton transitions were directly observed in a semiconductor QW system using a pump-probe technique [15]. The primary experimental challenge has been generating pump pulses with a duration long relative to the dipole decoherence time, yet with high enough intensity to induce Rabi oscillations. In the spectral domain, observation of exciton Rabi splitting in QWs has also recently been made [30]. Further observations of Rabi oscillations in QD systems have also been made [49]. These important studies in semiconductors show that the saturation effects due to discrete energy levels in an atomic system have analogous effects in an excitonic system. However, it has also been shown that Coulomb correlations have a strong effect on Rabi oscillations. The observed Rabi oscillations and splitting indicate a Rabi frequency two times that which is calculated from the formula $\Omega = \mu E/\hbar$ [15, 46]. The observed Rabi splitting in Ref. [30] also shows highly asymmetric lineshapes, even with the pump resonant with the exciton transition, a result not expected in atomic systems. Although these results are partially explained by current theories [15, 30], there are still aspects which are not well understood.

Rabi Splitting of Excitons

In this section, we will discuss our own observations of exciton Rabi oscillations and splitting, in an effort to show that we can generate pump fields large enough to achieve EIT. Unless otherwise noted, the experiments were performed using pump pulses of 6 ps duration and probe pulses of 150 fs duration, with the pump and probe having the same circular polarization.

Figure 36 shows the basic result of the Rabi splitting experiments. When the pump is applied to the HH exciton transition, the probe measures a splitting in the absorption spectrum. Although an exact determination of the pump electric field inside the sample is very difficult, an order-of-magnitude calculation using the average pump intensity over the pulse, pump duration, and $\mu/e = 0.6nm$ [15] predicts a Rabi energy $\hbar\Omega \sim 1$ meV. The measured splitting of 1.3 meV taken from our data is consistent with this calculation. Our pump intensities are also comparable to those used in Ref. [30].

We also observed exciton Rabi oscillations by measuring the spectrally integrated differential transmission as a function of the pump-probe delay. Results for these experiments are shown in Fig. 37, for different pump pulse intensities. We first note that after an initial time period of decreased transmission (probably due to induced absorption of biexciton transitions), we observe an increased transmission of the probe pulse due to saturation of the HH exciton transition. At higher pump intensities, we observed up to three highly damped Rabi oscillation cycles. The measured Rabi periods of order 1 ps correspond to Rabi energies of order 1

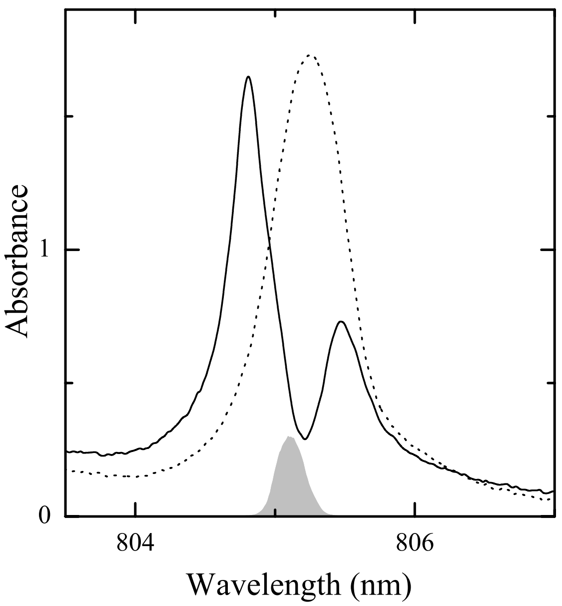

FIGURE 36. Rabi splitting of the HH exciton. The curves show the probe absorption in the presence (solid) and absence (dotted) of a pump with the same circular polarization. The probe arrives 3 ps before the peak of the pump. The pump pulse energy flux is 400 nJ/cm^2, and the pump spectrum is shown as the shaded area. The sample is the 10 nm MQW at 10K.

meV, again in general agreement with the spectral domain measurements. Note that these experiments were performed using a pump pulse of 1.5 ps duration, which was required to obtain electric fields of high enough magnitude to observe three Rabi cycles.

Returning to the Rabi splitting measurements, in Fig. 38 we show that as the pump intensity is increased, the Rabi splitting also increases. It is difficult to predict the expected behavior for the dependence of the Rabi splitting on the pump intensity. Even though the Rabi *frequency* has a definite relationship to the pump electric field ($\mathcal{R} = \sqrt{\delta^2 + \Omega^2}$), this is not necessarily so for the splitting

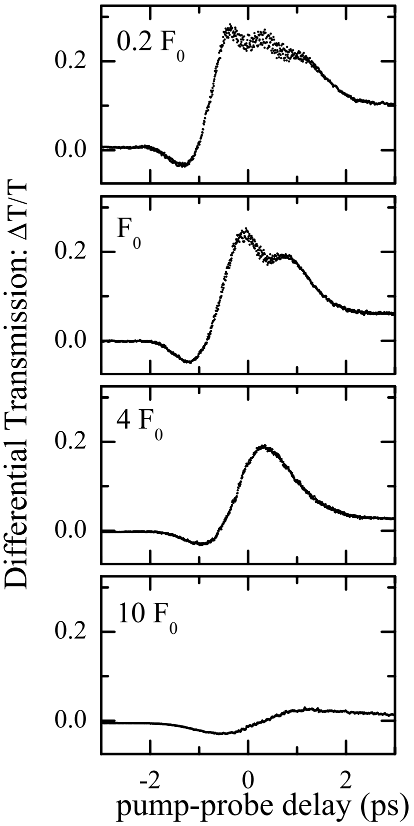

FIGURE 37. Rabi oscillations of HH exciton. The curves show the normalized differential transmission of the 150 fs probe pulse in the presence of a pump pulse resonant with the HH exciton and with 1.5 ps duration. The pump and probe have the same circular polarization. The pump pulse energy flux is indicated in the figure, with F_0 = 600 nJ/cm^2. The sample is the 13 nm MQW at 10K.

observed in the absorption spectrum. From calculations of Mollow spectra for CW excitation in atomic systems [29], we find that the splitting between absorption peaks is not equal to the Rabi frequency. In our transient experiment, we have the further complication that the instantaneous pump intensity is not constant, so that the Rabi frequency changes in time.

Not surprisingly, the observed absorption spectrum is highly dependent on

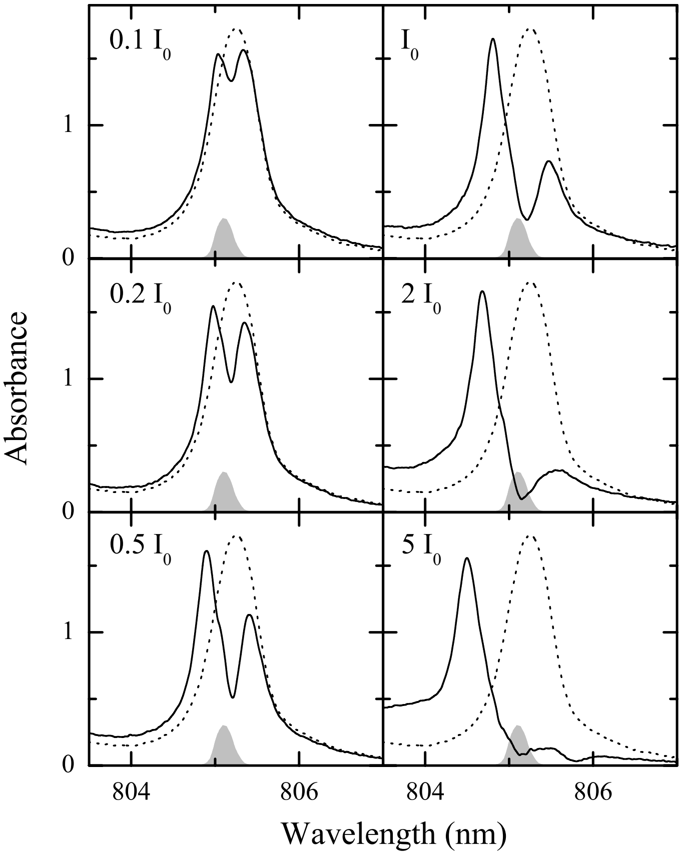

FIGURE 38. Dependence of Rabi splitting on the pump intensity. The pump energy flux is indicated in the figure, with $I_0 = 400 nJ/cm^2$. Other conditions are the same as in Fig. 36.

the pump-probe delay τ, as shown in Fig. 39. The Rabi splitting first appears when the probe arrives well before the peak of the pump, and the splitting initially increases as the delay gets closer to $\tau = 0$. Near $\tau = 0$, however, the splitting becomes harder to resolve and is absent for positive delays. When the probe arrives 8 ps after the pump, the exciton blue shift discussed in Chapter III remains present, along with saturation of the exciton absorption. The observation of stronger Rabi splitting for negative pump-probe delays is consistent with the behavior of the transient EIT experiments in Chapter II where coherent effects are measured.

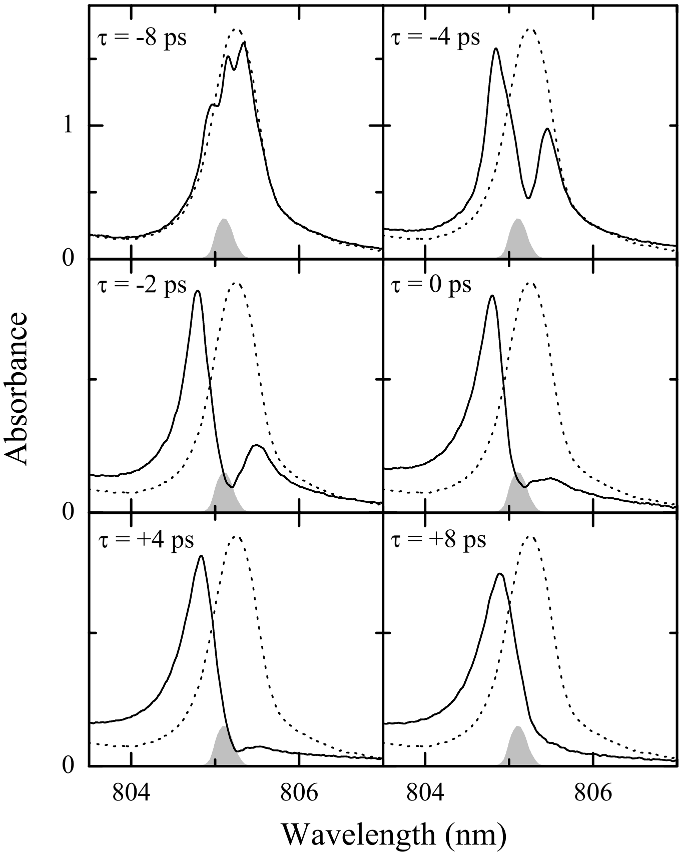

FIGURE 39. Dependence of Rabi splitting on the pump-probe delay τ. Other conditions are the same as in Fig. 36.

The disappearance of the splitting for positive delays also confirms that incoherent spectral hole burning is not an issue. As noted in Chapter III, the exciton linewidth includes some inhomogeneous broadening. A pump with spectral width narrower than the inhomogeneous linewidth could therefore potentially induce spectral hole burning by selectively saturating the absorption over the pump spectrum. However, because the exciton population relaxation times are long (100's of picoseconds) [25], we would expect the effects of spectral hole burning to persist for this duration. The disappearance of the splitting at even short positive pump-probe delays indicates that the origin for the splitting is not spectral hole burning. We can also discount the effects of spectral hole burning because we observe Rabi splittings larger than the original inhomogeneous line width. As discussed in Ref. [29], spectral hole burning is not possible under these conditions. Finally, the large exciton population excited by the pump causes EID, so that during and after the pump pulse, the exciton line is actually homogeneously broadened.

The effects of varying the wavelength of the pump are shown in Fig. 40. We observe very different behaviors when the pump is above the exciton resonance versus when the pump is below. Also, the absorption spectrum is highly asymmetric even when the pump is exactly resonant with the exciton absorption, as shown in Fig. 40(c). The cause of this asymmetry could be traced to several sources. First, the semiconductor system has a natural asymmetry due to the presence of the continuum states at the band edge. The LH exciton resonance is also present on the high energy side of the HH exciton. These effects are always present, however, and would not fully explain the change in asymmetry as a function of the pump-probe delay. Exciton correlations are also important, and furthermore their effects depend on the (changing) exciton density. Although bound biexcitons cannot be excited for this polarization configuration, there may be contributions to the absorption from unbound biexciton states at energies above the HH exciton.

The blue shift of the exciton transition due to exchange interactions has

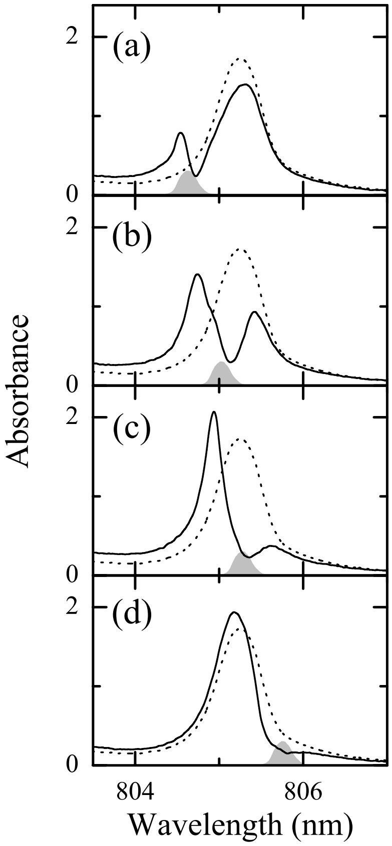

FIGURE 40. Effect of pump wavelength on Rabi splitting. Conditions are the same as for Fig. 36.

a particularly strong effect on the Rabi splitting. Because the exciton transition energy changes according to the exciton density, the effective detuning of the pump also changes *during the pump pulse.* For example, if the pump is initially resonant with the exciton transition, as the pump begins to excite an exciton density, the transition shifts to higher energy. Since the pump is now below the exciton energy, it induces the optical Stark effect, which further shifts the exciton transition to higher energy. On the other hand, if the pump is initially at a higher energy than the transition, the exciton density acts to pull the transition into resonance with the pump. In Fig. 40, the most symmetric Rabi splitting is observed for the pump tuned slightly to the high energy side of the exciton.

For completeness, we note that Rabi splitting of the LH exciton can also be observed. We show this in Fig. 41, for the 17.5 nm MQW sample. Also note that mixed biexciton absorption is visible at energies below the HH exciton, because the pump and probe have the same circular polarization.

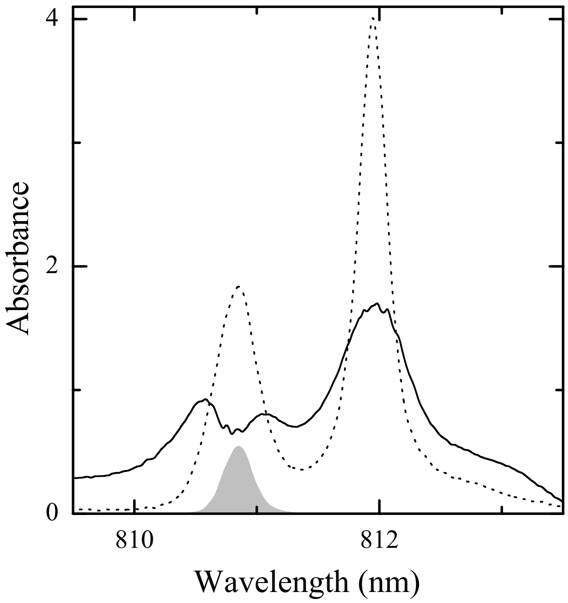

FIGURE 41. Rabi splitting of LH exciton transition. The probe arrives 1 ps before the peak of the pump. The pump pulse energy flux is 400 nJ/cm^2. The sample is the 17.5 nm MQW at 10 K.

Coherent Spectral Oscillations

Previous experimental and theoretical studies in semiconductors have discussed the role of coherent spectral oscillations in transient pump-probe experiments [25]. Spectral oscillations occur for experiments when both the pump and probe pulses are short compared with the dipole decoherence time, and when the probe arrives before the pump. In this case, the differential absorption spectrum contains oscillations having a frequency given by the inverse of the pump-probe delay [50]. The origin of the spectral oscillations can be explained as follows, and is diagrammed schematically in Fig. 42. If the probe arrives before the pump, it excites an optical polarization P in the sample which then begins to decay (as was discussed in Chapter II). The short pump pulse can interrupt this decay at a time $|\tau|$ after its start, through saturation, energy shifts, or other effects induced via its interaction with the system. The pump and probe pulses define a time window of duration τ, leading directly to oscillations at frequency $1/\tau$ in the Fourier transform of the polarization decay (from which the absorption spectrum is derived). The amplitude of the oscillations is also inversely proportional to τ. If the probe arrives too early, the polarization has already decayed to zero by the time the pump arrives, and the pump therefore has no effect.

In our Rabi splitting experiments, we can have spectral oscillations of a different type. The long pump pulse can also act as a time window (though with somewhat smooth edges). This time window can lead to oscillations in the spectrum with a frequency given by the inverse of the time between when the probe arrives at the sample and the time when the pump pulse ends. On the other hand, if the probe arrives much earlier that the pump, a time window is formed between

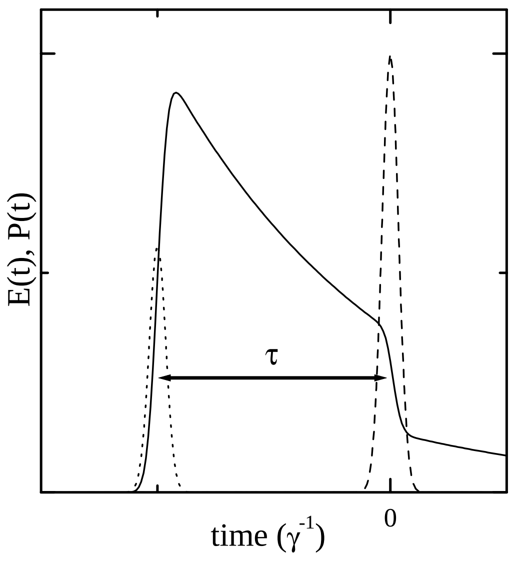

FIGURE 42. Spectral oscillations with short pump pulse. The probe pulse (dotted) excites a polarization P (solid). The decay of P is interrupted by the pump pulse (dashed), which arrives a time τ after the probe.

the time when the probe arrives and the time when the pump pulse *begins.* A diagram of these process is shown in Fig. 43. If the pump duration is long compared with the dipole decay time, then the effects of spectral oscillations can be minimized (though they may still appear for large negative pump-probe delays). The results presented earlier in this chapter satisfy this condition; however, we have also performed experiments using shorter pump pulses of 1.5 ps duration. In Fig. 44, we show the presence of spectral oscillations in a Rabi splitting experiment. Note that because the pump pulses are shorter in this experiment, the peak intensity is higher and larger Rabi splittings are observed.

Spectral oscillations can also have a significant effect in optical Stark effect measurements. In Fig. 45 we show results for when the pump is below the exciton

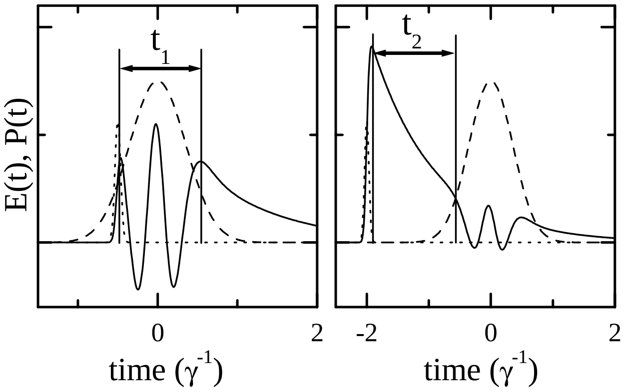

FIGURE 43. Spectral oscillations with long pump pulse. Time windows of duration t_1 and t_2 are formed when the probe arrives during or before the long pump pulse.

resonance. In this case, we see the appearance of a gain region in the spectrum (where the absorbance becomes negative). This gain peak is an artifact of spectral oscillations, and although we eventually learned how to remove it by using longer pump pulses, it has served an important role in our understanding of the physics. In Fig. 46 we plot the Rabi splitting for a resonant pump as a function of the pump-probe delay. A gain peak similar to the one observed when the pump was below resonance also appears after a certain delay when the pump is initially resonant with the HH exciton. This observation confirms what we discussed above: during the pump pulse, the blue shift of the exciton caused by exchange interactions causes the pump to become below resonance.

Even though we have greatly reduced the effects of spectral oscillations by using a long pump pulse, we can completely remove them by performing a slightly different experiment. The spectral oscillations can only occur if the probe pulse is short (and spectrally broad). Therefore, we have also performed experiments

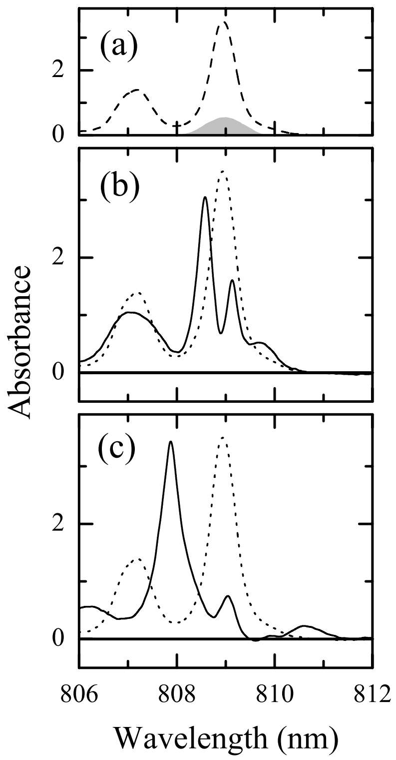

FIGURE 44. Coherent spectral oscillations in Rabi splitting. (a) Absorption spectrum for the 13 nm MQW at 10 K (dashed curve), and the pump spectrum (shaded area). (b) Probe absorption in the absence (dotted) and presence (solid) of pump pulse. The probe arrives 1 ps before the peak of the pump. The pump pulse energy flux is 250 nJ/cm^2. (c) Same as b, but with a pump pulse energy flux of 1.3 μJ/cm^2.

by using a pulse shaper to reduce the spectral width of the probe pulse. The pulse shaper was also used to scan the center wavelength of the probe in order to obtain an absorption spectrum. In this case, because the separation of the probe spectral components was performed before interaction with the sample, a spectrometer was not required for detection and a photodiode was used instead. For these experiments, the probe duration was 8 ps, while the pump duration was

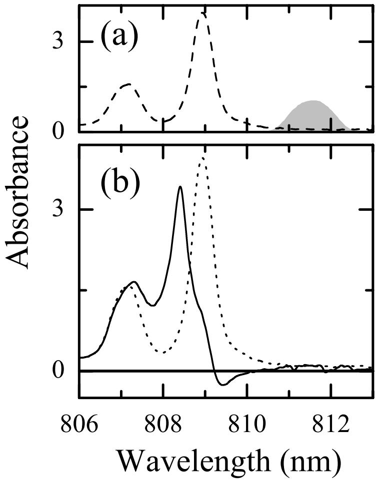

FIGURE 45. Coherent gain due to spectral oscillations in the optical Stark effect. (a) Absorption spectrum for the 13 nm MQW at 10 K (dashed curve), and the pump spectrum (shaded area). (b) Probe absorption in the absence (dotted) and presence (solid) of pump pulse. The probe arrives at the peak of the pump. The pump pulse energy flux is 2.5 μJ/cm^2.

6 ps. In Fig. 47 we show that Rabi splitting occurs in the spectrum for these excitation conditions. The downside to performing experiments in this manner was that the spectral resolution was given by the spectral width of the probe, which was limited to 0.17 nm due to the pulse shaper (in comparison to 0.05 nm resolution with the spectrometer). Because we can eliminate the effects of spectral oscillation in the short probe experiments by using a long pump pulse, performing the experiments using a long probe offers no advantages to us.

Theoretical Modeling of Exciton Rabi Splitting

We have also performed theoretical modeling of Rabi splitting in semiconductors to understand the physics of the experiment better. The model is based on

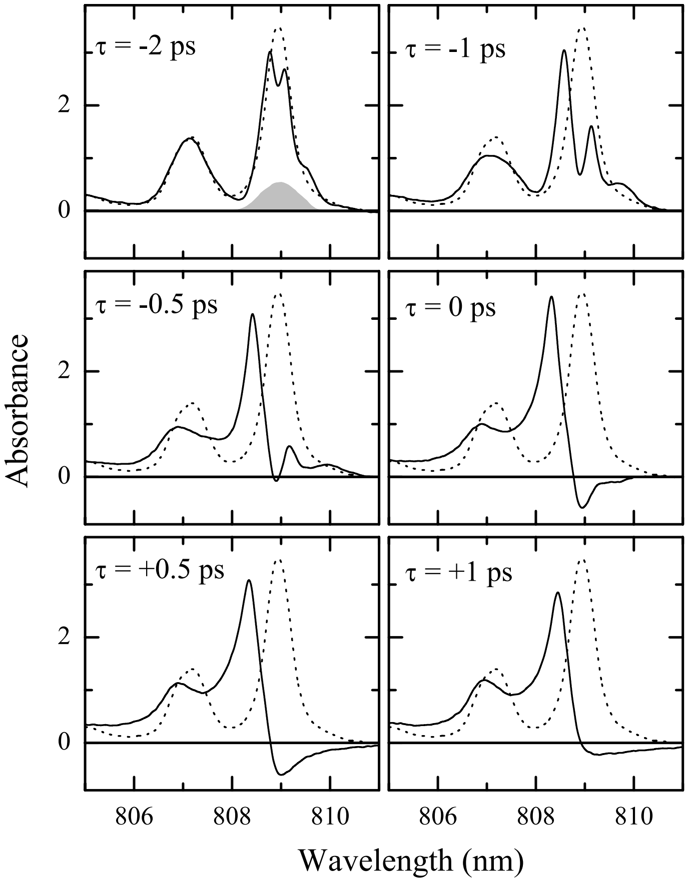

FIGURE 46. Coherent gain due to spectral oscillations in Rabi splitting. The pump-probe delay is indicated in the figure. The pump pulse energy flux is 250 nJ/cm^2. The pump spectrum is the same as in Fig. 44.

the OBE for a two-level system interacting with two optical fields: a strong pump field and a weak probe field. The derivation of the OBE for this system is given in Ref. [29] for CW excitation; we will derive the OBE but solve them numerically using pulsed pump and probe fields.

We consider a two level system with with ground state $|g\rangle$ and excited state $|e\rangle$ separated in energy by $\hbar\omega$. We use the OBE for a two-level system with

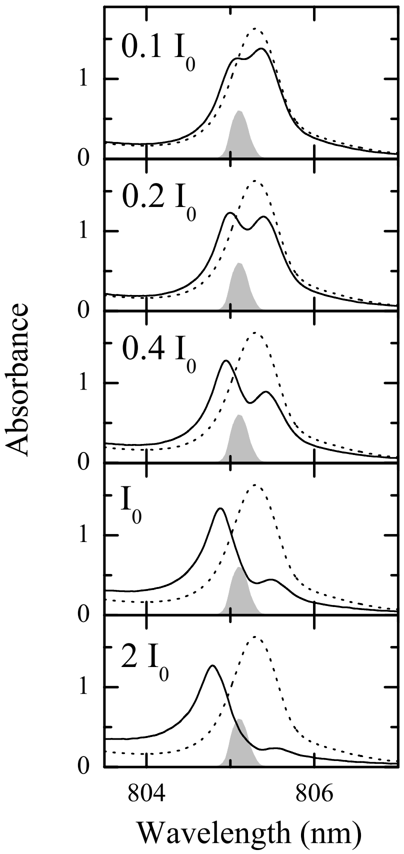

FIGURE 47. Rabi splitting experiment using a temporally long probe pulse. The peaks of the pump and probe arrive at the same time. The pump pulse energy flux is indicated in the figure, with $I_0 = 400$ nJ/cm^2. The sample is the 10 nm MQW at 10K.

phenomenological many-body corrections.

$$\dot{\rho}_{eg} = -\left(i\omega + \gamma + \sigma\rho_{ee}\right)\rho_{eg} - \frac{i\mu}{\hbar}\mathcal{E}\left(2\rho_{ee} - 1\right) \tag{5.7}$$

$$\dot{\rho}_{ee} = -\Gamma\rho_{ee} - \frac{i\mu}{\hbar}\left(\mathcal{E}\rho_{eg} - c.c.\right) \tag{5.8}$$

where we have assumed that $\rho_{ee} + \rho_{gg} = 1$. In these equations γ is the polarization dephasing rate, Γ is the population decay rate of state $|e\rangle$ and μ is the dipole matrix element (assumed to be real). We also include the effects of excitation induced dephasing (EID) by taking $\gamma \rightarrow \gamma + \sigma\rho_{ee}$.

The electric field interacting with this system consists of a pump (saturator) field and a probe field.

$$\mathcal{E} = \mathcal{E}_s + \mathcal{E}_p = \frac{1}{2}\left[E_s(t)e^{i(k_s \cdot r - \nu_s t)} + E_p(t)e^{i(k_p \cdot r - \nu_p t)} + c.c.\right] + L\mu\left(\rho_{eg} + c.c.\right) \quad (5.9)$$

which includes the Lorentz local field corrections in the factor L. In the final equations, it is more useful to express the Lorentz factor $\eta = \frac{2\mu^2 L}{\hbar}$.

To solve these equations, we follow the procedure given in Ref. [29], keeping terms up to first order in the probe field, but to all orders in the pump field. The details of the calculation are given in Appendix. A. The set of five coupled differential equations that we obtain are solved numerically using Mathematica, using the same methods as described in Chapter II.

We first consider solutions without the many-body effects included ($\sigma = \eta = 0$). Figure 48 shows Rabi splitting in the probe absorption spectrum for various saturator Rabi frequencies. The Rabi splitting increases for increasing saturator intensity, as expected. For comparison, in Fig. 48(b), we show results from analytic solutions of the OBE using CW saturator and probe fields, but with other conditions the same as for the transient results in Fig. 48(a). A particular benefit of the transient experiment is that the effects of high pump fields can be explored at relatively low excitation densities by using negative pump-probe delays. In contrast, the CW measurements are dominated by saturation effects, while the coherent Rabi splitting effects are small in magnitude. Note the change in scale for the y-axes in Fig. 48(b).

Returning to the numerical calculations, the effects of changing the pump-probe delay are shown in Fig. 49. As was observed in the experimental data, the Rabi splitting is best resolved for negative pump-probe delays. This behavior is also consistent with the EIT calculations discussed in Chapter II, and is a property of the pulsed experiment.

To model many-body interactions, we can examine the effects of EID and local fields on the solutions. We first consider the many-body effects in the incoherent limit $\tau = 20\gamma^{-1}$. Figure 50 shows that EID and the local field effects lead to a broadening and energy shift of the absorption resonance which increase with the exciton density. When both effects are included into the coherent regime of Rabi splitting, the experimental results can be qualitatively reproduced, as shown in Fig. 51. The model shows that the exciton blue shift during the pump pulse leads to an asymmetric lineshape, because the pump becomes detuned.

We should note that the model seems to qualitatively reproduce the experimental results for the regime $\Omega_s < \gamma$, but does not work as well for higher Rabi frequencies. This is not too surprising, because correlation effects which are not included in our simple model become important at higher exciton densities. Nevertheless, our model based on the OBE is useful for showing how the Rabi splitting spectrum is affected by the energy shift of the exciton resonance.

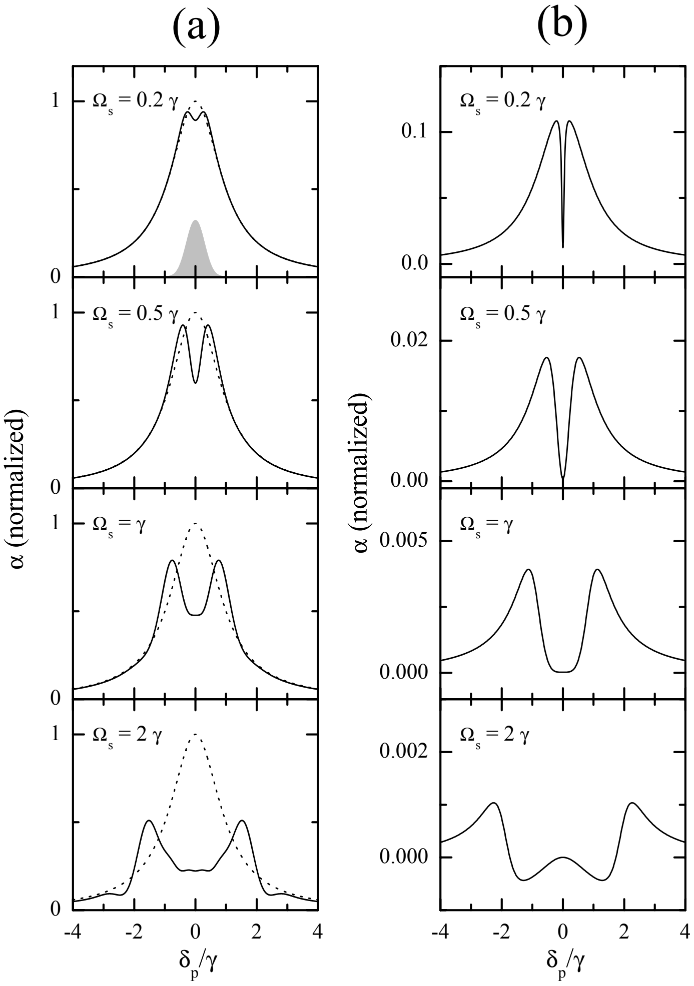

FIGURE 48. Rabi splitting in calculated absorption spectra. Solid curves show the probe absorption as a function of the probe detuning δ_p. (a) Absorption spectra from numerical calculation using pulsed saturator and probe. The saturator peak Rabi frequencies are given in the figure. The probe and saturator pulse shapes are Gaussian with durations of $0.1\gamma^{-1}$ and $10\gamma^{-1}$, respectively. The probe arrives $5\gamma^{-1}$ before the peak of the pump. The pump spectrum is shown as the shaded area in the figure. (b) Absorption spectra analytically calculated for CW saturator and probe. Note the change in scale for the y-axes. The saturator Rabi frequencies are given in the figure. In both (a) and (b), $\Gamma = 0.005\gamma$, and $\eta = \sigma = 0$.

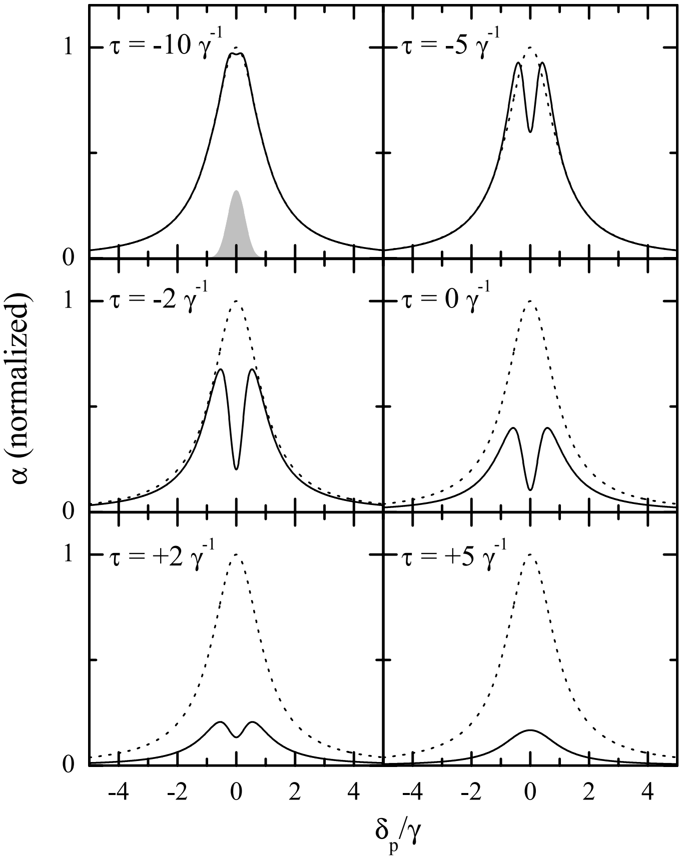

FIGURE 49. Effects of the pump-probe delay on Rabi splitting in numerically calculated absorption spectra. The saturator peak Rabi frequency is 0.5γ. The probe and saturator pulse shapes are Gaussian with durations of $0.1\gamma^{-1}$ and $10\gamma^{-1}$, respectively. The pump-probe delay is indicated in the figure. Other parameters are $\Gamma = 0.005\gamma$, and $\eta = \sigma = 0$.

Summary and Relationship to EIT

The experimental results presented in this chapter are useful for understanding Rabi splitting and the optical Stark effect in semiconductors. Rabi splitting is strongly affected by the many-body interactions which lead to the exciton blue shift, leading to highly asymmetric spectra. The experiments also prove that

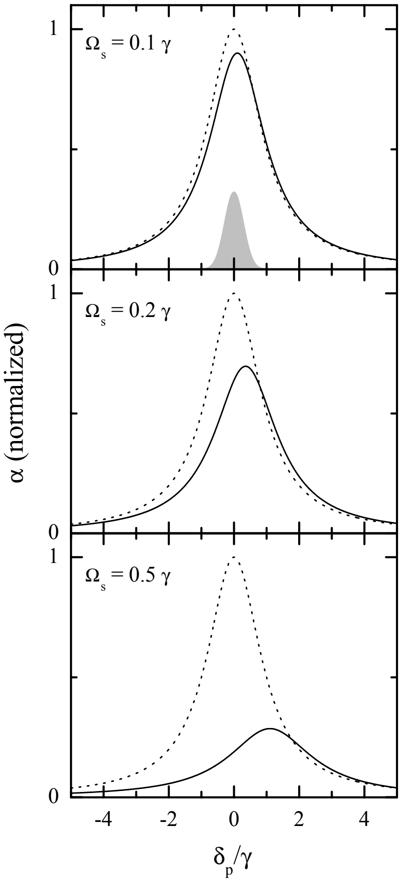

FIGURE 50. Incoherent effects of EID and local fields. Parameters are the same as in Fig. 49, but with $\tau = +20$ and with the pump Rabi frequencies shown in the figure. EID is included, with $\sigma n_{sat} = 2\gamma$ and local field effects are included, with $\eta n_{sat} = 4\gamma$, where the saturation density n_{sat} has been normalized to one.

pump-probe spectroscopy with a long pump pulse and short probe pulse can be a valuable technique for studying coherent optical phenomena. By observing Rabi splitting, we have shown that our experimental setup is capable of producing the correct conditions for also observing EIT. The remaining chapters will be devoted to the study of EIT in various three-level semiconductor systems.

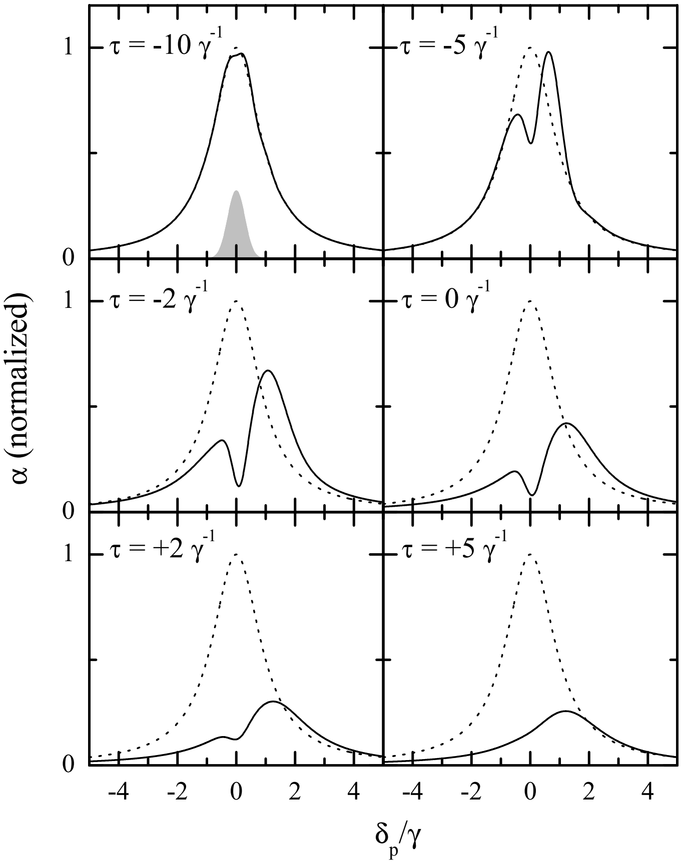

FIGURE 51. Effect on Rabi splitting of many-body effects due to EID and local fields. The pump-probe delays are shown in the figure, and other parameters are the same as in Fig. 50.

CHAPTER VI

EIT VIA VALENCE BAND COHERENCE

The possibility of creating dark states in semiconductors, which could form the basis for EIT, was proposed in 1995 by Lindberg and Binder [20]. Using the semiconductor Bloch equations, they showed that despite the many-body nature of a semiconductor system, it should be possible to induce a nonradiative coherence using exciton states. The presence of such a nonradiative coherence was shown to have similar theoretical effects on the optical properties of the semiconductor and atomic systems. As shown by the diagram in Fig. 52(a), HH and LH transitions excited by opposite circular polarizations have different valence band states, but a common conduction band state. A nonradiative coherence between HH and LH valence band states was shown to be a possible basis for forming dark states and establishing EIT.

From the level diagram, it would appear that the three electron states form a Λ-type three-level system in which the valence band states are coupled by a two-photon transition. However, in this semiconductor system, both valence band states are initially occupied, which does not match the prototypical atomic EIT setup for a Λ system. To make an analogy to an atomic system, the system is more correctly described as a V system as shown by the exciton states in Fig. 52(b). In this picture, the exciton ground state $|0\rangle$, the HH exciton excited with σ^+ light $|HH+\rangle$, and the LH exciton excited with σ^- light $|LH-\rangle$ all include a contribution from the common conduction band state. In the exciton state basis, the nonradiative coherence between exciton states is still due to the different valence band states involved.

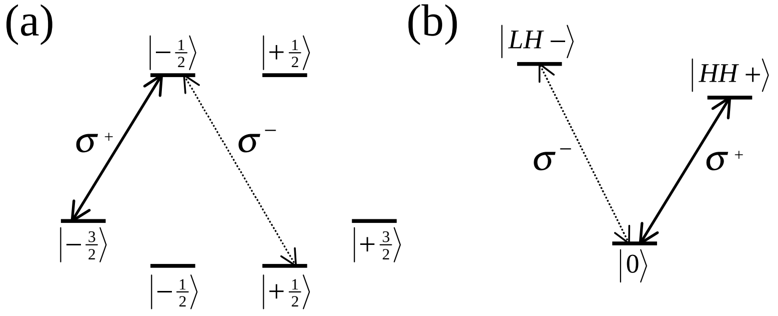

FIGURE 52. Energy diagrams for EIT via HH-LH valence band coherence. (a) Electron states. (b) Exciton states

Coupled Optical Stark Shifts of HH and LH Excitons

Experimental verification that the HH and LH excitonic transitions with opposite circular polarization are coupled was shown in Ref. [19], using the optical Stark effect. We have already discussed the optical Stark effect of the HH exciton in Chapter V, but here we consider the so-called coupled optical Stark effect. By applying a strong pump with σ^+ polarization below the HH exciton transition, the HH absorption probed with the same polarization is shifted to higher energy, as discussed in Chapter V. The experiments in Ref. [19] showed that the LH transition with opposite polarization also shifted to higher energy. While the results in Ref. [19] do show that the HH and LH transitions are coupled, and thus provide direct evidence for a valence band coherence, the experiments were performed at relatively large pump detunings and the theory performed in the

$\chi^{(3)}$-limit, outside the regime where EIT could occur if the pump were resonant with the HH transition.

To show that the Stark shifts of the HH and LH excitons behave similarly under conditions approaching those for the observation of EIT, and that the non-radiative valence band coherence also survives under these conditions, we present experimental results for a nearly resonant pump with relatively high intensity. The results here were obtained using the 17.5 nm MQW sample, with the pump tuned 1.0 nm to the red side of the HH exciton absorption. The pump duration was 6 ps, while the probe duration was 150 fs. The probe arrived 1 ps before the peak of the pump.

In Fig. 53, we show the absorption spectrum for a probe pulse with the same ($\sigma^+\sigma^+$) and the opposite ($\sigma^+\sigma^-$) circular polarization as the pump. For the $\sigma^+\sigma^+$ case, a strong blue shift of the HH exciton is observed, while the LH exciton shows no shift (or even a slight red shift). For the $\sigma^+\sigma^-$ case, the LH exciton shows the expected blue shift. Note that the HH exciton shows a strong red shift for $\sigma^+\sigma^-$, which has been discussed in the literature [51, 52], and is due to Coulomb correlations. Even for this strong pumping case, where the optical Stark shifts are of the same magnitude as the exciton linewidths, the coupling between the HH and LH bands persists. In Fig. 54, we show the magnitude of both the HH and LH exciton blue shifts as a function of the pump intensity, taken under conditions similar to Fig. 53. In Fig. 54, we also show the ratio of the HH and LH blue shifts, which within the experimental uncertainty equals 2 in all cases but the highest intensity pump. It is likely that at the highest intensity, a real excitonic population is excited by the pump, which may introduce other correlation effects.

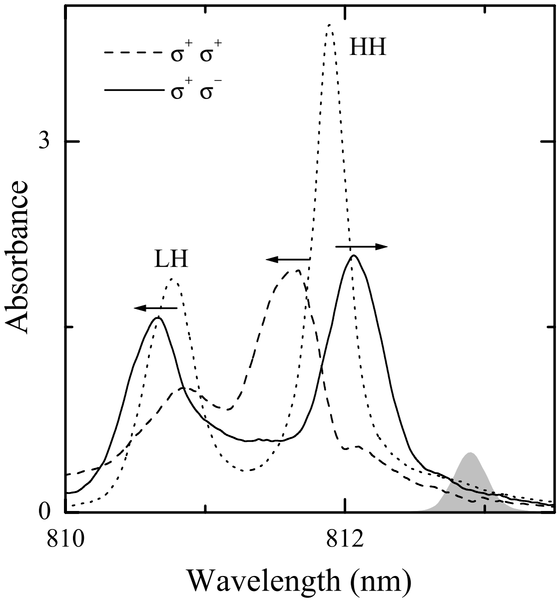

FIGURE 53. Coupled optical Stark shifts of HH and LH excitons. The dashed line is the probe absorption for $\sigma^+\sigma^+$ polarizations, the solid line is for $\sigma^+\sigma^-$ polarizations, and the dotted line shows the linear absorption in the absence of the pump. The pump spectrum is shown as the shaded area, and the pump pulse energy flux is 3.2 μ J/cm^2.

The value of 2 for the ratio of the energy shifts can be understood by considering the dressed states of the system. As shown in Fig. 55, the strong pump applied to the HH transition dresses both the $|0\rangle$ and $|HH+\rangle$ states. With the pump at a lower energy than the transition, the strongest absorption comes from the states marked by darker lines in the figure (these states have a larger atomic contribution to their wavefunction relative to the field contribution). A probe of the HH+ transition shows a blue shift in absorption due to the shift in energy of both $|0\rangle$ and $|HH+\rangle$ states. A probe of the LH- transition also shows a blue shift, but only from the shift of the $|0\rangle$ state. Therefore, the observed energy shift

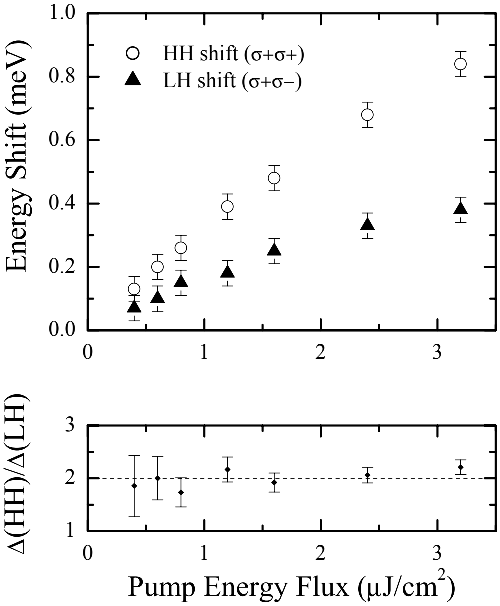

FIGURE 54. Exciton optical Stark shifts as a function of pump intensity. Energy shifts relative to the linear absorption peaks were measured from absorption spectra similar to Fig. 53. Open circles show the shift of the HH exciton for $\sigma^+\sigma^+$ polarizations of the pump and probe, and filled triangles show the shift of the LH exciton for $\sigma^+\sigma^-$ polarizations. The ratio of the HH shift to the LH shift is also shown.

of the LH- transition is half the shift for the HH+ transition. The fact that this description of light interacting with excitons in the semiconductor system agrees so well with predictions based on light interacting with electrons in an atomic system suggests that we should also be able to observe EIT in this system.

We have shown that the nonradiative coherence between valence bands exists and that an analogy with an atomic three-level system is appropriate. Coupled with the previously discussed experiments showing Rabi splitting of the HH exciton, we can deduce that it should be possible to observe EIT in this system, even for the worst case scenario where the decoherence rate of the valence band

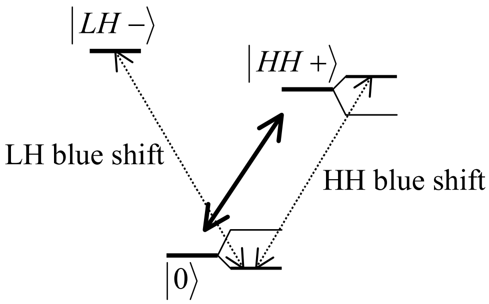

FIGURE 55. Dressed states of the HH transition with σ^+ pump field below resonance. The LH- blue shift is half that of the HH+ blue shift.

coherence is the same magnitude as the dipole coherences. In this case, by tuning the σ^+ pump resonant with the HH transition, we would expect to see an EIT dip in the LH absorption for a σ^- probe.

EIT via HH-LH Valence Band Coherence

Based on the discussion so far, all the necessary pieces required to observe EIT in this system are present; however, the actual experimental verification has been missing until now, though not for lack of effort. As noted in Chapter II, a CW pump is not the best choice for observation of EIT in semiconductors, but neither is a 150 fs pulse typical of other semiconductor experiments. As we discovered in the Rabi splitting experiments, it is important to make the pump pulse duration long relative to the decoherence times, in order to maximize the duration of the coherent interaction between the pump and the system. A pump pulse that is too short therefore effectively prevents the observation of EIT. Also, based on the analysis of the atomic system, it would seem that EIT would best be resolved using the highest pump intensity possible. However, we will show that this is not the case for this semiconductor system, which certainly delayed our successful observation of EIT. Finally, although high quality samples showing narrow exciton linewidths are desirable, the single QWs we initially used did not have enough absorption to resolve EIT signatures. The increased absorption in the MQW samples we used more than made up for their slightly broader linewidths.

In Fig. 56 we show results for pumping at the HH exciton and probing with opposite circular polarization. We will discuss the strong dip at the HH resonance in the next chapter, but of interest here is the dip in the LH absorption. The presence of this absorption dip verifies that EIT is occurring due to the valence band coherence. Slightly better results were obtained using the 13 nm MQW, for which we show results in Fig. 57 and for the rest of this chapter.

Even though we know from the Rabi splitting experiments that spectral hole burning is not an issue for the pump intensities used in these experiments, it is nevertheless important to verify that the dependence of the EIT dip on the pump-probe delay acts as expected. Figure 58 shows the absorption spectrum for six values of the pump-probe delay. The EIT dip in the LH exciton is best resolved for pump-probe delays near zero, and disappears for delays greater than 4 ps. This behavior is consistent with a coherent effect such as EIT, and again rules out spectral hole burning as a possible explanation for the results.

To underscore the dependence of the EIT dip on the underlying valence band coherence, we show in Fig. 59 the result of changing the pump excitation wavelength. As the pump is tuned relative to the HH exciton peak, the EIT dip moves in the same direction relative to the LH peak. As discussed in Chapters II

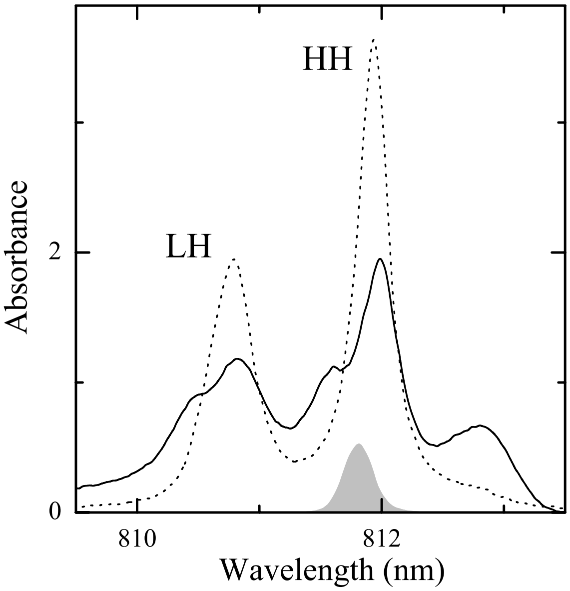

FIGURE 56. EIT due to HH-LH valence band coherence in the 17.5 nm MQW sample. The solid line is the absorption of the probe for $\sigma^+\sigma^-$ polarization, and the dotted line is the linear absorption. The pump spectrum is shown as the shaded area, and the pump pulse energy flux is 200 nJ/cm^2.

and V, this behavior reflects the two-photon resonance condition in a Λ or V system. The results also demonstrate a difference of the semiconductor system from an ideal atomic system. In Fig. 59, the EIT dip is only resolved if the pump is on the high energy side of the HH resonance. Because the pump is resonant or nearly resonant with the HH exciton absorption, and therefore excites a large population of excitons, the exchange interactions cause a blue shift of both the HH and LH absorption peaks, as discussed in Chapter III. In order for the EIT dip to be centered on the shifted LH peak, the pump must be tuned to the high energy side of the HH peak. In contrast, if the pump is tuned to the low energy side of the HH, the two-photon resonance condition for the EIT places it

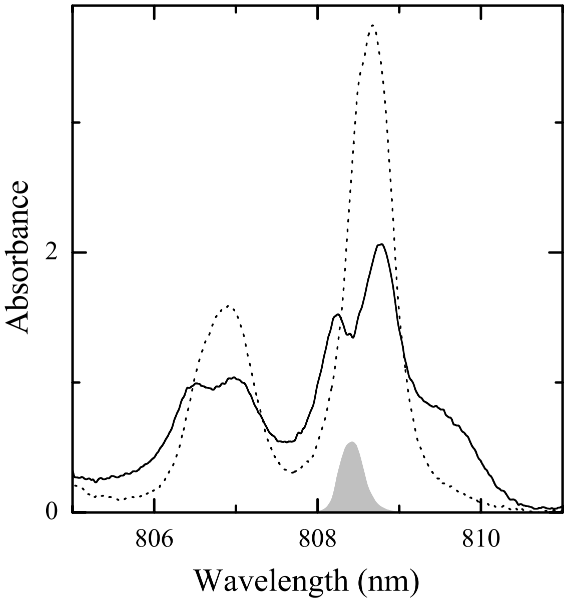

FIGURE 57. EIT due to HH-LH valence band coherence in the 13 nm MQW sample. The pump pulse energy flux is 160 nJ/cm^2.

in a position of low absorption on the shifted exciton peaks, where it cannot be resolved. Note, however, that although the many-body interactions cause energy shifts of the exciton absorption, the coherent optical interactions caused by the nonradiative coherence remain similar to those in an atomic system.

The effects of changing the pump intensity are shown in Fig. 60. Although the depth of the EIT dip increases somewhat, the dip is also broadened significantly as the pump intensity is increased. There are two effects occurring here. First is the overall reduction in LH absorption, which is expected for a V system due to incoherent pumping from the $|0\rangle$ state to the $|HH+\rangle$ state. To show this effect, we again use our numerical solutions for the OBE, but this time must use the equations for a V system. For the V system, we must keep track of the density

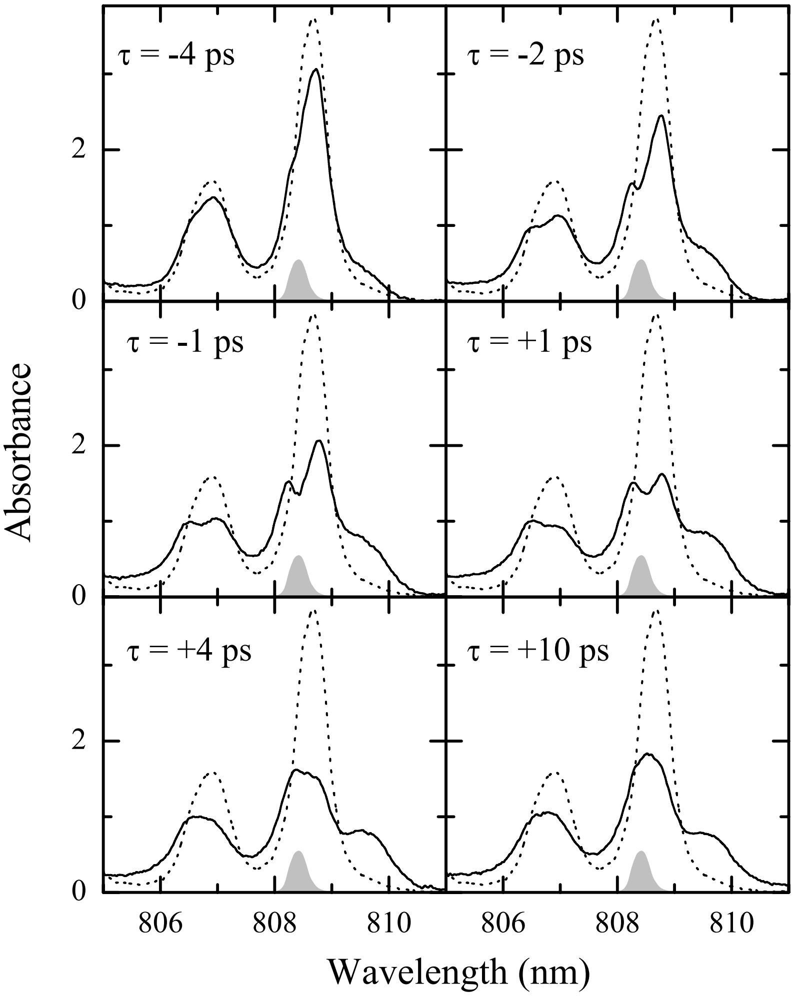

FIGURE 58. Dependence of the probe absorption spectrum on the pump-probe delay. The pump pulse energy flux is 160 nJ/cm^2.

matrix elements excited by the pump even when the probe is absent. The OBE to first order in the probe field are:

$$\dot{\tilde{p}}_{HH}^{(0)} = \left(i\delta_{HH} - \gamma\right)\tilde{p}_{HH}^{(0)} - \frac{i\Omega_{pump}}{2}\left(2n_{HH}^{(0)} - 1\right) \tag{6.1}$$

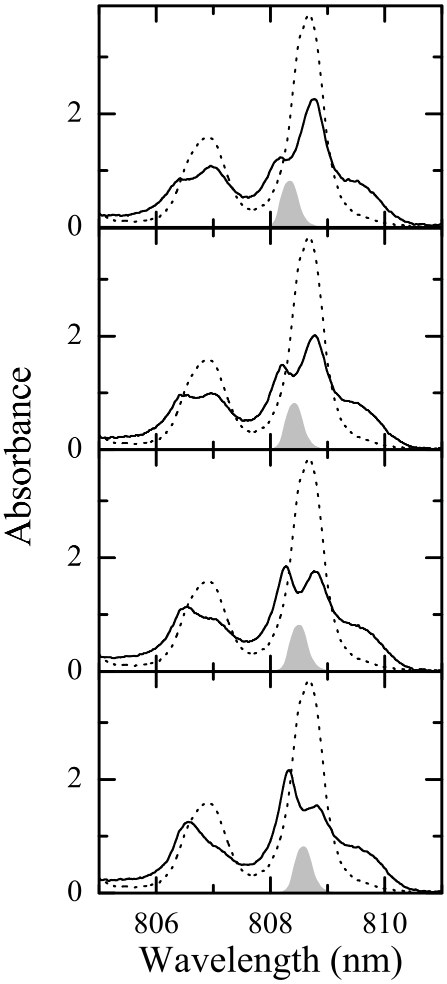

FIGURE 59. Dependence of the probe absorption spectrum on the pump wavelength. The pump pulse energy flux is 160 nJ/cm^2.

$$\dot{n}_{HH}^{(0)} = -\Gamma n_{HH}^{(0)} - \frac{i}{2}\left(\Omega_{pump}^{*}\tilde{p}_{HH}^{(0)} - c.c\right) \tag{6.2}$$

$$\dot{\tilde{p}}_{LH}^{(1)} = \left(i\delta_{probe} - \gamma\right)\tilde{p}_{LH}^{(1)} - \frac{i\Omega_{probe}}{2}\left(n_{HH}^{(0)} - 1\right) - \frac{i\Omega_{pump}}{2}\tilde{p}_{v}^{(1)*} \tag{6.3}$$

$$\dot{\tilde{p}}_v^{(1)} = \left[i\left(\delta_{pump} - \delta_{probe}\right) - \gamma_v\right]\tilde{p}_v^{(1)} - \frac{i\Omega_{probe}^*}{2}\tilde{p}_{HH}^{(0)} + \frac{i\Omega_{pump}}{2}\tilde{p}_{LH}^{(1)*} \tag{6.4}$$

where we have replaced the labels a and b with HH and LH, and used $\tilde{p}_v^{(1)}$ and γ_v to label the nonradiative valence band coherence and its decoherence rate, respectively. Details of the derivation are given in Appendix B

The decrease in population in the ground state $|0\rangle$ caused by the pump leads to a decrease in absorption for the $|0\rangle \leftrightarrow |LH-\rangle$ transition, even in the absence of EIT. This is shown on the left hand side of Fig. 61, in which we plot absorption spectra for numerical solutions of the OBE similar to those in Chapter II, but this time for a V system. The solid curves show the solution for three-level system, with $\gamma_v = 0.2\gamma$, where γ and γ_v are the decoherence rates for the dipole and valence band coherence, respectively. As the pump intensity increases from Fig. 61(a) to (c), the EIT dip gets deeper. In addition to the coherent effects directly related to the presence of the nonradiative coherence, the overall absorption strength is reduced. The dashed lines show this incoherent contribution to the absorption, calculated in the limit of $\gamma_v >> \gamma$.

In the experimental data shown in Fig. 60, these incoherent pumping effects are evident in the overall reduction in absorption of both the HH and LH exciton resonances. The incoherent nature of this absorption reduction is confirmed by by the delay dependence in Fig. 58, where the HH and LH absorption is reduced even when the probe arrives 10 ps after the pump. However, this reduction in absorption does not explain why the EIT dip in Fig. 60 does not significantly increase in depth with increasing pump intensity, as the numerical results would suggest.

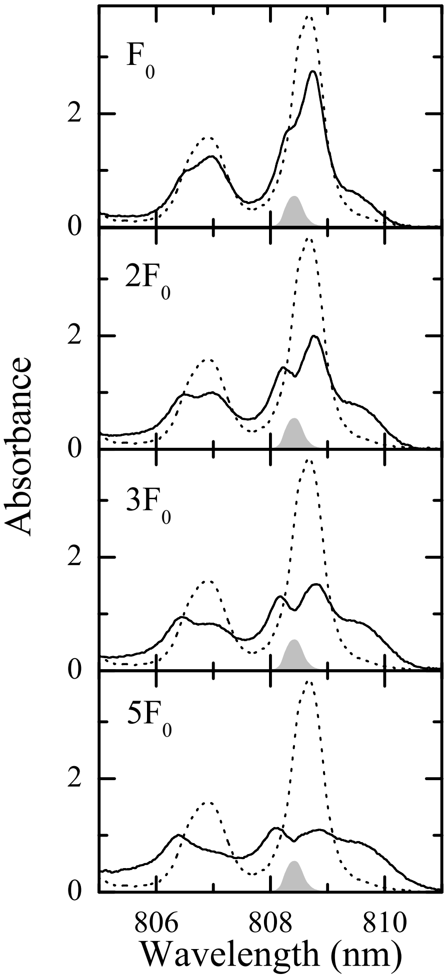

FIGURE 60. Dependence of the probe absorption spectrum on the pump intensity. The pump pulse energy flux is indicated in the figure, with $F_0 = 80$ nJ/cm^2.

The second effect of incoherent pumping of HH excitons is an increase in exciton-exciton scattering, which leads to an increase in all decoherence rates, including both γ and γ_v. The effects of such EID have already been discussed in Chapter V, and they are certainly applicable here. To model the effects of EID, we have added phenomenological corrections to the OBE in which the decoherence

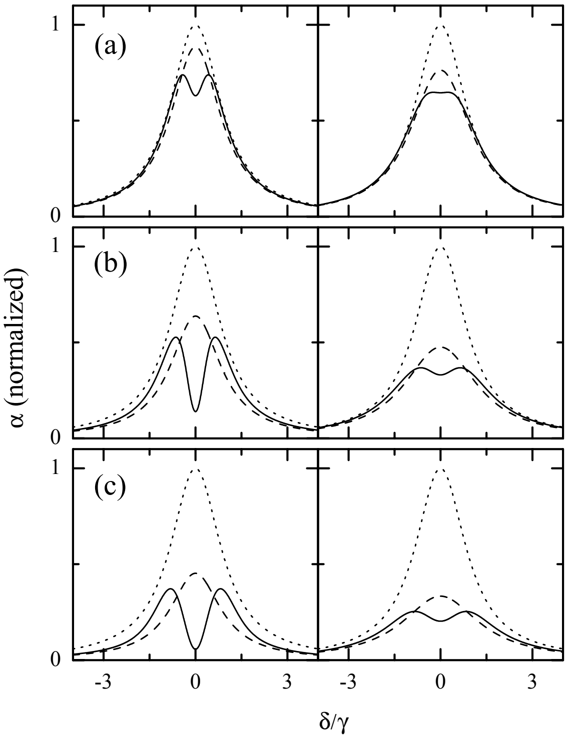

FIGURE 61. Probe absorption spectra determined from numerical solution of the OBE for a V system. The solid curves are for $\gamma_v = 0.2\gamma^{-1}$, and the dashed curves are for $\gamma_v >> \gamma$. The dotted curves show the linear absorption of the probe in the absence of the pump. The left hand column shows results without EID, while the right hand column shows results with $\sigma n_{sat} = \gamma$. The pump and probe have durations $5\gamma^{-1}$ and $.05\gamma^{-1}$, respectively. The probe arrives $2\gamma^{-1}$ before the peak of the pump. The peak pump Rabi frequency is 0.5γ for (a), γ for (b), and 1.5γ for (c).

rates are dependent on the population in the $|HH+\rangle$ state (note that to first order in the probe field, the population in the $|LH-\rangle$ state is zero). The modified equations are as follows:

$$\dot{\tilde{p}}_{HH}^{(0)} = \left(i\delta_{HH} - \gamma - \sigma n_{HH}^{(0)}\right)\tilde{p}_{HH}^{(0)} - \frac{i\Omega_{pump}}{2}\left(2n_{HH}^{(0)} - 1\right) \tag{6.5}$$

$$\dot{n}^{(0)}_{HH} = -\Gamma n^{(0)}_{HH} - \frac{i}{2}\left(\Omega^{*}_{pump}\tilde{p}^{(0)}_{HH} - c.c\right) \tag{6.6}$$

$$\dot{\tilde{p}}^{(1)}_{LH} = \left(i\delta_{probe} - \gamma - \sigma n^{(0)}_{HH}\right)\tilde{p}^{(1)}_{LH} - \frac{i\Omega_{probe}}{2}\left(n^{(0)}_{HH} - 1\right) - \frac{i\Omega_{pump}}{2}\tilde{p}^{(1)*}_{v} \tag{6.7}$$

$$\dot{\tilde{p}}^{(1)}_{v} = \left[i\left(\delta_{pump} - \delta_{probe}\right) - \gamma_v - \sigma n^{(0)}_{HH}\right]\tilde{p}^{(1)}_{v} - \frac{i\Omega^{*}_{probe}}{2}\tilde{p}^{(0)}_{HH} + \frac{i\Omega_{pump}}{2}\tilde{p}^{(1)*}_{LH} \tag{6.8}$$

where $\sigma n^{(0)}_{HH}$ models the EID. In the right hand column of Fig. 61, we show results for the same parameters as in the left column, but including the EID terms. In this case, the incoherent contribution to the absorption broadens due to EID, as shown by the dashed lines. In addition, the EIT dip broadens significantly for all pump intensities shown, as shown by the solid lines.

Although the experimental results show that EIT is possible due to the valence band coherence, the weak EIT signature is somewhat disappointing. The cause for such a weak EIT signal stems directly from the decoherence of the valence band coherence. From the experimental data, it is unclear whether the decoherence rate of the valence band coherence is too high even at low excitation levels, or if exciton-exciton scattering is the primary limitation. As discussed in Chapter III, the HH and LH valence bands undergo mixing away from the Brillouin zone center. This band mixing contributes to rapid spin relaxation within the valence bands [53], which may be a factor in the decoherence of the valence band coherence, even at low excitation levels. Regardless of the low excitation limit for γ_v, the presence of strong exciton-exciton scattering is clearly visible as the pump intensity is increased.

In this chapter, we have shown experimental evidence for EIT in a semiconductor due to a coherence between HH and LH valence bands. While optical Stark effect measurements had previously indicated the presence of the valence band coherence, a direct use of this nonradiative coherence to induce EIT was lacking. Even though the experiments were successful, the large decoherence rate of the valence band coherence prevents stronger EIT signatures from being observed. It is clear that a V configuration is not the ideal system for observing EIT in semiconductors, due to the effects of exciton-exciton scattering. A Λ or *cascade* system, in which excitation of a real population by the pump could be prevented, would be much more promising for observing large EIT signatures. Unfortunately, looking at the state diagram, there are no other three-level systems available. We will show in the following chapters how the exciton-exciton interactions which are so detrimental here actually hold the solution to the problem of observing stronger EIT effects in semiconductors.

CHAPTER VII

EIT VIA EXCITON SPIN COHERENCE

With only marginal success of EIT based on the coherence between HH and LH valence bands, and having thus exhausted the only three-level system indicated by the band diagram, we are left with no clear direction for how to proceed toward our goal of observing strong EIT signatures in semiconductors. Because we are taking an effect which was discovered in atomic systems, and trying to extend the studies to semiconductor systems, it is easy to push the analogies between excitons and atoms too far. We must not forget, however, that excitons are not atoms. Although exciton-exciton interactions may appear at times to be a hindrance (causing strong dephasing in experiments and generally complicating theoretical analysis), we will show in this chapter that by exploiting these interactions inherent to a many-body semiconductor system, we can induce EIT in ways not possible in atomic systems.

We begin with an interesting observation encountered during our investigations of Rabi splitting discussed in Chapter V, and also when exploring the valence band coherence in Chapter VI. In the Rabi splitting experiments, we used co-circularly polarized pump and probe pulses acting on the same transition to induce a splitting. Instead, when we used opposite circular polarizations for the pump and probe, under otherwise similar experimental conditions, we observed spectra like the one shown in Fig. 62. In this case, we observed a pronounced dip in the HH exciton absorption resonance. While the cause of this absorption dip is not readily apparent, it is clear that it is not due to Rabi splitting because as shown in Fig. 63, oppositely polarized pump and probe act on different transitions in this system.

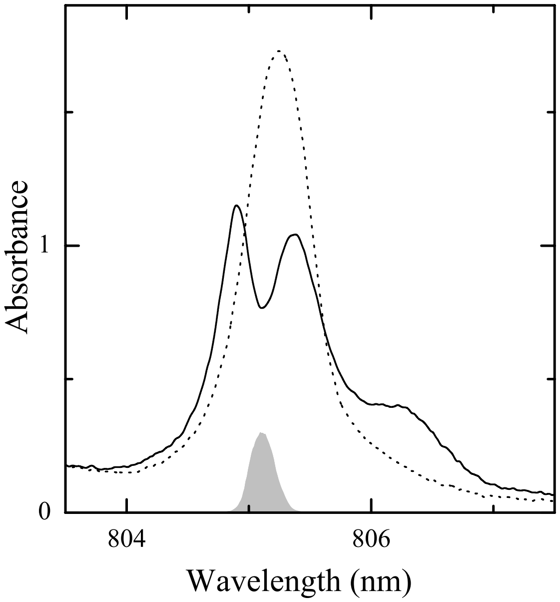

FIGURE 62. Observed dip in absorption spectrum of probe with opposite circular polarizations of pump and probe. The dotted line shows the absorption of the probe in the absence of the pump. The probe arrives 3 ps before the pump. The pump spectrum is shown as the shaded area, and the pump pulse energy flux is 400 nJ/cm^2. The sample is the 10 nm QW at 10K.

Figure 64 shows the effect of varying the delay between the pump and the probe. The absorption dip is sharper and deeper when the probe precedes the pump (as was the case for the Rabi splitting), and disappears when the probe is delayed by 6 ps. This behavior indicates that the absorption dip is caused by a coherent effect. In Fig. 65 we show the effects of changing the wavelength of the pump, and observe that the absorption dip follows the pump almost exactly.

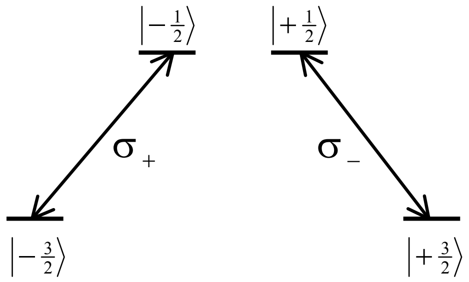

FIGURE 63. Transitions between HH valence band states and conduction band states. Transitions with opposite circular polarization share no levels.

So far, all the experimental observations are consistent with the features of EIT discussed in Chapter II, but we have yet to identify a three-level system and an underlying two-photon coherence which could lead to EIT. As noted several times before, the energy levels in Fig. 63 do not account for exciton-exciton interactions. If instead we consider the N-exciton states shown in Fig. 66(a), it appears possible to form a three-level Λ system from the two exciton spin states $|+\rangle$ and $|-\rangle$ and an interacting (but unbound) two-exciton state $|+-\rangle_u$. However, this three-level system which includes an unbound two-exciton state is certainly different from the typical atomic system. In this case, it would be a coherent superposition of the $|+\rangle$ and $|-\rangle$ states, i.e. an exciton spin coherence, which is the two-photon coherence responsible for EIT. If it is indeed possible to observe EIT in a system containing two-exciton states, then it should also be possible to form a three-level system with the bound biexciton state $|+-\rangle_b$.

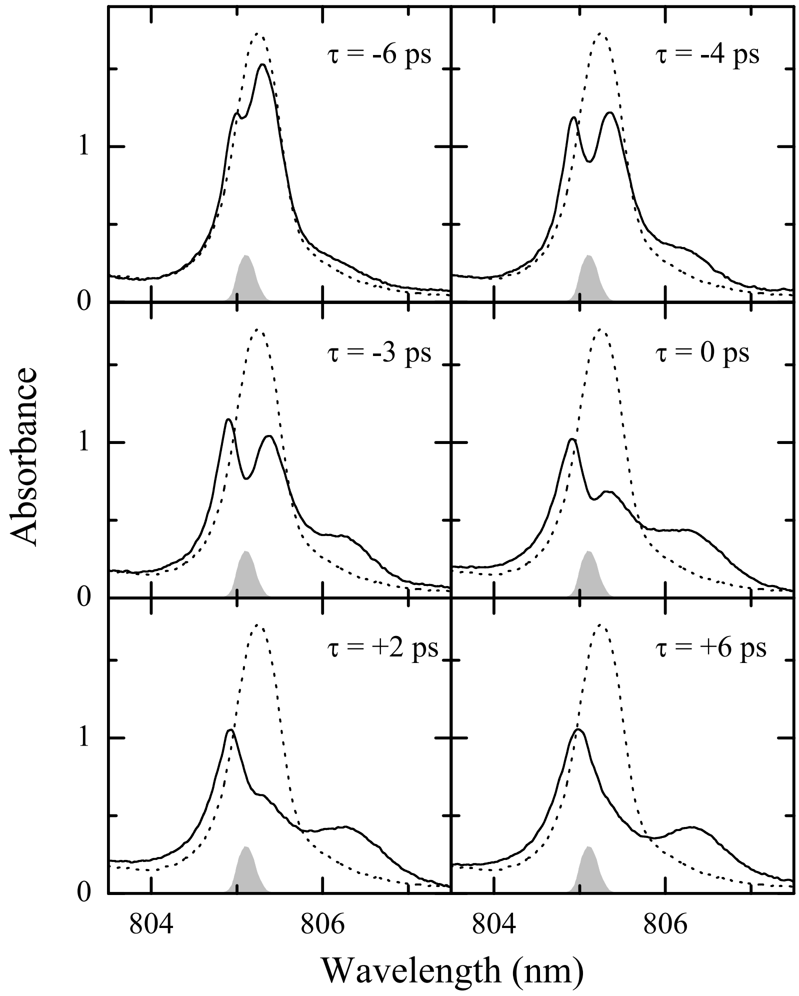

FIGURE 64. Dependence of the absorption dip on the pump-probe delay τ. Other conditions are the same as for Fig. 62

Spin Coherence Induced via the Bound Biexciton State

As shown in Fig. 29(b), we can form a Λ-type three-level system consisting of the two exciton spin states $|+\rangle$ and $|-\rangle$, and the bound biexciton state $|+-\rangle_b$. To measure EIT in this system, we apply a strong pump with σ^+ polarization to the $|-\rangle \leftrightarrow |+-\rangle_b$ transition and a weak probe with σ^- polarization to the

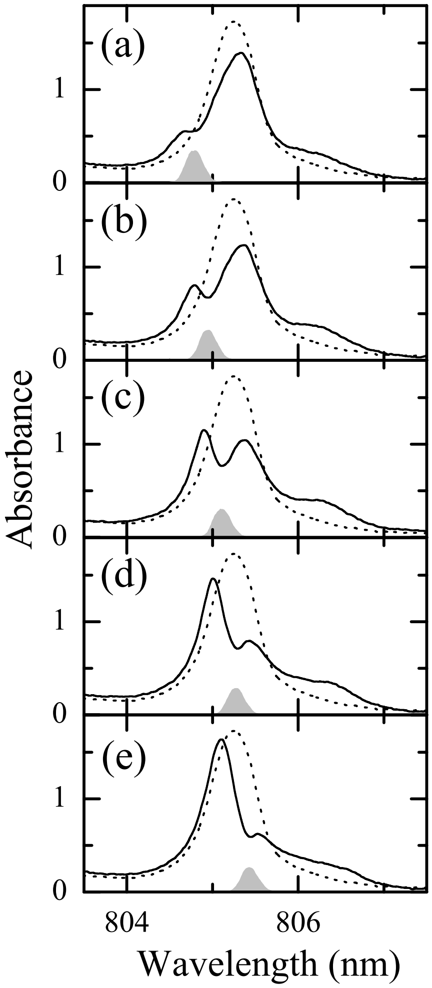

FIGURE 65. Dependence of the absorption dip on the pump wavelength. Other conditions are the same as for Fig. 62

$|+\rangle \leftrightarrow |+-\rangle_b$ transition. In this three-level system, all the levels are excited states. In order to observe EIT, we need to populate the exciton state $|+\rangle$ before the pump and probe interact with the system.

To populate the $|+\rangle$ state, we used a prepulse of 3 ps duration with σ^+ polarization that arrived 10 ps before the probe pulse. The 10 ps delay is long

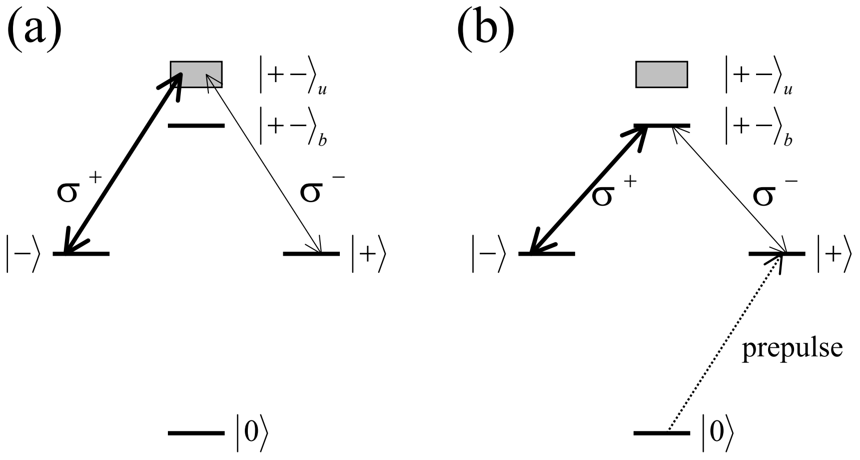

FIGURE 66. N-exciton states. The zero-exciton ground state is denoted by $|0\rangle$. The one-exciton states $|-\rangle$ and $|+\rangle$ denote spin-down and spin-up excitons, excited by σ^- and σ^+ circularly polarized light, respectively. The two-exciton states are labeled by $|+-\rangle_b$ and $|+-\rangle_u$ for the bound and unbound biexciton states, respectively.

compared to the exciton dephasing time, so that any dipole coherences induced by the prepulse cannot interfere with the observation of EIT. However, the 10 ps delay is short compared to the exciton spin relaxation time (50-100 ps) [53], so that only the $|+\rangle$ exciton state is occupied at the start of the EIT experiment. Figure 67(a) shows the spectrum of the prepulse relative to the linear absorption of the HH exciton. When the system was probed 10 ps after this prepulse (but without the pump present), the spectrum shown in Fig. 67(b) was obtained, showing the biexciton absorption resonance corresponding to the $|+\rangle \leftrightarrow |+-\rangle_b$ transition.

When the pump was then applied to the $|-\rangle \leftrightarrow |+-\rangle_b$ transition, the absorption spectrum shown in Fig. 68 was obtained. The spectrum shows a distinct dip in the biexciton resonance at the same wavelength as the pump. Figure 69

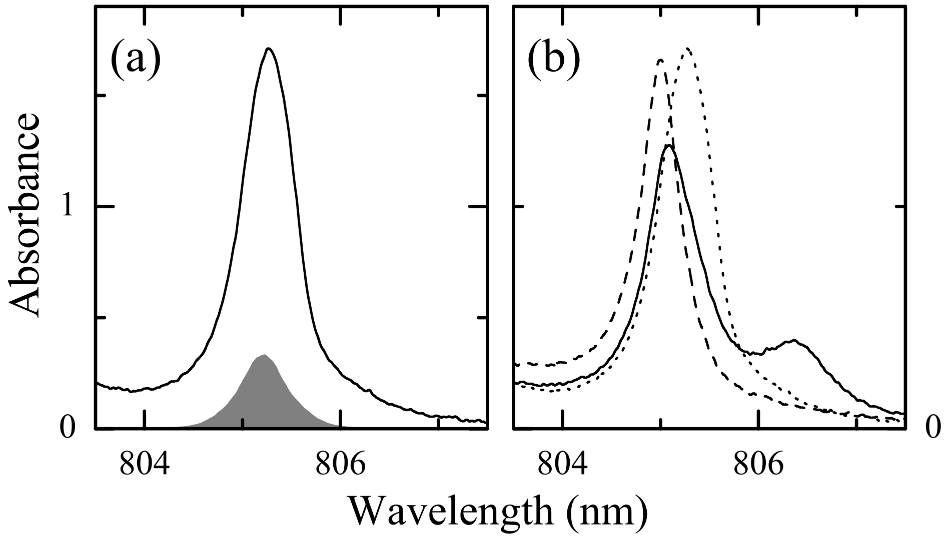

FIGURE 67. Effect of prepulse on absorption of probe. (a) Linear absorption of probe in the absence of the prepulse. The prepulse spectrum is shown by the shaded region. (b) Absorption of the σ^- probe (solid) and σ^+ probe (dashed) in the presence of the σ^+ prepulse. The dotted line shows the linear absorption for reference. The prepulse energy flux is 100 nJ/cm^2, and the probe is delayed by 10 ps relative to the prepulse.

shows the dependence of the absorption dip on the pump-probe delay. The deepest absorption dip was obtained when the probe arrived 3 ps before the peak of the pump. When the probe arrived 6 ps after the pump, the dip disappeared. This behavior verifies that we are observing a coherent effect.

Figure 70 shows that as the center wavelength of the pump was tuned around the biexciton resonance, the position of the absorption dip followed. As discussed in Chapter II, this behavior is representative of the two-photon resonance condition for a Λ system. Based on the experimental observations, combined with the three-level system we have constructed, we can conclude that the origin of this absorption

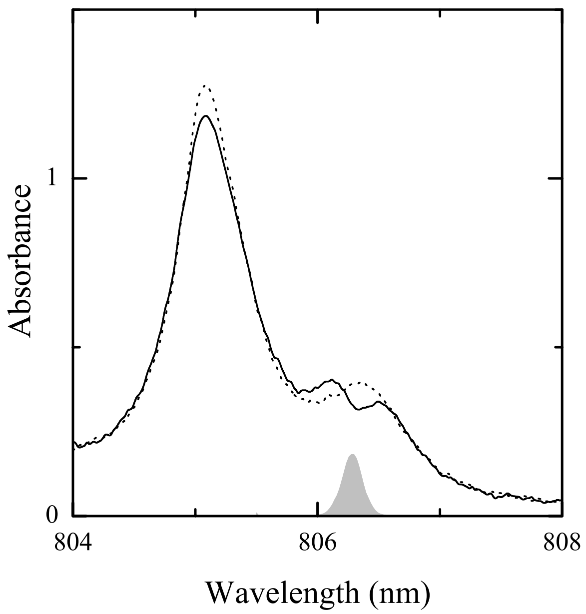

FIGURE 68. EIT of the biexciton resonance. The absorption of the σ^- probe in the presence of the σ^+ prepulse and σ^+ pump is shown by the solid line, while the dotted line shows the probe absorption in the absence of the pump. The pump and prepulse energy fluxes are 800 and 100 nJ/cm^2, respectively. The probe arrives 10 ps after the prepulse and 3 ps before the pump.

dip is EIT arising from an exciton spin coherence. Although the EIT resulting from this spin coherence shares similar properties with EIT in an atomic system, the spin coherence itself is the direct result of many-body correlations. Without the exciton-exciton interactions which lead to the biexciton state, the two excitonic transitions would be completely independent and no coherent superposition of exciton spin states could be induced.

Figure 70 also shows that the EIT dip appears sharper when the pump is on the long wavelength side of the biexciton resonance. As the pump moves to the high energy side of the biexciton resonance, the EIT dip begins to look more

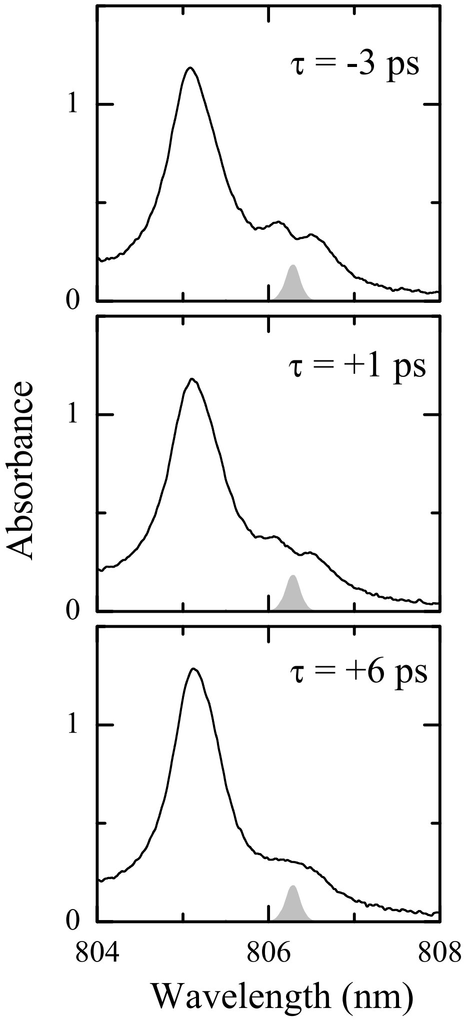

FIGURE 69. Dependence of EIT at the biexciton resonance on the pump-probe delay. The pump-probe delay τ is indicated in the figure, but otherwise the conditions are the same as for Fig. 68.

dispersive in shape. However, the pump spectrum also begins to overlap the exciton resonance, which may cause additional complications in the interpretation.

We also note that Rabi splitting of the biexciton resonance could be observed for co-circularly polarized pump and probe. This process in diagrammed in

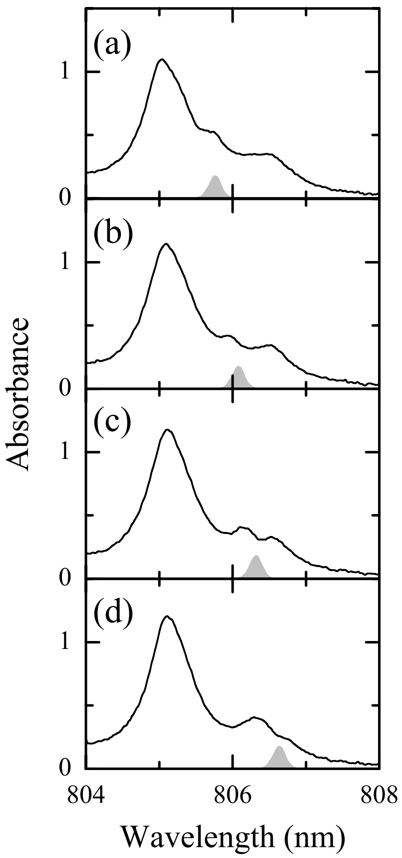

FIGURE 70. Dependence of EIT at the biexciton resonance on the pump wavelength. Other conditions are the same as for Fig. 68.

Fig. 71(a), and experimental results are shown in Fig. 71(b).

Spin Coherence Induced via Exciton Correlations

We can now understand the experiment discussed at the beginning of the chapter, where the pump was resonant with the exciton and no prepulse was present. The similar behaviors of the EIT dip for both experiments suggests that an exciton spin coherence is responsible for the EIT in both cases. While the sec-

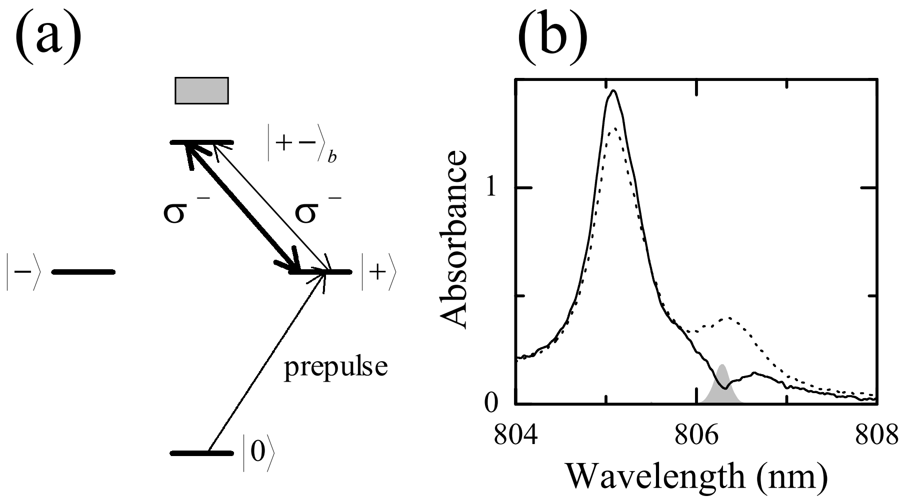

FIGURE 71. Rabi splitting of the biexciton resonance. (a) Energy level diagram for biexciton Rabi splitting. The σ^+ prepulse prepares the system with a population of $|+\rangle$ excitons. The σ^- pump and probe then measure Rabi splitting of the $|+\rangle \leftrightarrow |+-\rangle_b$ transition. (b) Experimental results, with all conditions except for the polarizations the same as for Fig. 68.

ond experiment used a bound biexciton state to couple the exciton spin states, the first experiment shows that a bound state is not required. The interactions alone are sufficient to couple the spin states.

In the first experiment, the pump pulse actually plays two roles, as shown in Fig. 72. The first role is to set up the spin coherence (acting with the probe) by coupling the $|-\rangle$ and $|+-\rangle_u$ states. But because the pump is resonant with the $|0\rangle \leftrightarrow |+\rangle$ transition, it also plays the role of the prepulse in the second experiment, by populating the $|+\rangle$ state. Both roles of the pump are necessary to observe EIT in this system.

Although we have indicated a single interacting exciton state $|+-\rangle_u$ to make clear the analogy with atomic EIT, in reality there are a continuum of interacting

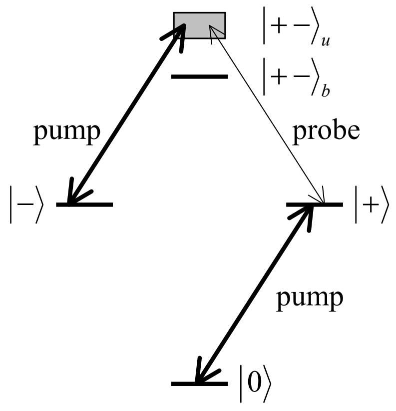

FIGURE 72. Dual role of pump for EIT at exciton resonance.

unbound two-exciton states. All of these states may contribute to the coupling of the exciton spin states, with varying degrees depending on their detuning from the pump. In this case, it is also possible that the bound biexciton state also contributes weakly to the EIT signal observed in the first experiment. We should also point out that continuum states have previously been used in atomic systems to observe EIT [2]. However, in the atomic systems the continuum states were not due to many-body interactions.

The EIT dip due to exciton spin coherence is considerably stronger than that observed for the HH-LH valence band coherence. This indicates that the spin coherence has a smaller decoherence rate than the valence band coherence. In fact, the width of the observed EIT dip may be limited by the pump spectral width, and not by the decoherence rate for the spin coherence. It is already known that the spin relaxation times for excitons are in the range of 50-100 ps [53], which sets a lower bound for the spin decoherence time. However, exciton-exciton scattering is probably the dominant contribution to the decoherence. The effects of exciton-exciton scattering are visible in Fig. 73, where we have increased the pump intensity in an effort to increase the degree of transparency. The depth of the EIT dip does not continue to increase for higher pump intensities, but instead begins to broaden. Because the pump is resonant with the exciton transition for this experiment, increasing the pump intensity increases the exciton scattering.

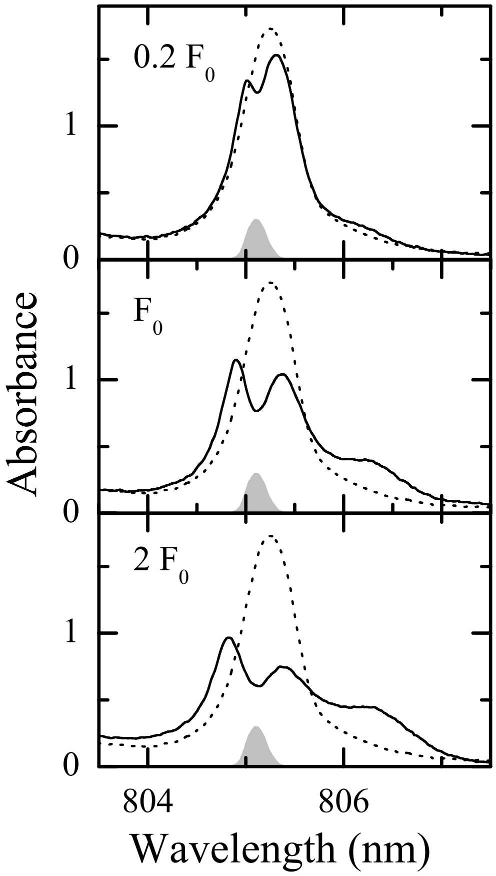

FIGURE 73. Dependence of EIT at exciton resonance on the pump intensity. The pump energy flux is indicated in the figure, with $F_0 = 400$ nJ/cm^2. Other conditions are the same as in Fig. 62

The observed EIT dip was also observed when using a spectrally narrow probe pulse, in experiments similar to those discussed in Chapter V in regard to Rabi splitting. Figure 74 shows a representative absorption spectrum obtained in this manner. These experiments more closely resemble the typical experiments in atomic systems, and may be more suited to practical applications in which all spectral components of the probe pulse are affected by the transparency. However, the decreased spectral resolution makes the narrow probe experiments less desirable as a spectroscopic tool for probing nonradiative coherences.

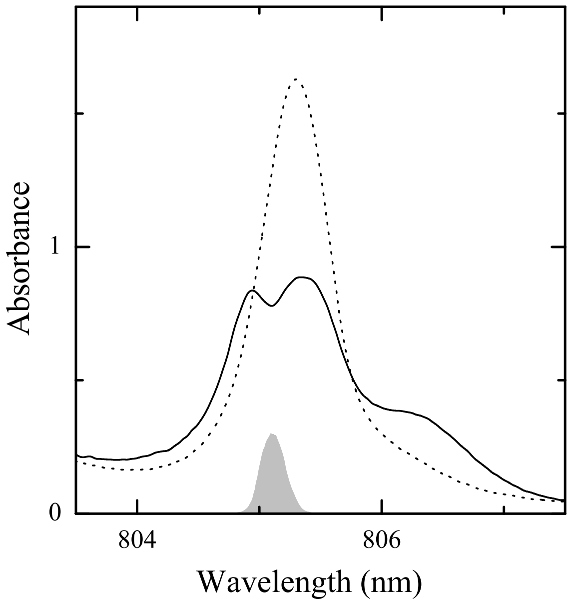

FIGURE 74. EIT at exciton resonance with spectrally narrow probe. The probe absorption is shown in the presence (solid) and absence (dotted) of a pump with opposite circular polarization. The pump duration is 6 ps, the probe duration is 8 ps, and the peaks of the pump and probe pulses arrive at the same time. The pump energy flux is 800 nJ/cm^2.

We have shown in this chapter an interesting extension of the EIT concept to a many-body semiconductor system. First, the experiments show that strong EIT signatures may be observed in a semiconductor, despite the high decoherence rates relative to atomic systems. More importantly, the experiments also show that we can use many-particle interacting states as part of a three-level system in which to observe EIT. In spite of the many-body interactions, the optical interactions leading to EIT are similar to those in an atomic system. Although the exciton-exciton interactions which lead to increased dephasing place a limit on the degree of transparency, we should not forget that the EIT would not be possible without these very interactions. In the next chapter, we will show how we can reduce the effects of exciton scattering, while still using a biexciton state, in order to observe even stronger EIT effects in a semiconductor system.

CHAPTER VIII

EIT VIA BIEXCITONIC COHERENCE

As we discovered in the last chapter, the biexciton states may be used to induce nonradiative exciton spin coherences in semiconductors. Looking at the exciton states shown in Fig. 75, we can form another three-level system using the $|0\rangle$, $|-\rangle$ (or $|+\rangle$), and $|+-\rangle_b$ states. If we apply a σ^+ pump to the $|-\rangle \leftrightarrow |+-\rangle_b$ transition, and a σ^- probe to the $|0\rangle \leftrightarrow |+\rangle$ transition, we can attempt to observe EIT in this *cascade* configuration. This system has the additional advantage that the pump is not resonant with an exciton transition, and we can therefore avoid the extra dephasing caused by EID.

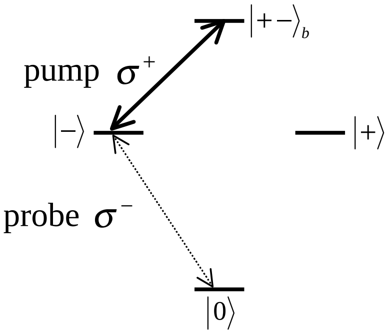

FIGURE 75. Three-level *cascade* system for EIT via biexcitonic coherence. The ground state $|0\rangle$, the HH exciton states $|-\rangle$ and $|+\rangle$, and the bound biexciton state $|+-\rangle_b$ are shown. The pump and probe fields are also shown.

In this three-level system, the nonradiative coherence generated is between the ground and biexciton states, which we call a biexcitonic coherence. Biexcitonic coherences in QWs have been explored previously in the $\chi^{(3)}$ regime [25], and were found to have significant effects on the nonlinear properties of semiconductors. In particular, the presence of a biexcitonic coherence was found to create large nonlinear signals in four-wave mixing studies [17, 18] and also to have effects in quantum beat measurements [54, 55]. The biexcitonic coherence has also been studied in QD systems [56], and plays a central role in the development of quantum information processing schemes in those systems.

Our experiments focus on two aspects of the biexcitonic coherence. First, we wish to see if a large enough biexcitonic coherence can be generated to observe EIT. Previous studies have indicated that the biexcitonic decoherence rate is comparable to the exciton decoherence rate [18], which could make EIT difficult to observe. On the other hand, the effects of EID should be minimized in this system, so at least the decoherence rates should not increase much further. The second aim is to use the EIT experiments to explore the properties of the biexcitonic coherence. By doing so, we hope to gain more understanding about nonradiative coherences in many-body systems.

Experimental Results

The experimental setup and methods were the same as for the previous experiments in this dissertation. The 6 ps pump pulses with σ^+ polarization were tuned to be resonant with the exciton to biexciton transition. The 150 fs probe pulses with σ^- polarization measured the absorption spectrum in the presence of the pump. Based on the level diagram, we would expect to see the EIT dip appearing at the HH exciton resonance. We found that the strongest EIT signatures were observed using the 17.5 nm MQW, and all results in this chapter are from this sample.

In order to locate the spectral position of the exciton to biexciton transition, we set the pump resonant with the exciton and measured the probe absorption at 10 ps after the pump. The spectrum in Fig. 76 shows the biexciton resonance, from which we calculate a biexciton binding energy of 1.6 meV.

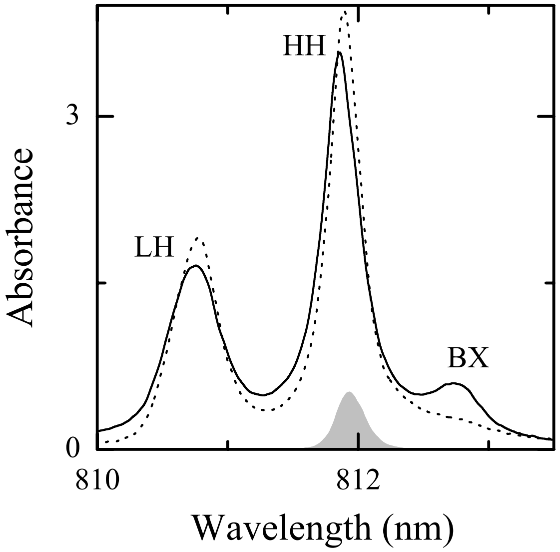

FIGURE 76. Location of the biexciton resonance. The curves show the probe absorption in the presence (solid) and absence (dotted) of the pump. The pump is resonant with the exciton transition, and the pump spectrum is shown as the shaded area. The pump pulse energy flux is 40 nJ/cm^2, and the probe arrives 10 ps after the peak of the pump.

If the pump was tuned resonant with the biexciton transition, we observed the spectrum in Fig. 77. The spectrum is not symmetric as we would expect from an atomic model, but a small EIT does appear on the high energy side of the exciton peak. From the two-photon resonance condition for the biexcitonic coherence, we would expect the EIT dip to be positioned exactly at center of the exciton peak.

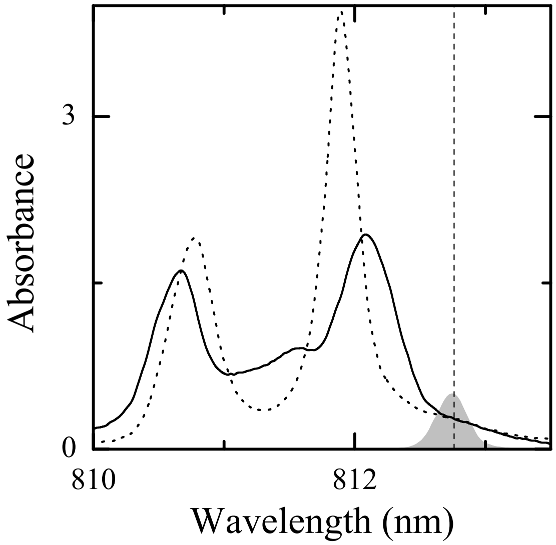

FIGURE 77. EIT via biexcitonic coherence. The pump is resonant with the biexciton transition, where the center of the biexciton transition is indicated by the dashed line. The pump pulse energy flux is 2 μJ/cm^2, and the probe arrives 1 ps before the peak of the pump.

If instead the pump was tuned in between the biexciton and exciton transitions, the spectrum shown in Fig. 78 was observed. The EIT dip is now positioned at the center of the exciton resonance. In this case, the absorption is reduced by factor of $\exp(3.1) = 22$ at the center of the HH exciton. This represents the greatest degree of transparency due to EIT we have observed so far.

The dependence of the EIT dip in the absorption spectrum on the pump-probe delay is shown in Fig. 79. In this experiment, the depth of the EIT dip is more symmetric about $\tau = 0$ than it was for the other EIT experiments; however, it is still resolved slightly better for negative delays. The absorption spectrum

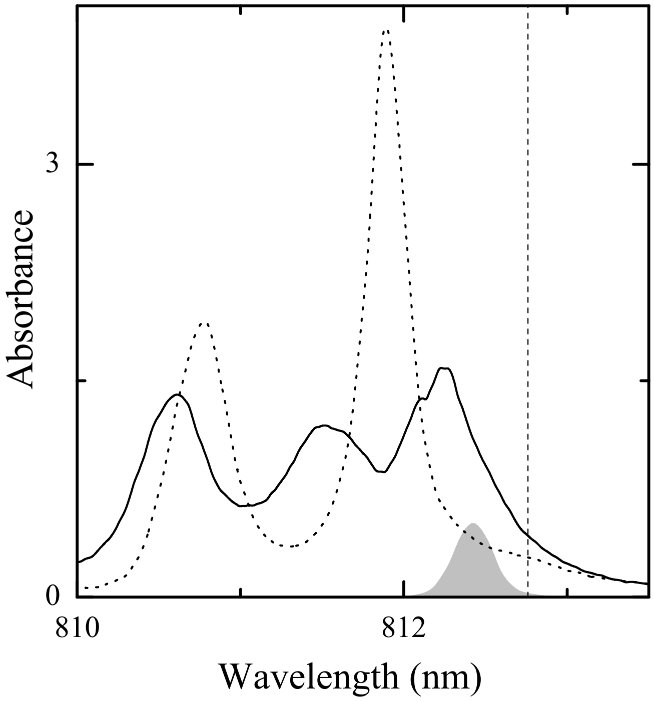

FIGURE 78. Improved EIT via biexcitonic coherence. The pump is now above the biexciton transition energy, where the center of the biexciton transition is indicated by the dashed line. Other conditions are the same as for Fig. 77.

at $\tau = +10$ ps matches the linear absorption almost exactly. This behavior is particularly interesting, because it shows that the EIT process in this experiment is almost fully coherent. In other words, the pump pulse does not excite a significant real exciton population.

We have already noticed that the EIT dip is not in the expected position based on the two-photon resonance condition. In Fig. 80 we show further effects of changing the pump excitation wavelength. As the pump is moved to higher energies relative to the biexciton, the EIT dip moves to lower energies relative to the exciton. This behavior confirms that we are observing EIT in a *cascade* system,

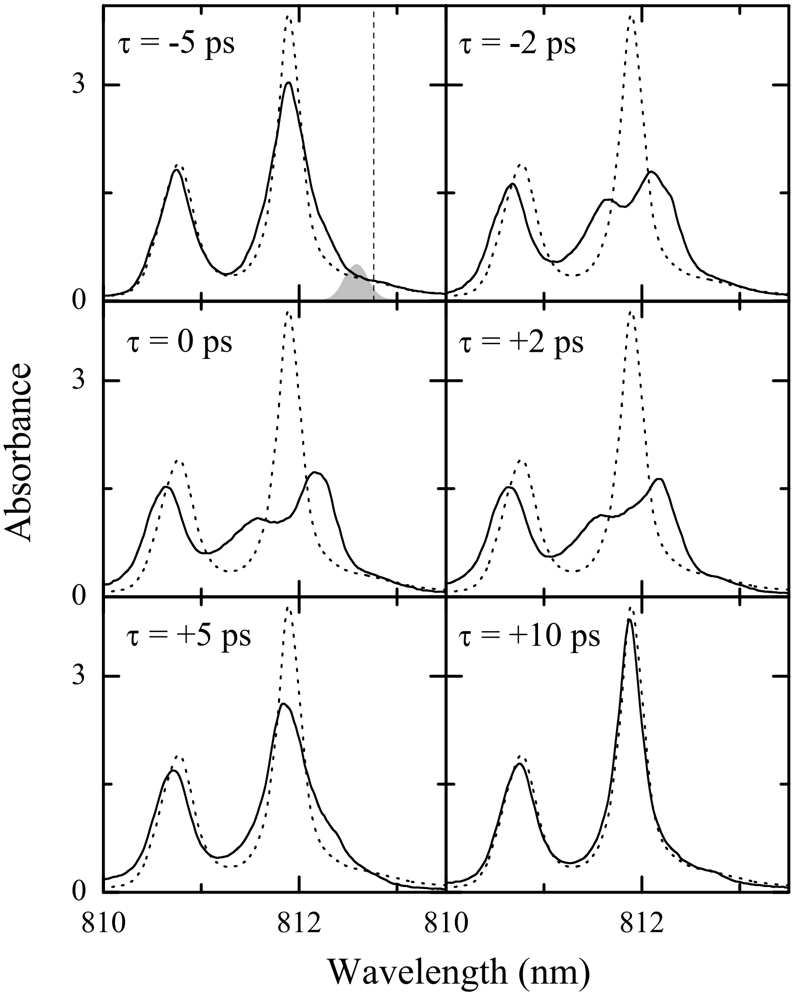

FIGURE 79. Dependence of EIT on pump-probe delay. The pump-probe delay τ is indicated in the figure. The pump spectrum is indicated by the shaded area, and the pump pulse energy flux is 1.6 μJ/cm^2.

where the two-photon resonance condition of $\delta_b = -\delta_a$ is expected, as explained in Chapter II. Also note that in Fig. 80(d), an additional dip can be seen, which is centered at the pump. This dip appears similar to the one we observed due to exciton spin coherence, though its exact source is unknown at this time.

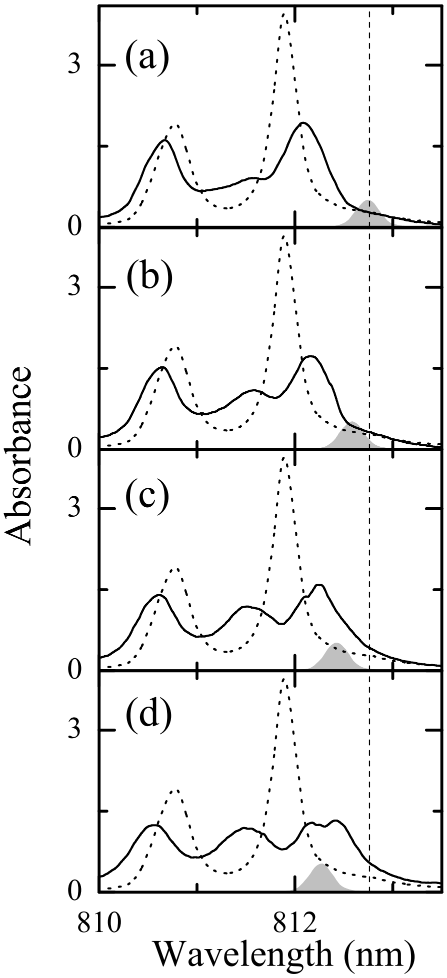

FIGURE 80. Dependence of EIT on pump excitation wavelength. The pump spectrum is indicated by the shaded area. Other conditions are the same as for Fig. 77.

In Fig. 81 we plot the absorption spectrum for increasing pump intensity. Here we notice a very interesting behavior: the position of the EIT dip changes with the pump intensity. For the lowest intensity, the EIT dip appears on the low energy side of the HH exciton. This is consistent with the atomic model two-photon resonance condition, because the pump is on the high energy side of the biexciton transition. At higher pump intensities, however, the EIT dip moves to higher energy. We will discuss this interesting behavior, which is not predicted by atomic models, in the next section.

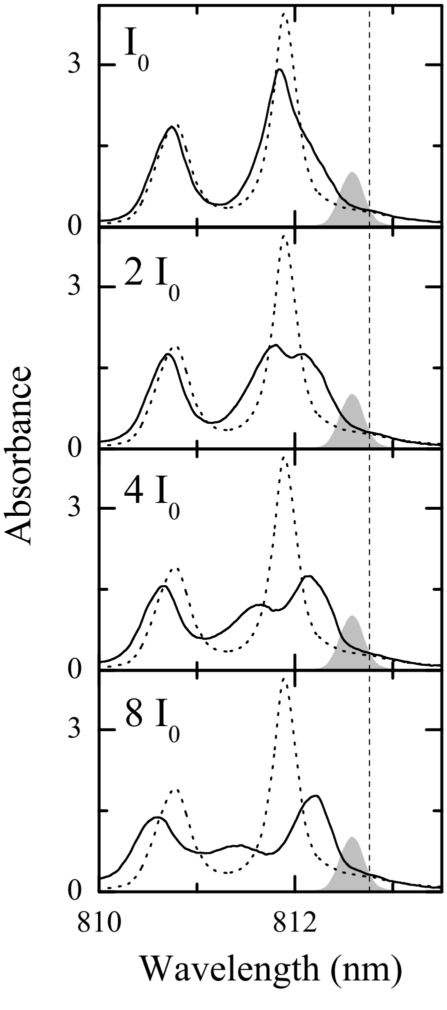

FIGURE 81. Dependence of EIT on pump intensity. The pump pulse energy flux is indicated in the figure, with $I_0 = 400\text{nJ/cm}^2$. Other conditions are the same as for Fig. 77.

Effects of Many-Body Interactions

The shift of the EIT dip with increasing pump intensity indicates that the two-photon resonance condition is varying. In our *cascade* system, the only way for this to happen is if the energy of the biexciton state changes. Formally, the two-photon resonance condition is $E_{EIT} = E_b - E_{pump}$, where E_{EIT} is the energy position of the EIT dip, E_b is the total energy for the biexciton state, and E_{pump} is the energy position of the pump. This situation is diagrammed in Fig. 82, where we can see that the energy of the exciton state $|-\rangle$ does not affect the two-photon resonance condition.

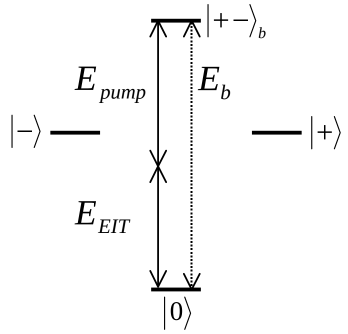

FIGURE 82. Two-photon resonance condition in biexciton system.

The observed shift of the EIT to higher energy therefore indicates that the biexciton energy level is also shifting to higher energy. We can introduce this behavior into our OBE model for EIT by changing the biexciton energy depending on the pump intensity. To isolate the effects of the two-photon resonance from any effects due to transient pump and probe pulses, we present results from analytic solutions of the OBE for CW pump and probe. The solutions are similar to those discussed in Chapter II, but the OBE are taken for a *cascade* instead of a Λ system. Details of the derivation of the OBE for the *cascade* system are given in Appendix B. To account for the shift in the biexciton energy, we take $E_b = E_b^0 + \hbar\beta\Omega_{pump}^2$, where E_b^0 is the energy of the biexciton in the absence of the pump, Ω_{pump} is the Rabi frequency of the pump, and β is a factor giving the strength of the shift. We can then write the pump detuning as $\delta_{pump} = \delta_{pump}^0 - \beta\Omega_{pump}^2$. This form for the biexciton energy is used so that the shift of the biexciton is linear with the pump intensity, for reasons which will become clear shortly.

In Fig. 83 we plot the EIT spectrum for the case where the pump is resonant with the unshifted biexciton transition, and under the conditions $\gamma_b = \gamma$ and $\Omega_{pump} = 2\gamma$. Note that for the theoretical calculations, we plot the detuning in frequency, which is inversely related to the wavelength. Fig. 83(a) shows the spectrum for $\beta = 0$ so that there is no shift of the biexciton. The dashed curve gives a reference for where the biexciton absorption resonance is located, and the pump is indicated by the sharp spike. The EIT dip is positioned at the center of the exciton resonance. Fig. 83(b) shows how the result changes when the biexciton shift is included by setting $\beta = 0.3\gamma^{-1}$. In this case, the shift in the biexciton energy means that the pump is actually below the biexciton resonance. Therefore, the EIT dip appears on the high energy side of the exciton peak. This behavior is similar to what we observed in the experiments.

The change in the EIT dip position with pump intensity can also be reproduced, as shown in Fig. 84. The pump position is in between the exciton and the unshifted biexciton resonances. Even though the pump position remains fixed as the intensity increases, the shift in energy of the biexciton resonance leads to

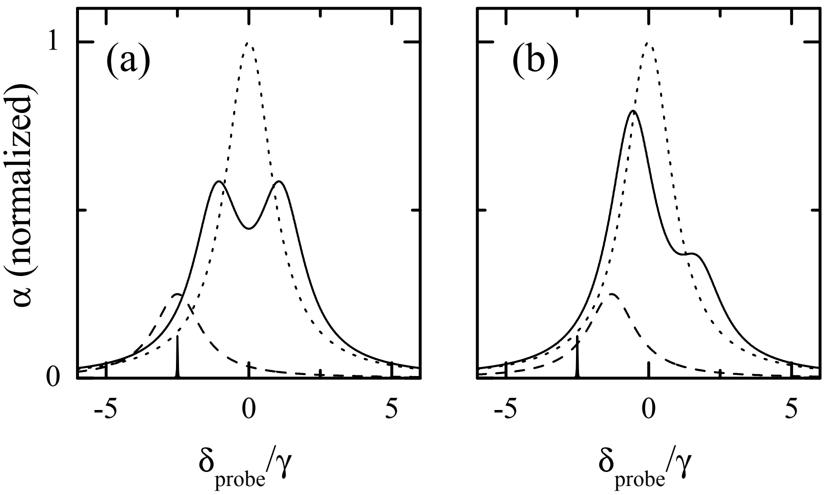

FIGURE 83. Effect of biexciton energy shift. Curves give the calculated absorption of probe as a function of probe detuning δ_{probe} in the presence (solid) and absence (dotted) of the pump. The dashed line shows the position of the biexciton resonance and the sharp spike shows the pump position. (a) $\beta = 0$. (b) $\beta = 0.3\gamma^{-}1$. For both parts, $\Omega_{pump} = 2\gamma$ and $\gamma_b = \gamma$.

changes in the EIT position. At low intensity, the biexciton shift is small and the EIT dip appears on the low energy side of the exciton. As the intensity increases, the biexciton shifts so that the pump is now below it. Therefore, the EIT dip appears on the high energy side of the exciton.

The EIT experiments have shown us that the biexciton shifts to higher energy with increasing pump intensity, and we can now turn to explanations for this behavior. Because the biexciton is composed of two excitons, we can write its energy as follows: $E_b = E_+ + E_- - E_{binding}$, where E_+ and E_- are the energies of noninteracting $|+\rangle$ and $|-\rangle$ excitons, and $E_{binding}$ is the biexciton binding energy. If we look back at the exciton state diagram, the pump is not only resonant with the $|-\rangle \leftrightarrow |+-\rangle_b$ transition, it is also acting on the $|0\rangle \leftrightarrow |+\rangle$ transition. We know

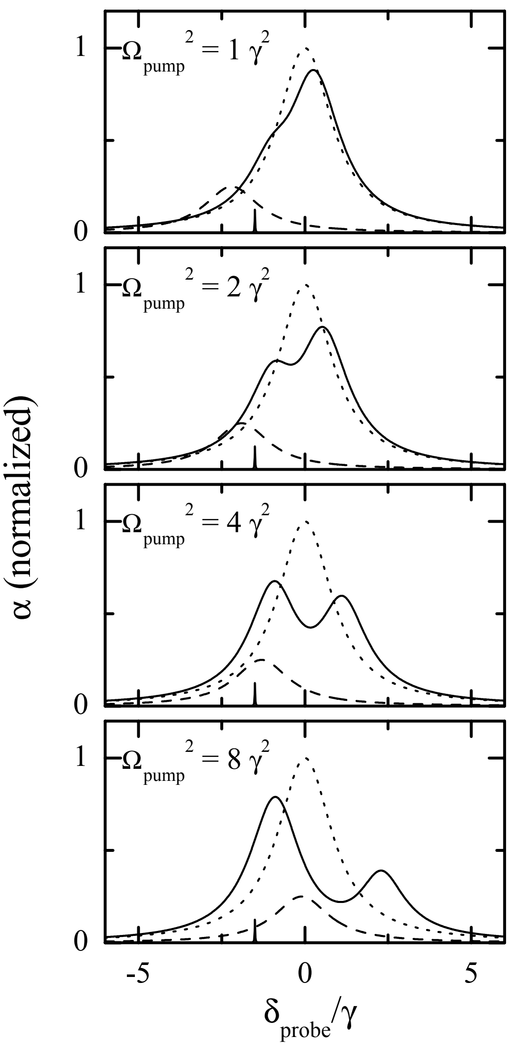

FIGURE 84. Effects of intensity dependent biexciton shift. The pump rabi frequencies are shown in the figure. Other parameters are $\beta = 0.3\gamma^{-}1$ and $\gamma_b = 0.75\gamma$.

from our previous experiments that because the pump is below this transition, it causes an optical Stark shift of the $|+\rangle$ exciton to higher energy. This energy shift of the $|+\rangle$ exciton causes a corresponding energy shift of the biexciton energy. This process is diagrammed in Fig. 85.

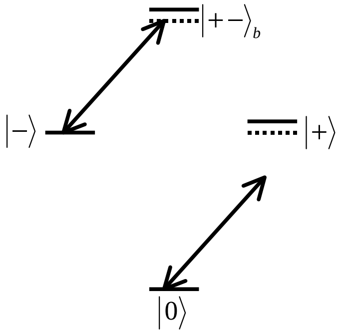

FIGURE 85. Effect of optical Stark shift on biexciton energy.

In Fig. 86 we plot the energy position of the EIT dip relative to the HH exciton as a function of pump intensity, as measured from the spectra shown in Fig. 81 and additional spectra not plotted. We also plot the optical Stark shift of the HH exciton, measured from spectra taken under identical conditions, except with pump and probe having the same circular polarization. The position of the EIT dip follows the HH stark shift closely except at the highest pump intensities. The nearly linear dependence of the shifts on the pump intensity also justifies our choice in the theoretical calculations. The data confirms that at low pump intensities, the dominant cause of the biexciton energy shift is the optical Stark shift of the $|+\rangle$ exciton. Also, Coulomb correlations can strongly affect the biexciton binding energy, which explains the nonlinear behavior of the EIT position at higher pump intensities.

Our simple OBE model qualitatively explains the observed behavior and gives insight into the physical processes at play. We also note that the experiment has recently been studied using microscopic semiconductor calculations, in a collaboration with I. Rumyantsev, N.H. Kwong, R. Takayama, and R. Binder [31].

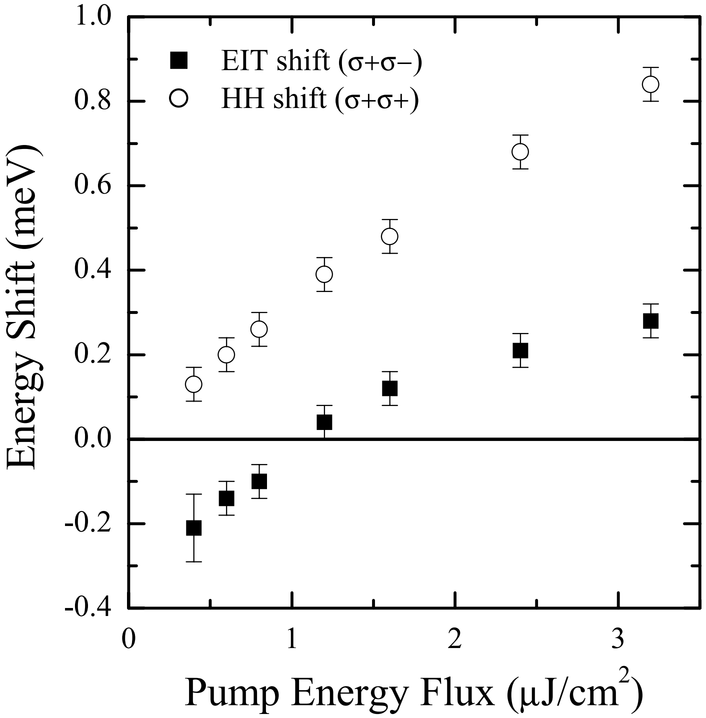

FIGURE 86. Energy shift of the EIT dip. The shift of the EIT dip relative to the HH exciton is plotted as the filled squares. The optical Stark shift of the HH exciton (measured with $\sigma^+\sigma^+$ pump and probe), is also plotted as the open circles. The experimental conditions are the same as in Fig. 81.

The more rigorous semiconductor theory confirms the energy shift of the biexciton, and also predicts the observed shift of the EIT position.

We have shown in this chapter a demonstration of EIT in semiconductors based on a biexcitonic coherence. We can produce strong EIT signatures for this experiment in part because the effects of decoherence due to EID are minimized. In addition to producing EIT, we have also used the experiment to study the physics of the exciton-biexciton system. The changing energy position of the EIT dip gives direct evidence for an energy shift of the biexciton, which we attribute primarily to an exciton optical Stark shift caused by the pump. The results again confirm that it is possible to observe EIT based on nonradiative coherences induced via many-exciton states. And the results further show that, as it was for the exciton spin coherence, the many-body nature of the semiconductor system cannot be ignored.

CHAPTER IX

SUMMARY AND FUTURE WORK

Summary

This dissertation has presented experimental verification that EIT is possible in a semiconductor system, despite the high decoherence relative to atomic systems. We have demonstrated EIT in three different excitonic systems, which rely on three different nonradiative coherences to cause the destructive interference. Furthermore, we have used the EIT experiments to gain insight into the properties of the nonradiative quantum coherences themselves.

The first system discussed was a V system composed of HH and LH exciton states coupled through the ground state. This system had previously been proposed as a candidate for semiconductor EIT studies, but the experimental verification had been absent. Our observations show that nonradiative coherence between valence band states can be generated and used to cause EIT; however, the degree of transparency attained was weak. The limitation was found to result from a high decoherence rate for the valence band coherence. The decoherence was made even worse at higher excitation levels, due to additional dephasing from exciton-exciton scattering. We concluded that a V configuration is not ideal for semiconductor EIT studies, because the strong pump necessarily excites a large exciton population.

We next discussed EIT which arose from a nonradiative exciton spin coherence. We showed that the spin coherence could be generated by coupling the exciton spin states through the bound biexciton resonance, in which the EIT occurred at the bound biexciton transition energy. We also showed that the spin coherence could be generated by coupling the spin states through the unbound biexciton continuum. In this case, a strong EIT dip occurred at the HH exciton transition energy. The exciton spin coherence is particularly interesting because it would not be possible without the many-body interactions present in a semiconductor system. We further showed that the magnitude of the EIT signatures in these experiments reflects a small decoherence rate for the exciton spin coherence. However, because the pump is again resonant with the HH exciton transition in these experiments, decoherence from EID places a limit on the transparency achievable.

The third system in which we observed EIT was a *cascade* system composed of the ground, exciton, and bound biexciton states. By applying the pump to the exciton-biexciton transition, we avoided the EID effects observed in the previous experiments, and were able to observe strong EIT signatures at the HH exciton transition. These experiments represent the highest degree of transparency we were able to attain, showing a factor of twenty reduction in the absorption. We also observed behaviors due to many-body interactions in this system. Because the biexciton state energy depends on the energy of both exciton spin states, the pump was found to cause a shift in the biexciton energy via the optical Stark effect on an exciton state not directly involved in the EIT process.

In addition to the EIT observations, we have studied Rabi splitting of excitons. These experiments are valuable for demonstrating the correct conditions for the observation of EIT, but they were also useful for studying the effects of many-body interactions in a high excitation regime. We found that the shift of the exciton energy due to exchange interactions had a large effect on the observed lineshapes. A pump pulse that is initially resonant with the exciton transition therefore becomes off-resonant as the exciton density increases during the pump pulse.

Both the EIT and Rabi splitting experiments also showed that using a temporally long pump and short probe can be a useful spectroscopic technique. By having the probe pulse arrive before the peak of the pump pulse, the probe can monitor the coherent properties of the system as it is driven by the pump, but before a large steady-state incoherent exciton population is generated. In a semiconductor, this technique is extremely valuable because it avoids the large increased decoherence caused by the exciton population. We also showed that the potential complication of coherent spectral oscillation in these experiments can be avoided by using a pump pulse which is long relative to the exciton dipole decoherence time.

Future Work

Concerning EIT in the systems discussed here, there are a few additional experiments which could increase our understanding. In our experiments, the pump spectral width places a limit on the width of the EIT dip which can be observed. We therefore could only place an upper limit on the decoherence rate for the spin coherence at low exciton densities. Additional experiments could be performed if the pulse shaping apparatus was improved so that narrower pump spectral widths were available. In order to observe EIT, it is likely that additional amplification of the pump pulses would then be necessary. Also, in our experiments we have restricted our attention to the circularly polarized optical transitions, as that is the natural basis for discussing biexcitons. A study of the linearly polarized transitions may yield additional information about the system.

The EIT experiments discussed here could also be performed in other semiconductor systems. The biexciton binding energy in ZnSe is much larger than in GaAs, and experiments in ZnSe systems could better isolate the exciton and biexciton transitions from each other. The phenomenon of EIT can also be explored in lower dimensional structures such as quantum dots, and our experiments strongly suggest that observation of EIT will be possible.

The exciton spin decoherence is believed to be dominated by the faster hole spin relaxation relative to the electron spin. For semiconductors in magnetic fields, or engineered magnetic semiconductors, the electron spin levels can split and the optical selection rules change so that an electron spin coherence can be generated. It is hoped that the low decoherence rate for the electron spin coherence will allow for very strong EIT effects to be observed. Studies of these systems are already underway in the Wang lab.

The demonstration of EIT in semiconductors opens the door to the wide variety of related phenomena which depend on the quantum interference caused by a nonradiative coherence. A study of the changes to the index of refraction associated with EIT has yet to be made in semiconductors. The implementation of slow light phenomena in semiconductors could have many technological applications. There is also the possibility of designing semiconductor inversionless lasers based on the generation of nonradiative coherences. The successful demonstrations of both Rabi oscillations and EIT also show that it is possible to coherently control both dipole and nonradiative coherences in semiconductors, which can provide direct control over the semiconductor's optical properties. It also increases the possibility of semiconductor-based quantum information processing, where information is stored in the quantum coherences of the system.

While the technological implications of EIT in semiconductors are certainly interesting, it is also hoped that the experiments discussed here lead to a better understanding of the optical properties of many-body systems. Current semiconductor theory is for the most part unable to handle the effects of correlations in highly nonlinear optical processes such as EIT. In order to fully describe EIT in semiconductors, additional theoretical progress will be required. We will conclude by noting that the collaborations resulting from our experimental observations of EIT due to the biexcitonic coherence have already led to advances in the theoretical modeling of semiconductors.

APPENDIX A

DERIVATION OF OPTICAL BLOCH EQUATIONS FOR RABI SPLITTING IN TWO-LEVEL SYSTEMS

This appendix details the derivation of the equations describing a two-level system subject to a strong pump and a weak probe optical field. The OBE for the this system are derived, including semiconductor many-body corrections. A similar derivation, without the semiconductor corrections, is given in Ref. [29].

We begin by writing the OBE for a two-level system with ground state $|g\rangle$ and excited state $|e\rangle$ separated in energy by $\hbar\omega$.

$$\dot{\rho}_{eg} = -\left(i\omega + \gamma + \sigma\rho_{ee}\right)\rho_{eg} - \frac{i\mu}{\hbar}\mathcal{E}\left(2\rho_{ee} - 1\right) \tag{A.1}$$

$$\dot{\rho}_{ee} = -\Gamma\rho_{ee} - \frac{i\mu}{\hbar}\left(\mathcal{E}\rho_{eg} - c.c.\right) \tag{A.2}$$

where we have assumed that $\rho_{ee} + \rho_{gg} = 1$. In these equations γ is the polarization dephasing rate, Γ is the population decay rate of state $|e\rangle$ and μ is the dipole matrix element (assumed to be real). The effects of excitation induced dephasing (EID) are included by the term including the constant σ.

The electric field $\mathcal{E}$ includes contributions from both the pump and probe fields.

$$\mathcal{E} = \mathcal{E}_s + \mathcal{E}_p = \frac{1}{2}\left[E_s(t)e^{i(k_s\cdot r-\nu_s t)} + E_p(t)e^{i(k_p\cdot r-\nu_p t)} + c.c.\right] + L\mu\left(\rho_{eg} + c.c.\right) \quad (A.3)$$

where the subscript s refers to the strong pump (saturator) field, and the subscript p refers to the weak probe field. The constant L accounts for the Lorentz local field corrections.

To solve the OBE we assume that the probe field is weak and therefore keep terms up to first order in E_p. The pump field is assumed strong and we keep terms to all orders in E_s.

To zeroth order in the probe, we obtain the following equations:

$$\dot{\rho}_{eg}^{(0)} = -\left(i\omega + \gamma + \sigma\rho_{ee}^{(0)}\right)\rho_{eg}^{(0)} - \frac{i\mu}{\hbar}\mathcal{E}_s\left(2\rho_{ee}^{(0)} - 1\right) \quad (A.4)$$

$$\dot{\rho}_{ee}^{(0)} = -\Gamma\rho_{ee}^{(0)} - \frac{i\mu}{\hbar}\left(\mathcal{E}_s\rho_{eg}^{(0)} - c.c.\right) \quad (A.5)$$

We make the following substitutions:

$$\rho_{eg}^{(0)} = p_0 e^{-i\nu_s t} \quad (A.6)$$

$$\rho_{ee}^{(0)} = n_0 \quad (A.7)$$

and after making the rotating wave approximation (RWA), the zeroth order OBE reduce to

$$\dot{p}_0 = \left(i\delta_s - \gamma - \sigma n_0\right) p_0 - \frac{i}{2}\left(\Omega_s + \eta p_0\right)\left(2n_0 - 1\right) \tag{A.8}$$

$$\dot{n}_0 = -\Gamma n_0 - \frac{i}{2}\left(\Omega_s^* p_0 - c.c.\right) \tag{A.9}$$

where $\delta_s = \nu_s - \omega$, $\Omega_s = \frac{\mu E_s}{\hbar} e^{ik_s \cdot r}$, and $\eta = \frac{2\mu^2 L}{\hbar}$. These two equations give the response of the system to the pump field in the absence of the probe.

Keeping terms of first order in E_p yields the following equations.

$$\dot{\rho}_{eg}^{(1)} = -\left(i\omega + \gamma + \sigma\rho_{ee}^{(0)}\right)\rho_{eg}^{(1)} - \sigma\rho_{ee}^{(1)}\rho_{eg}^{(0)} - \frac{i\mu}{\hbar}\mathcal{E}_p\left(2\rho_{ee}^{(0)} - 1\right) - \frac{i\mu}{\hbar}\mathcal{E}_s\left(2\rho_{ee}^{(1)}\right) \tag{A.10}$$

$$\dot{\rho}_{ee}^{(1)} = -\Gamma\rho_{ee}^{(1)} - \frac{i\mu}{\hbar}\left(\mathcal{E}_p\rho_{eg}^{(0)} - c.c.\right) - \frac{i\mu}{\hbar}\left(\mathcal{E}_s\rho_{eg}^{(1)} - c.c.\right) \tag{A.11}$$

We will next make the following substitutions:

$$\rho_{eg}^{(0)} = p_0 e^{-i\nu_s t} \tag{A.12}$$

$$\rho_{eg}^{(1)} = p_1 e^{-i\nu_p t} + p_f e^{-i(2\nu_s - \nu_p)t} \tag{A.13}$$

$$\rho_{ee}^{(1)} = n_1 e^{i(\nu_s - \nu_p)t} \tag{A.14}$$

Note that $\rho_{eg}^{(1)}$ contains terms oscillating at two different frequencies and that these terms are coupled via n_1. We will split the equation for $\rho_{eg}^{(1)}$ into two parts based on the oscillation frequency. After making the RWA, we therefore derive the following three equations.

$$\dot{n}_1 = -\left(i\Delta + \Gamma\right) n_1 + \frac{i}{2}\Omega_p p_0^* - \frac{i}{2}\Omega_s^* p_1 + \frac{i}{2}\Omega_s p_f^* \tag{A.15}$$

$$\dot{p}_f = \left(i\delta_3 - \gamma - \sigma n_0\right) p_f - \left(i\Omega_s + i\eta p_0 + \sigma p_0\right) n_1^* - \frac{i}{2}\eta p_f \left(2n_0 - 1\right) \tag{A.16}$$

$$\dot{p}_1 = \left(i\delta_p - \gamma - \sigma n_0\right) p_1 - \frac{i}{2}\left(\Omega_p + \eta p_1\right)\left(2n_0 - 1\right) - \left(i\Omega_s + i\eta p_0 + \sigma p_0\right) n_1 \tag{A.17}$$

where $\Delta = \nu_s - \nu_p$, $\delta_p = \nu_p - \omega$, $\delta_3 = 2\nu_s - \nu_p - \omega$, and $\Omega_p = \frac{\mu E_p}{\hbar} e^{ik_p \cdot r}$.

Now if we let $p_{fwm} = p_f^*$, and also eliminate the static Lorentz Shift terms, we arrive at the following set of OBE.

$$\dot{p}_0 = \left[i\delta_s - \gamma - \left(\sigma + i\eta\right) n_0\right] p_0 - \frac{i}{2}\Omega_s \left(2n_0 - 1\right) \tag{A.18}$$

$$\dot{n}_0 = -\Gamma n_0 - \frac{i}{2}\left(\Omega_s^* p_0 - c.c.\right) \tag{A.19}$$

$$\dot{n}_1 = -\left(i\Delta + \Gamma\right) n_1 + \frac{i}{2}\Omega_p p_0^* - \frac{i}{2}\Omega_s^* p_1 + \frac{i}{2}\Omega_s p_{fwm} \tag{A.20}$$

$$\dot{p}_{fwm} = -\left[i\delta_3 + \gamma + (\sigma - i\eta)\, n_0\right] p_{fwm} + \left(i\Omega_s^* + i\eta p_0^* - \sigma p_0^*\right) n_1^* \tag{A.21}$$

$$\dot{p}_1 = \left[i\delta_p - \gamma - (\sigma + i\eta)\, n_0\right] p_1 - \frac{i}{2}\Omega_p\, (2n_0 - 1) - \left(i\Omega_s + i\eta p_0 + \sigma p_0\right) n_1 \tag{A.22}$$

APPENDIX B

DERIVATION OF OPTICAL BLOCH EQUATIONS FOR EIT IN THREE-LEVEL SYSTEMS

This appendix shows how the OBE are derived for various three-level systems. First we write down the Hamiltonian and density matrix operators for the three-level systems under consideration. We then proceed to derive the OBE and discuss EIT for a weak probe field in each system.

Hamiltonian

We consider three-level systems with states $|a\rangle$, $|b\rangle$, and $|e\rangle$ (or $|g\rangle$), as shown in Fig. 87. The states have energies $\hbar\omega_{aa}$, $\hbar\omega_{bb}$, $\hbar\omega_{ee}$, respectively. We will refer to the three systems as Λ, *cascade*, and V systems. Two electric fields are applied: $\mathcal{E}_a$ which excites the $|a\rangle \leftrightarrow |e\rangle$ transition, and $\mathcal{E}_b$ which excites the $|b\rangle \leftrightarrow |e\rangle$ transition. The $|a\rangle \leftrightarrow |b\rangle$ transition is dipole forbidden.

The Hamiltonian for the system may be written as $\mathcal{H} = \mathcal{H}_0 + V$, where

$$\mathcal{H}_0 = \hbar \begin{pmatrix} \omega_{ee} & 0 & 0 \\ 0 & \omega_{aa} & 0 \\ 0 & 0 & \omega_{bb} \end{pmatrix} \tag{B.1}$$

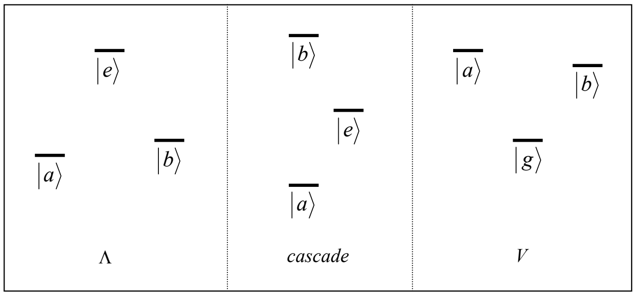

FIGURE 87. Three-level systems discussed in appendix

and

$$V = -\begin{pmatrix} 0 & \mu_a\mathcal{E}_a & \mu_b\mathcal{E}_b \\ \mu_a\mathcal{E}_a & 0 & 0 \\ \mu_b\mathcal{E}_b & 0 & 0 \end{pmatrix} \tag{B.2}$$

The dipole moments μ_a and μ_b are taken to be real for convenience and the electric fields are given by:

$$\mathcal{E}_a = \frac{1}{2}E_a e^{-i\nu_a t} + c.c. \tag{B.3}$$

$$\mathcal{E}_b = \frac{1}{2}E_b e^{-i\nu_b t} + c.c. \tag{B.4}$$

We wish to derive equations of motion for the density matrix elements, where the density matrix is of the form:

$$\rho = \begin{pmatrix} \rho_{ee} & \rho_{ea} & \rho_{eb} \\ \rho_{ae} & \rho_{aa} & \rho_{ab} \\ \rho_{be} & \rho_{ba} & \rho_{bb} \end{pmatrix} \tag{B.5}$$

Using the basic relationship $\dot{\rho} = \frac{i}{\hbar}[\rho, \mathcal{H}]$, we may derive the equations of motion for the density matrix elements. In the following sections, we will perform this derivation for each of the three types of system considered.

OBE Derivation for Λ System

In this system, we are interested in the density matrix elements ρ_{ea}, ρ_{eb}, ρ_{ba}, ρ_{aa}, and ρ_{bb}. We make the following substitutions:

$$\rho_{ea} = \tilde{p}_a e^{-i\nu_a t} \tag{B.6}$$

$$\rho_{eb} = \tilde{p}_b e^{-i\nu_b t} \tag{B.7}$$

$$\rho_{ba} = \tilde{p}_r e^{i(\nu_b - \nu_a)t} \tag{B.8}$$

$$\rho_{aa} = n_a \tag{B.9}$$

$$\rho_{bb} = n_b \tag{B.10}$$

Using the Hamiltonian and the above substitutions for the density matrix elements we can derive the equations of motion. After making the rotating wave approximation (RWA) and introducing phenomenological decay terms, we obtain the following set of OBE:

$$\dot{\tilde{p}}_a = (i\delta_a - \gamma_a)\tilde{p}_a - \frac{i\Omega_a}{2}(1 - n_b - 2n_a) + \frac{i\Omega_b}{2}\tilde{p}_r \tag{B.11}$$

$$\dot{\tilde{p}}_b = (i\delta_b - \gamma_b)\tilde{p}_b - \frac{i\Omega_b}{2}(1 - n_a - 2n_b) + \frac{i\Omega_a}{2}\tilde{p}_r^* \tag{B.12}$$

$$\dot{\tilde{p}}_r = \left[i(\delta_a - \delta_b) - \gamma_r\right]\tilde{p}_r - \frac{i\Omega_a}{2}\tilde{p}_b^* + \frac{i\Omega_b}{2}\tilde{p}_a \tag{B.13}$$

$$\dot{n}_a = \Gamma_a(1 - n_a - n_b) + \frac{i}{2}(\Omega_a^*\tilde{p}_a - c.c.) \tag{B.14}$$

$$\dot{n}_b = \Gamma_b(1 - n_a - n_b) + \frac{i}{2}(\Omega_b^*\tilde{p}_b - c.c.) \tag{B.15}$$

where $\delta_a = \nu_a - \omega_a$, $\delta_b = \nu_b - \omega_b$, $\omega_a = \omega_{ee} - \omega_{aa}$, and $\omega_b = \omega_{ee} - \omega_{bb}$. The Rabi frequencies are defined by $\Omega_a = \frac{\mu_a E_a}{\hbar}$, and $\Omega_b = \frac{\mu_b E_b}{\hbar}$. We have also made the assumption that $n_a + n_b + n_e = 1$, in order to eliminate n_e from the equations.

EIT in Λ System

We consider the pump-probe scheme show in Fig. 88 with strong pump Ω_b and weak probe Ω_a. We also consider an arbitrary initial population in the state $|a\rangle$ denoted by $n_a^{(0)}$. Keeping only terms up to first order in Ω_a, the OBE reduce to:

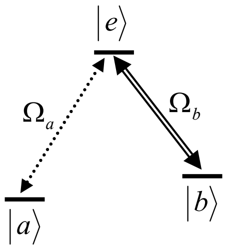

FIGURE 88. Pump and probe fields in Λ system

$$\dot{\tilde{p}}_b^{(0)} = (i\delta_b - \gamma_b)\,\tilde{p}_b^{(0)} - \frac{i\Omega_b}{2}\left(1 - n_a^{(0)} - 2n_b^{(0)}\right) \tag{B.16}$$

$$\dot{n}_b^{(0)} = \Gamma_b\left(1 - n_a^{(0)} - n_b^{(0)}\right) + \frac{i}{2}\left(\Omega_b^*\tilde{p}_b^{(0)} - c.c\right) \tag{B.17}$$

$$\dot{\tilde{p}}_a^{(1)} = (i\delta_a - \gamma_a)\,\tilde{p}_a^{(1)} - \frac{i\Omega_a}{2}\left(1 - n_b^{(0)} - 2n_a^{(0)}\right) + \frac{i\Omega_b}{2}\tilde{p}_r^{(1)} \tag{B.18}$$

$$\dot{\tilde{p}}_r^{(1)} = \left[i\left(\delta_a - \delta_b\right) - \gamma_r\right]\tilde{p}_r^{(1)} - \frac{i\Omega_a}{2}\tilde{p}_b^{(0)*} + \frac{i\Omega_b^*}{2}\tilde{p}_a^{(1)} \tag{B.19}$$

where the superscript refers to the power of Ω_a.

Next we consider the conventional EIT situation, in which $n_a^{(0)} = 1$, and therefore $n_b^{(0)} = \tilde{p}_b^{(0)} = 0$. In this case, solving the OBE under steady-state conditions gives the following result for $\tilde{p}_a^{(1)}$.

$$\tilde{p}_a^{(1)} = \frac{-\frac{i\Omega_a}{2}\left[i\left(\delta_a - \delta_b\right) - \gamma_r\right]}{\left(i\delta_a - \gamma_a\right)\left[i\left(\delta_a - \delta_b\right) - \gamma_r\right] + \frac{|\Omega_b|^2}{4}} \tag{B.20}$$

To find the linear absorption, $\alpha(\delta_a)$, we use the relation $\alpha \propto \mathrm{Im}\left[\frac{\tilde{p}_a^{(1)}}{\Omega_a}\right]$.

If $\delta_b = 0$, the reduction in absorption at the line center ($\delta_a = 0$) is given by the ratio

$$\frac{\alpha\left(0\right)}{\alpha_0} = \frac{1}{1 + \frac{|\Omega_b|^2}{4\gamma_a\gamma_r}} \tag{B.21}$$

where α_0 is the absorption at $\delta_a = 0$ for $\Omega_b = 0$. In order to achieve greater than 50 percent reduction in absorption, we require $|\Omega_b|^2 > 4\gamma_a\gamma_r$

A steady-state solution of the OBE for the case $n_a^{(0)} \neq 1$ is also possible, but is not given here. Note that in this case, the absorption by the $|a\rangle \leftrightarrow |e\rangle$ transition is affected by the saturation of the $|b\rangle \leftrightarrow |e\rangle$ transition.

OBE Derivation for *Cascade* System

In this system, we are interested in the density matrix elements ρ_{ea}, ρ_{be}, ρ_{ba}, ρ_{aa}, and ρ_{bb}. We make the following substitutions:

$$\rho_{ea} = \tilde{p}_a e^{-i\nu_a t} \tag{B.22}$$

$$\rho_{be} = \tilde{p}_b e^{-i\nu_b t} \tag{B.23}$$

$$\rho_{ba} = \tilde{p}_r e^{-i(\nu_b+\nu_a)t} \tag{B.24}$$

$$\rho_{aa} = n_a \tag{B.25}$$

$$\rho_{bb} = n_b \tag{B.26}$$

After making the RWA and introducing decay terms, we obtain the following set of OBE:

$$\dot{\tilde{p}}_a = (i\delta_a - \gamma_a)\tilde{p}_a - \frac{i\Omega_a}{2}(1 - n_b - 2n_a) + \frac{i\Omega_b^*}{2}\tilde{p}_r \tag{B.27}$$

$$\dot{\tilde{p}}_b = (i\delta_b - \gamma_b)\tilde{p}_b - \frac{i\Omega_b}{2}(2n_b + n_a - 1) - \frac{i\Omega_a^*}{2}\tilde{p}_r \tag{B.28}$$

$$\dot{\tilde{p}}_r = \left[i(\delta_a + \delta_b) - \gamma_r\right]\tilde{p}_r - \frac{i\Omega_a}{2}\tilde{p}_b + \frac{i\Omega_b}{2}\tilde{p}_a \tag{B.29}$$

$$\dot{n}_a = \Gamma_a(1 - n_a - n_b) + \frac{i}{2}(\Omega_a^*\tilde{p}_a - c.c.) \tag{B.30}$$

$$\dot{n}_b = -\Gamma_b n_b - \frac{i}{2}(\Omega_b^*\tilde{p}_b - c.c.) \tag{B.31}$$

where $\delta_a = \nu_a - \omega_a$, $\delta_b = \nu_b - \omega_b$, $\omega_a = \omega_{ee} - \omega_{aa}$, and $\omega_b = \omega_{bb} - \omega_{ee}$. The Rabi frequencies are defined by $\Omega_a = \frac{\mu_a E_a}{\hbar}$, and $\Omega_b = \frac{\mu_b E_b}{\hbar}$. We have also made the assumption that $n_a + n_b + n_e = 1$, in order to eliminate n_e from the equations.

EIT in *Cascade* System

Using the pump-probe scheme shown in Fig. 89, with strong pump Ω_b and weak probe Ω_a, we can simplify the OBE by keeping terms only up to first order in Ω_a. Assuming that $n_a^{(0)} = 1$ (all initial population in the ground state), the relevant equations are:

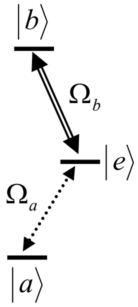

FIGURE 89. Pump and probe fields in *cascade* system

$$\dot{\tilde{p}}_a^{(1)} = (i\delta_a - \gamma_a)\,\tilde{p}_a^{(1)} + \frac{i\Omega_a}{2} + \frac{i\Omega_b^*}{2}\tilde{p}_r^{(1)} \tag{B.32}$$

$$\dot{\tilde{p}}_r^{(1)} = [i\,(\delta_a + \delta_b) - \gamma_a]\,\tilde{p}_r^{(1)} + \frac{i\Omega_b}{2}\tilde{p}_a^{(1)} \tag{B.33}$$

Solving the above equations under steady-state conditions, we obtain the following expression for $\tilde{p}_a^{(1)}$.

$$\tilde{p}_a^{(1)} = \frac{-\frac{i\Omega_a}{2}\left[i\left(\delta_a+\delta_b\right)-\gamma_r\right]}{\left(i\delta_a-\gamma_a\right)\left[i\left(\delta_a+\delta_b\right)-\gamma_r\right]+\frac{|\Omega_b|^2}{4}} \tag{B.34}$$

Note that the result is identical to that for the Λ system, if we account for how the detunings relate to the level structures. In both systems, the strongest reduction in absorption occurs if the net detuning of the two-photon transition $|a\rangle \leftrightarrow |b\rangle$ is zero. For the Λ system, this corresponds to $\delta_a - \delta_b = 0$, while for the *cascade* system, the condition is $\delta_a + \delta_b = 0$.

OBE Derivation for V System

In this system, we use state $|g\rangle$ instead of state $|e\rangle$, but otherwise the derivation proceeds as before. We are interested in the density matrix elements ρ_{ag}, ρ_{bg}, ρ_{ba}, ρ_{aa}, and ρ_{bb}. We make the following substitutions:

$$\rho_{ag} = \tilde{p}_a e^{-i\nu_a t} \tag{B.35}$$

$$\rho_{bg} = \tilde{p}_b e^{-i\nu_b t} \tag{B.36}$$

$$\rho_{ba} = \tilde{p}_r e^{-i(\nu_b-\nu_a)t} \tag{B.37}$$

$$\rho_{aa} = n_a \tag{B.38}$$

$$\rho_{bb} = n_b \tag{B.39}$$

After making the RWA and introducing phenomenological decay terms, we obtain the following set of OBE:

$$\dot{\tilde{p}}_a = (i\delta_a - \gamma_a)\tilde{p}_a - \frac{i\Omega_a}{2}(2n_a + n_b - 1) - \frac{i\Omega_b}{2}\tilde{p}_r^* \tag{B.40}$$

$$\dot{\tilde{p}}_b = (i\delta_b - \gamma_b)\tilde{p}_b - \frac{i\Omega_b}{2}(2n_b + n_a - 1) - \frac{i\Omega_a}{2}\tilde{p}_r \tag{B.41}$$

$$\dot{\tilde{p}}_r = \left[i(\delta_a - \delta_b) - \gamma_r\right]\tilde{p}_r - \frac{i\Omega_a^*}{2}\tilde{p}_b + \frac{i\Omega_b}{2}\tilde{p}_a^* \tag{B.42}$$

$$\dot{n}_a = -\Gamma_a n_a - \frac{i}{2}(\Omega_a^*\tilde{p}_a - c.c.) \tag{B.43}$$

$$\dot{n}_b = -\Gamma_b n_b - \frac{i}{2}(\Omega_b^*\tilde{p}_b - c.c.) \tag{B.44}$$

where $\delta_a = \nu_a - \omega_a$, $\delta_b = \nu_b - \omega_b$, $\omega_a = \omega_{aa} - \omega_{gg}$, and $\omega_b = \omega_{bb} - \omega_{gg}$. The Rabi frequencies are defined by $\Omega_a = \frac{\mu_a E_a}{\hbar}$, and $\Omega_b = \frac{\mu_b E_b}{\hbar}$. We have also made the assumption that $n_a + n_b + n_g = 1$, in order to eliminate n_g from the equations.

EIT in *V* System

We consider the pump-probe scheme show in Fig. 90 with strong pump Ω_b and weak probe Ω_a. We assume that all initial population is in state $|g\rangle$. Keeping only terms up to first order in Ω_a, the OBE reduce to:

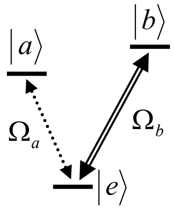

FIGURE 90. Pump and probe fields in V system

$$\dot{\tilde{p}}_b^{(0)} = (i\delta_b - \gamma_b)\,\tilde{p}_b^{(0)} - \frac{i\Omega_b}{2}\left(2n_b^{(0)} - 1\right) \tag{B.45}$$

$$\dot{n}_b^{(0)} = -\Gamma_b n_b^{(0)} - \frac{i}{2}\left(\Omega_b^* \tilde{p}_b^{(0)} - c.c\right) \tag{B.46}$$

$$\dot{\tilde{p}}_a^{(1)} = (i\delta_a - \gamma_a)\,\tilde{p}_a^{(1)} - \frac{i\Omega_a}{2}\left(n_b^{(0)} - 1\right) - \frac{i\Omega_b}{2}\tilde{p}_r^{(1)*} \tag{B.47}$$

$$\dot{\tilde{p}}_r^{(1)} = \left[i\left(\delta_b - \delta_a\right) - \gamma_r\right]\tilde{p}_r^{(1)} - \frac{i\Omega_a^*}{2}\tilde{p}_b^{(0)} + \frac{i\Omega_b}{2}\tilde{p}_a^{(1)*} \tag{B.48}$$

Solving the zeroth-order equations in steady-state gives the standard two-level results:

$$n_b^{(0)} = \frac{\frac{1}{2} I_b \mathcal{L}_b}{1 + I_b \mathcal{L}_b} \tag{B.49}$$

$$\tilde{p}_b^{(0)} = -\frac{i\Omega_b}{2} \cdot \frac{1}{(i\delta_b - \gamma_b)} \cdot \frac{1}{1 + I_b \mathcal{L}_b} \tag{B.50}$$

where $I_b = \frac{|\Omega_b|^2}{\gamma_b \Gamma_b}$ and $\mathcal{L}_b = \frac{\gamma_b^2}{\gamma_b^2 + \delta_b^2}$.

Although a general solution is possible, here we only consider the case $\delta_b = 0$. In this case, we obtain the following result for $\tilde{p}_a^{(1)}$

$$\tilde{p}_a^{(1)} = -\frac{\frac{i\Omega_a}{2}}{\left[\left(i\delta_a - \gamma_a\right)\left(i\delta_a - \gamma_r\right) + \frac{|\Omega_b|^2}{4} \right]} \cdot \frac{\left(i\delta_a - \gamma_r\right)\left(1 + \frac{1}{2} I_b\right) + \frac{|\Omega_b|^2}{4\gamma_b}}{1 + I_b} \tag{B.51}$$

Solving for the absorption at $\delta_a = 0$ gives:

$$\frac{\alpha\left(0\right)}{\alpha_0} = \frac{1}{1 + \frac{|\Omega_b|^2}{4\gamma_a\gamma_r}} \cdot \frac{1 + \frac{|\Omega_b|^2}{4\gamma_b\Gamma_b}\left(2 - \frac{\Gamma_b}{\gamma_r}\right)}{1 + \frac{|\Omega_b|^2}{\gamma_b\Gamma_b}} \tag{B.52}$$

The first term is the same as for the Λ and the *cascade* systems, and represents the reduction in absorption due to EIT interference effects. The second term represents the reduction in absorption due to saturation of the $|g\rangle \leftrightarrow |b\rangle$ transition. For example, if we let $\Gamma_b \to 0$, then

$$\frac{\alpha\left(0\right)}{\alpha_0} \to \frac{1}{1 + \frac{|\Omega_b|^2}{4\gamma_a\gamma_r}} \cdot \frac{1}{2} \tag{B.53}$$

indicating that half of the population has been pumped into state $|b\rangle$.

APPENDIX C

NUMERICAL SOLUTIONS OF OBE USING MATHEMATICA

Included on the following pages is a copy of a Mathematica notebook used to perform numerical solutions of the OBE described in the text of the dissertation. By changing the input parameters and the differential equations in the notebook, this basic script was adapted for all the numerical simulations presented in this dissertation.

EIT in a lambda system. Probe kept to first order only.

```
          (* sample properties *)
γa = 1;     γr = 1;

          (* probe parameters *)

t0 = 0;
τ = -2;
awidth = .05;
aamp = 1;
Ωa = aamp Exp[- ((t - t0 - τ) / awidth) ^2];

          (*  pump parameters *)

bwidth = 5;
bamp = 4;
 Ωb = bamp Exp[- ((t - t0) / bwidth) ^2];

          (* definitions *)
δa = 0;
δb = 0;


          (* differential equations *)
solution = NDSolve[{
    pa'[t] == (I δa - γa ) pa[t] + I / 2 Ωa  + I / 2 Ωb pr[t],
    pr'[t] == (I (δa - δb) - γr ) pr[t] + I / 2 Ωb pa[t],
    pa[t0 - 500] == 0, pr[t0 - 500] == 0},
   {pa, pr},
   {t, -500, 500},
   MaxSteps → Infinity, MaxStepSize → .01, Method → RungeKutta];


Plot[{Ωa / aamp, Ωb / bamp, 50 Im[Evaluate[pa[t] /. solution] / aamp]},
 {t, -500, 500}, PlotRange → {{-15, 15}, {-1, 1}},
 PlotStyle → {RGBColor[0, 0, 1], RGBColor[0, 0, 0], RGBColor[0, 1, 0]}, PlotPoints → 500]

Plot[{Ωa / aamp, Ωb / bamp, 50 Re[Evaluate[pr[t] /. solution] / aamp]},
 {t, -500, 500}, PlotRange → {{-15, 15}, {-1, 1}},
 PlotStyle → {RGBColor[0, 0, 1], RGBColor[0, 0, 0], RGBColor[0, 1, 0]}, PlotPoints → 500]
```

(∗ take fourier transform to get spectrum ∗)

```
starttime = -500; endtime = 500; samples = 16384 * 2;
(* make samples an even number, pref power of 2 *)
time = Table[starttime + i (endtime - starttime) / (samples - 1), {i, 0, samples - 1}];
patimeseries = First[Evaluate[pa[time] /. solution]];
probetimeseries = aamp Exp[- ((time - t0 - τ) / awidth) ^2];
pumptimeseries = bamp Exp[- ((time - t0) / bwidth) ^2];

freq = Flatten[{Table[N[2 Pi (j - 1) / (endtime - starttime)], {j, 1, samples / 2}],
    Table[N[-2 Pi (samples - j + 1) / (endtime - starttime)], {j, samples / 2 + 1, samples}]}];
specresponse = Fourier[patimeseries];
proberesponse = Fourier[probetimeseries];
pumpresponse = Fourier[pumptimeseries];
specseries = 2 γa Im[specresponse / proberesponse];
theorspecseries = 2 γa ^2 / (2 (freq^2 + γa ^2));

spectrum = Flatten[{Take[Transpose[{freq, specseries}], -samples / 2],
    Take[Transpose[{freq, specseries}], samples / 2]}, 1];
theorspectrum = Flatten[{Take[Transpose[{freq, theorspecseries}], -samples / 2],
    Take[Transpose[{freq, theorspecseries}], samples / 2]}, 1];
diffabs = Transpose[{Transpose[spectrum][[1]],
    Transpose[spectrum][[2]] - Transpose[theorspectrum][[2]]}];
probespectrum = Flatten[{Take[Transpose[{freq, Abs[proberesponse]}], -samples / 2],
    Take[Transpose[{freq, Abs[proberesponse]}], samples / 2]}, 1];
pumpspectrum = Flatten[{Take[Transpose[{freq, Abs[pumpresponse]}], -samples / 2],
    Take[Transpose[{freq, Abs[pumpresponse]}], samples / 2]}, 1];

Null
```

(∗ plot spectra ∗)

```
ListPlot[probespectrum, PlotJoined → True,
  PlotRange → {{-10, 10}, {-1, 1}}, PlotStyle → {RGBColor[0, 0, 1]}];
ListPlot[pumpspectrum, PlotJoined → True, PlotRange → {{-10, 10}, {-1, 1}},
  PlotStyle → {RGBColor[0, 0, 1]}];
ListPlot[spectrum, PlotJoined → True, PlotRange → {{-10, 10}, {-1, 1}}];
ListPlot[theorspectrum, PlotJoined → True, PlotRange → {{-10, 10}, {-1, 1}}];
ListPlot[diffabs, PlotJoined → True, PlotRange → {{-10, 10}, {-1, 1}}];

Null
```

```
filecounter = 1;
```

```
        (* Data Export *)
timedata =
  Table[{t, N[Ω_a] / aamp, N[Ω_b] / bamp, Flatten[Evaluate[20 Im[pa[t]] /. solution]][[1]],
    Flatten[Evaluate[Re[pr[t]] /. solution]][[1]]}, {t, -20, 20, .01}];

header = If[filecounter < 10, "/simulationdata/data093002/mp093002_0",
   "/simulationdata/data093002/mp093002_"];
dataparams = {{"gamma", γ_a}, {"gammaab", γ_r}, {"pumpdetuning", δ_b},
   {"pumplength", bwidth}, {"pumpamp", bamp}, {"delay", τ}};
Export[header <> ToString[filecounter] <> "_abs" <> ".dat",
 Take[spectrum, {3 samples / 8, 5 * samples / 8}]]
Export[header <> ToString[filecounter] <> "_pump" <> ".dat",
 Take[pumpspectrum, {3 samples / 8, 5 * samples / 8}]]
Export[header <> ToString[filecounter] <> "_timedata" <> ".dat", timedata]
Export[header <> ToString[filecounter] <> "_params" <> ".dat", dataparams]
filecounter++;
Null

Export[header <> ToString[filecounter] <> "_nopumpabs" <> ".dat",
 Take[theorspectrum, {3 samples / 8, 5 * samples / 8}]]
```

BIBLIOGRAPHY

[1] J. E. Field, K. H. Hahn, and S. E. Harris, “Observation of Electromagnetically Induced Transparency in Collisionally Broadened Lead Vapor,” Phys. Rev. Lett. **67,** 3062–3065 (1991).

[2] K. J. Boller, A. Imamoǧlu, and S. E. Harris, “Observation of Electromagnetically Induced Transparency,” Phys. Rev. Lett. **66,** 2593–2596 (1991).

[3] S. E. Harris, “Electromagnetically induced transparency,” Physics Today **50(7),** 36–42 (1997).

[4] M. O. Scully and M. S. Zubairy, *Quantum Optics* (Cambridge University Press, 1997).

[5] L. V. Hau, S. E. Harris, Z. Dutton, and C. H. Behroozi, “Light speed reduction to 17 metres per second in an ultracold atomic gas,” Nature **397,** 594–598 (1999).

[6] S. E. Harris, J. E. Field, and A. Kasapi, “Dispersive properties of electromagnetically induced transparency,” Phys. Rev. A **46,** R29–R32 (1992).

[7] M. K. Kash, V. A. Sautenkov, A. S. Zibrov, L. Hollberg, G. R. Welch, M. D. Lukin, Y. Rostovtsev, E. S. Fry, and M. O. Scully, “Ultraslow group velocity and enhanced nonlinear optical effects in a coherently driven hot atomic gas,” Phys. Rev. Lett. **82,** 5229–5232 (1999).

[8] J. Oreg, F. T. Hioe, and J. H. Eberly, “Adiabatic following in multilevel systems,” Phys. Rev. A **29,** 690–697 (1984).

[9] B. W. Shore, K. Bergmann, J. Oreg, and S. Rosenwaks, “Multilevel adiabatic population transfer,” Phys. Rev. A **44,** 7442–7447 (1991).

[10] C. Liu, Z. Dutton, C. H. Behroozi, and L. V. Hau, “Observation of coherent optical information storage in an atomic medium using halted light pulses,” Nature **409,** 490–493 (2001).

[11] D. F. Phillips, A. Fleischhauer, A. Mair, R. L. Walsworth, and M. D. Lukin, “Storage of Light in Atomic Vapor,” Phys. Rev. Lett. **86,** 783–786 (2001).

[12] S. E. Harris, “Lasers without inversion: Interference of lifetime-broadened resonances,” Phys. Rev. Lett. **62,** 1033–1036 (1989).

[13] M. O. Scully, S. Y. Zhu, and A. Gavrielides, “Degenerate quantum-beat laser: Lasing without inversion and inversion without lasing,” Phys. Rev. Lett. **62,** 2813-2816 (1989).

[14] A. Imamolu, J. E. Field, and S. E. Harris, “Lasers without inversion: A closed lifetime broadened system,” Phys. Rev. Lett. **66,** 1154-1156 (1991).

[15] A. Schülzgen, R. Binder, M. E. Donovan, M. Lindberg, K. Wundke, H. M. Gibbs, G. Khitrova, and N. Peyghambarian, “Direct observation of excitonic rabi oscillations in semiconductors,” Phys. Rev. Lett. **82,** 2346–2349 (1999).

[16] K. B. Ferrio and D. G. Steel, “Raman quantum beats of interacting excitons,” Phys. Rev. Lett. **80,** 786–789 (1998).

[17] B. F. Feuerbacher, J. Kuhl, and K. Ploog, “Biexcitonic contribution to the degenerate-four-wave-mixing signal from a GaAs/AlxGa1-xAs quantum well,” Phys. Rev. B **43,** 2439-2441 (1991).

[18] H. Wang, J. Shah, T. C. Damen, and L. N. Pfeiffer, “Polarization-dependent coherent nonlinear optical response in GaAs quantum wells: dominant effects of two-photon coherence between ground and biexciton states,” Solid State Comm. **91,** 869–874 (1994).

[19] M. E. Donovan *et al.*, “Evidence for Intervalence Band Coherences in Semiconductor Quantum Wells via Coherently Coupled Optical Stark Shifts,” Phys. Rev. Lett. **87,** 237402 (2001).

[20] M. Lindberg and R. Binder, “Dark States in Coherent Semiconductor Spectroscopy,” Phys. Rev. Lett. **75,** 1403–1406 (1995).

[21] G. S. Agarwal, “Electromagnetic-field-induced transparency in high-density exciton systems,” Phys. Rev. A **51,** R2711–R2714 (1995).

[22] G. B. Serapiglia, E. Paspalakis, C. Sirtori, K. L. Vodopyanov, , and C. C. Phillips, “Laser-Induced Quantum Coherence in a Semiconductor Quantum Well,” Phys. Rev. Lett. **84,** 1019–1022 (2000).

[23] A. Liu and C. Z. Ning, “Exciton absorption in semiconductor quantum wells driven by a strong intersubband pump field,” J. Opt. Soc. Am. B **17,** 433–439 (2000).

[24] A. Imamoglu and R. J. Ram, “Semiconductor lasers without population inversion,” Opt. Lett. **19,** 1744–1746 (1994).

[25] J. Shah, *Ultrafast Spectroscopy of Semiconductors and Semiconductor Nanostructures*, 2nd ed. (Springer, 1999).

[26] H. Wang, K. Ferrio, D. G. Steel, Y. Z. Hu, R. Binder, and S. W. Koch, “Transient nonlinear optical response from excitation induced dephasing in GaAs,” Phys. Rev. Lett. **71,** 1261–1264 (1993).

[27] H. Haug and S. W. Koch, *Quantum theory of the optical and electronic properties of semiconductors*, 3rd ed. (World Scientific, 1990).

[28] V. M. Axt and A. Stahl, “A dynamics-controlled truncation scheme for the hierarchy of density matrices in semiconductor optics,” Z. Phys. B, Condens. Matter **93,** 195–204 (1994).

[29] P. Meystre and I. M. Sargent, *Elements of Quantum Optics*, 3rd ed. (Springer, 1999).

[30] M. Saba, F. Quochi, C. Ciuti, D. Martin, J. L. Staehli, and B. Deveaud, “Direct observation of the excitonic ac Stark splitting in a quantum well,” Phys. Rev. B **62,** R16322–R16325 (2000).

[31] M. Phillips, H. Wang, I. Rumyantsev, N. H. Kwong, R. Takayama, and R. Binder, “Electromagnetically induced transparency in semiconductors,” submitted to Science (2002).

[32] S. Schmitt-Rink, D. S. Chemla, and D. A. B. Miller, “Linear and Nonlinear optical properties of semiconductor quantum wells,” Adv. Physics **38,** 89–188 (1989).

[33] D. S. Chemla and D. A. B. Miller, “Room-temperature excitonic nonlinear-optical effects in semiconductor quantum wells,” J. Opt. Soc. Am. B **2,** 1155–1173 (1985).

[34] P. K. Basu, *Theory of optical processes in semiconductors: bulk and microstructures* (Oxford, 1997).

[35] N. Peyghambarian, H. M. Gibbs, J. L. Jewell, A. Antonetti, A. Migus, D. Hulin, and A. Mysyrowicz, “Blue shift of the exciton resonance due to exciton-exciton interactions in a multiple-quantum-well structure,” Phys. Rev. Lett. **53,** 2433–2436 (1984).

[36] M. Wegener, D. S. Chemla, S. Schmitt-Rink, and W. Schäfer, “Line shape of time-resolved four-wave mixing,” Phys. Rev. A **42,** 5675–5683 (1990).

[37] H. P. Wagner, W. Langbein, and J. M. Hvam, “Mixed biexcitons in single quantum wells,” Phys. Rev. B **59,** 4584–4587 (1999).

[38] T. Meier, S. W. Koch, M. Phillips, and H. Wang, “Strong coupling of heavy- and light-hole excitons induced by many-body correlations,” Phys. Rev. B **62,** 12605–12608 (2000).

[39] D. S. Alavi, P. C. Sercel, and M. G. Raymer, http://materialscience. uoregon. edu/sercel/pslas.htm, (unpublished).

[40] I. I. Rabi, “Space Quantization in a Gyrating Magnetic Field,” Phys. Rev. **51,** 652-654 (1937).

[41] B. R. Mollow, “Power Spectrum of Light Scattered by Two-Level Systems,” Phys. Rev. **188,** 1969-1975 (1969).

[42] B. R. Mollow, “Stimulated Emission and Absorption near Resonance for Driven Systems,” Phys. Rev. A **5,** 2217-2222 (1972).

[43] F. Y. Wu, S. Ezekiel, M. Ducloy, and B. R. Mollow, “Observation of Amplification in a Strongly Driven Two-Level Atomic System at Optical Frequencies,” Phys. Rev. Lett. **38,** 1077-1080 (1977).

[44] F. Y. Wu, R. E. Grove, and S. Ezekiel, “Investigation of the Spectrum of Resonance Fluorescence Induced by a Monochromatic Field,” Phys. Rev. Lett. **35,** 1426-1429 (1975).

[45] C. Cohen-Tonnoudji, J. Dupont-Roc, and G. Grynberg, *Photons and Atoms, Introduction to Quantum Electrodynamics* (Wiley, 1989).

[46] R. Binder, S. W. Koch, M. Lindberg, N. Peyghambarian, and W. Schäfer, “Ultrafast adiabatic following in semiconductors,” Phys. Rev. Lett. **65,** 899–902 (1990).

[47] S. T. Cundiff, A. Knorr, J. Feldmann, S. W. Koch, E. O. Göbel, and H. Nickel, “Rabi flopping in semiconductors,” Phys. Rev. Lett. **73,** 1178–1181 (1994).

[48] H. Giessen, A. Knorr, S. Haas, S. W. Koch, S. Linden, J. Kuhl, M. Hetterich, M. Grn, and C. Klingshirn, “Self-Induced Transmission on a Free Exciton Resonance in a Semiconductor,” Phys. Rev. Lett. **81,** 4260-4263 (1998).

[49] T. H. Stievater, X. Li, D. G. Steel, D. Gammon, D. S. Katzer, D. Park, C. Piermarocchi, and L. J. Sham, “Rabi Oscillations of Excitons in Single Quantum Dots,” Phys. Rev. Lett. **87,** 133603 (2001).

[50] S. W. Koch, N. Peyghambarian, and M. Lindberg, "Transient and steady-state optical non-linearities in semiconductors," J. Phys. C **21,** 5229–5249 (1988).

[51] C. Sieh *et al.*, "Coulomb Memory Signatures in the Excitonic Optical Stark Effect," Phys. Rev. Lett. **82,** 3112–3115 (1999).

[52] P. Brick, C. Ell, S. Chatterjee, G. Khitrova, H. M. Gibbs, T. Meier, C. Sieh, and S. W. Koch, "Influence of light holes on the heavy-hole excitonic optical Stark effect," Phys. Rev. B **64,** 075323 (2001).

[53] T. C. Damen, L. Vina, J. E. Cunningham, J. Shah, and L. J. Sham, "Subpicosecond spin relaxation dynamics of excitons and free carriers in GaAs quantum wells," Phys. Rev. Lett. **67,** 3432–3435 (1991).

[54] D. J. Lovering, R. T. Phillips, G. J. Denton, and G. W. Smith, "Resonant generation of biexcitons in a GaAs quantum well," Phys. Rev. Lett. **68,** 1880-1883 (1992).

[55] E. Mayer *et al.*, "Evidence of biexcitonic contributions to four-wave mixing in GaAs quantum wells," Phys. Rev. B **50,** 14730–14733 (1994).

[56] G. Chen, T. H. Stievater, E. T. Batteh, X. Li, D. G. Steel, D. Gammon, D. S. Katzer, D. Park, and L. J. Sham, "Biexciton Quantum Coherence in a Single Quantum Dot," Phys. Rev. Lett. **88,** 117901 (2002).